2016

Terahertz Plasmonic Lasers with Distributed-Feedback

Chongzhao Wu
Lehigh University

Terahertz Plasmonic Lasers with Distributed-Feedback

by

Chongzhao Wu

A Dissertation
Presented to the Graduate Committee
of Lehigh University
in Candidacy for the Degree of
Doctor of Philosophy
in
Electrical Engineering

Lehigh University
September, 2016

Approved and recommended for acceptance as a dissertation in partial fulfillment of the requirements for the degree of Doctor of Philosophy.

Date

Dr. Sushil Kumar, Dissertation Director

Accepted Date

Committee Members

Dr. Sushil Kumar (Committee Chair)

Dr. Jonathan Wierer

Dr. Chao Zhou

Dr. Jean Toulouse

Acknowledgments

Over the period of my doctoral studies, I became deeply appreciative of the research area of terahertz photonics in which I was supervised and advised by Prof. Sushil Kumar. I consider myself very fortunate to have had Prof. Kumar as my advisor along my research journey as a PH.D. student. He is an outstanding scientist and extraordinary advisor. I learned numerous things from him directly. Some of the initial things that he taught me include hands-on training in the cleanroom for each step of the complex fabrication procedure of the semiconductor quantum cascade lasers (QCLs). I also recall countless hours that he spent with me in discussing simulations, experiments, and general research progress. His advice and encouragement about making impactful research presentations were always helpful, and were among my most unforgettable moments at Lehigh. His scientific vision and high academic standards kept me focused in pursuit of my research goals. With his guidance, I felt passionate and enthusiastic about my research projects. He has always been patient and accessible whenever I had needed to discuss with him. I have no hesitation in saying that he will be among my role-models as I move forward in my career. For all his support, I would like to express my sincere gratitude to Prof. Kumar.

I would also like to thank Prof. Jean Toulouse for his teaching, academic advising, and numerous helpful comments on my thesis. I appreciated his wonderful and detailed remarks written point-by-point on the evaluation draft of this thesis. I also thank Prof. Jonathan Wierer and Prof. Chao Zhou for serving on my thesis committee, for meeting with me, and for providing constructive criticisms and helpful suggestions.

I am grateful for all my labmates, Sudeep Khanal, Le Zhao, Yuan Jin, Liang Gao and Ji Chen for their help and for creating a positive atmosphere in the laboratory. Sudeep and I shared the most amount of overlapped time in the laboratory. He was kind to provide me generous help and guidance on aspects related to fabrication and measurement. I vividly remember our joint excitement when we noticed lasing in our laboratory for the first time. This thesis would not have been possible without

Sudeep's help. I also appreciate Yuan's efforts and contributions in fabrication and measurement of the tunable and high-power laser projects in the latter periods of my doctoral work.

Dr. John L. Reno from Sandia National Laboratories did MBE growth for the high quality QCLs wafers used in this doctoral work. Immense credit goes to his willingness to collaborate with us on this project, and which forms a fundamental backbone for all the experimental work that was performed as part of this thesis.

I would like to thank Prof. Bartoli, Prof. Ding, Prof. Tansu, and seniors Dr. Qiaoqiang Gan and Dr. Guan Sun for their help. I would also like to thank Chee-Keong Tan, Peifen Zhu, and Yongyang Huang who have been great friends at Lehigh.

I would like to thank my best friend, Dr. Guoqiang Xu from MIT. Our great friendship started ten yeas ago when we were undergraduate students.

The times spent at the Zoellner arts center and the Goodman campus sports facilities will forever remain parts of my Lehigh memory. I am thankful for Chartree as my table tennis partner and Phil as my tennis partner. Running across green fields and natural beauty at dusk or under starry skies at the Lehigh outdoor tracks and field helped me relieve academic pressures and provided me energy and motivation to overcome the challenges that I faced.

I thank Annie Yan Xie, for her love and support.

Care, love, and support from my parents Yuxiang Wu and Hongxia Wang remain my strongest driving force in moving forward in life. Phone calls with them always make me feel warm and relaxed. They are always there, waiting and expecting me to be home, as life continues to paint the color of snow on their hair.

Although a lot of challenges, difficulties, and failures are always associated with any research, there are always instances of euphoria when things work the way they were intended to. Similar instances happened during my Ph.D. research as well. On particular incident at 8 pm on January 9, 2014, will remain etched forever in my mind. I measured the narrow beam-pattern from our terahertz lasers for the first time on that day. I still remember how delighted I was to email my advisor immediately about the very important result, which was a culmination of novel

concepts, lot of simulations, and challenging fabrication and experimental work in prior years. Staring at the laser under the microscope after a long but satisfying fabrication period, or at the clear and large tuning spectra of single-mode lasers, there are many more such cherished but limited precious moments that make all the hard work in the six-years appear worthwhile. My motto remains: "Rainbow will appear after storm. Never lose hope!"

I dedicate this thesis to my grandparents, and to my six years of energetic youth at Lehigh University!

Contents

List of Figures **x**

Abstract **1**

1 Introduction **4**

1.1 Terahertz (THz) and its applications 4

1.2 Quantum cascade lasers (QCLs) 6

1.3 Terahertz semiconductor quantum cascade lasers 8

1.4 Terahertz quantum cascade lasers with metal-metal waveguides . . . 9

1.4.1 Strong terahertz mode-confinement in metal-metal microcavities 9

1.4.2 Poor emission characteristics of terahertz QCLs with metal-metal microcavities 10

1.5 Distributed-feedback (DFB) 11

1.6 Terahertz QCLs with traditional distributed-feedback 12

1.7 Overview 13

2 Terahertz plasmonic lasers radiating in an ultra-narrow beam **16**

2.1 Introduction 16

2.2 New antenna-feedback scheme for plasmonic lasers 18

2.3 Simulation results 22

2.4 Fabrication of antenna-feedback for THz QCLs 24

2.5 Experimental demonstration of antenna-feedback for THz QCLs 29

2.6 Experimental characteristics of third-order DFB QCL and a Fabry-Pérot-cavity QCL . . . 34
2.7 Summary . . . 37

3 Analysis and design of terahertz quantum cascade lasers with new antenna-feedback scheme 39
3.1 Analysis of antenna-feedback scheme . . . 40
3.2 Photonic engineering of antenna-feedback scheme . . . 55

4 Large tuning of narrow-beam terahertz plasmonic lasers operating above liquid-nitrogen temperature 60
4.1 Introduction and various tuning methods for THz QCLs . . . 60
4.2 Description of the tuning technique . . . 63
4.3 Results . . . 66
4.4 Discussion . . . 74

5 High power surface-emitting THz QCLs with single-lobed beam 76
5.1 A new grating design for surface-emitting terahertz QCLs . . . 77
5.2 Beam pattern from 3D simulations . . . 78
5.3 Experimental results . . . 80
5.3.1 Conventional second-order DFB with 100 μm width . . . 80
5.3.2 Second-order DFB with new photonic cavity with 70 μm width 81
5.3.3 Second-order DFB with new photonic cavity with 200 μm width 84

6 Conclusions and future outlook 86
6.1 Conclusions . . . 86
6.2 Future outlook . . . 89

A Appendix 92
A.1 Fabrication Recipes . . . 92
A.2 Finite Element Simulations . . . 101

A.2.1 2D simulations 101
A.2.2 3D simulations 103
A.3 Mechanical Drawings 105
A.3.1 Copper mounts used for edge-emitting and surface-emitting QCLs 105
A.3.2 Copper mount for edge-emitting QCLs, to mount very close to dewar's window 106

Bibliography **108**

Vita **116**

List of Figures

1.1 The terahertz frequency range in the eletromagnetic spectrum. . . . 4
1.2 Interband versus intersubband optical transitions in two-dimensional quantum wells. . . . 6
1.3 Left: Schematic of a metal-metal parallel plate ridge cavity, which confines the terahertz optical mode with very low losses at long wavelengths. Right: Measured far-field beam pattern of such a terahertz QCL [1]. Optical emission is highly divergent with distorted ring-like wavefronts. . . . 10
1.4 Schematic of a distributed Bragg grating implemented in a semiconductor gain medium to improve spectral and modal characteristics of laser cavities. . . . 12
1.5 Simulation results for second-order DFB. From left to right: the eigenmode spectrum of conventional second-order DFB, in-plane electric field and dominant electric field of the lowest loss mode. . . . 13

2.1 **The antenna-feedback concept for plasmonic lasers.** (a) The general principle of conventional distributed-feedback (DFB) that could be implemented in a spaser by introducing periodicity in its metallic cladding. A parallel-plate metallic cavity is illustrated; however, the principle is equally applicable to spaser cavities with a single metal-cladding. (b) If the periodicity in (a) is implemented by making holes or slits in the metal-cladding, the guided SPP wave diffracts out through the apertures and generates single-sided SPP waves on the cladding in the surrounding medium. The figure shows phase-mismatch between successive apertures for SPP waves on either side of the cladding. Coherent single-sided SPP waves in the surrounding medium cannot therefore be sustained owing to destructive interference with the guided SPP wave inside the cavity, as illustrated in (c). (d) Principle of an antenna-feedback grating. If the periodicity in the metal film allows the guided SPP mode to diffract outside the cavity, a grating period could be chosen that leads to the first-order Bragg diffraction in the opposite direction, but in the surrounding medium rather than inside the active medium itself. Similarly, the single-sided SPP mode in the surrounding medium undergoes first-order Bragg diffraction to couple with the guided SPP wave in the opposite direction inside the cavity. (e) The grating in (d) leads to a fixed phase-condition at each aperture between counter propagating SPP waves on the either side of metal-cladding. First, this leads to significant build up of amplitude in the single-sided SPP wave in the surrounding medium, as illustrated in (f). Second, emission from each aperture adds constructively to couple to far-field radiation in the end-fire (z) direction. As argued in the text, both of these aspects lead to narrow far-field emission profile in the $x - y$ plane. 19

2.2 **Comparison between conventional DFB (third-order DFB as an example) and antenna-feedback schemes for terahertz QCL cavities.** The figure shows SPP eigenmode spectrum and electric-field for the eigenmode with lowest loss calculated by finite-element simulations of parallel-plate metallic cavities as in Fig. 2.1, with GaAs as dielectric ($n_{\mathrm{a}} = 3.6$) and air as surrounding medium ($n_{\mathrm{s}} = 1$). Simulations are done in 2-D (i. e. cavities of infinite-width) for 10 μm thick and 1.4 mm long cavities, and metal and active-layers are considered lossless. A periodic grating with apertures of (somewhat arbitrary) width 0.2Λ in the top-metal cladding are implemented for DFB. Λ is chosen to excite the lowest-loss DFB mode at similar frequencies close to $\sim$ 3 THz. The eigenmode spectrum shows frequencies and loss for the resonant-cavity modes, which reflects combination of radiation loss and the loss at longitudinal absorbing regions. Radiation loss occurs through diffraction from apertures, and the amplitude of in-plane electric-field E_z is indicative of the outcoupling efficiency. The major fraction of EM energy for the resonant modes exists in TM polarized (E_y) electric-field. A photonic bandgap in the eigenmode spectrum is indicative of DFB effect due to the grating. The antenna-DFB grating excites a strong single-sided SPP standing-wave on top of the metallic grating (in air) as also illustrated in Fig. 2.1(f). Also, the radiative loss for the third-order DFB grating is smaller since the lowest-loss eigenmode has zeros of E_z under the apertures, which leads to smaller net outcoupling of radiation. The loss is $\sim$ 6.7 cm^{-1} and $\sim$ 10.6 cm^{-1} for the lowest loss resonant cavity mode of third-order DFB and antenna-feedback scheme, respectively. 21

2.3 Schematic of fabrication steps for THz QCLs with distributed-feedback (part1). 26

2.4 Schematic of fabrication steps for THz QCLs with distributed-feedback (part2). 27

2.5 Picture of laser chip on a Cu mount. 28
2.6 Experimental setup for measurements of THz QCLs. 30
2.7 **Lasing characteristics of terahertz QCLs with antenna-feedback.** (a) The schematic on left shows the QCL's metallic-cavity with antenna-feedback grating implemented in top metal cladding. The active-medium is 10 μm thick and based on a 3 THz GaAs/$Al_{0.10}Ga_{0.90}As$ QCL design. A scanning-electron microscope image of the fabricated QCLs is shown on the right. (b) Experimental light-current-voltage characteristics of a representative QCL with antenna-feedback of dimensions 1.4 mm $\times$ 100 μm at different heat-sink temperatures. The QCL is biased with low duty-cycle current pulses of 200 ns duration and 100 kHz repetition rate. Inset shows lasing spectra for different bias where the spectral linewidth is limited by instrument's resolution. The emitted optical power is measured without any cone collecting optic inside the cryostat. (c) Measured spectra for four different antenna-feedback QCLs with varying grating periods Λ, but similar overall cavity dimensions. The QCLs are biased at a current-density $\sim$ 440 A/cm^2 at 78 K. 31
2.8 Experimental setup for beam measurement. 32
2.9 **Far-field radiation-patterns of terahertz QCLs with antenna-feedback.** (a) Schematic showing orientation of QCLs and definition of angles. The QCLs were operated at 78 K in pulsed mode and biased at $\sim$ 440 A/cm^2 while lasing in single-mode. The plots are for QCLs with $\sim$ 1.4 mm long cavities and (b) 70 μm width and Λ = 21 μm grating emitting at $\sim$ 3.1 THz, (c) 100 μm width and Λ = 21 μm grating emitting at $\sim$ 3.1 THz, and (d) 100 μm width and Λ = 24 μm grating emitting at $\sim$ 2.9 THz respectively. 33

2.10 **Lasing characteristics of a terahertz QCL with third-order DFB without phase matching.** Light-current characteristics of a terahertz QCL with third-order DFB in pulsed operation. The QCL is fabricated on the same chip, and the cavity dimensions are similar to the QCLs with antenna-feedback. The inset shows the measured far-field radiation-pattern with the same angular definitions as in Fig. 2.9(a). The QCL emitted predominantly in single-mode at $\lambda = 103.0$ μm ($\nu = 2.91$ THz) with grating period 44 μm 35

2.11 **Lasing characteristics of a terahertz QCL with Fabry-Pérot cavity.** Light-current characteristics of a QCL with Fabry-Pérot cavity at different heat-sink temperatures in pulsed operation. Output power was collected with a Winston cone placed close to laser facet due to the highly divergent beam pattern of Fabry-Pérot type THz QCLs. The inset shows lasing spectra at different bias at ~ 78 K. . . 36

3.1 Energy-density profiles along the length of the metallic cavities (in z direction) for the band-edge DFB modes for (a) third-order DFB cavity, and (b) cavity with antenna-feedback respectively. 40

3.2 **Role of longitudinal absorbing boundaries in resonant-cavities with antenna-feedback.** (a) Eigenmode spectrum of QCL metallic cavity with antenna-feedback gratings in the top metallic layer, but without longitudinal absorbing boundaries at the two ends of the cavity. The dimensions of the cavity are otherwise similar to that for the result in Fig. 2.2(b). (b) Energy density profile along the length of the ~ 1.4 mm long cavity and dominant electric field E_y of a Fabry-Pérot cavity type mode that exists sufficiently away from the photonic bandgap. (c) Energy density profile and electric-field profile along the length of the cavity for the "desired" antenna-feedback mode that exists at the edge of the photonic bandgap. The z direction is along the length of laser ridge, as marked in Fig. 3.1. 41

3.3 **Electric-field profile of the SPP mode in surrounding medium of the plasmonic laser's cavity with antenna-feedback gratings from 3D simulation.** A parallel-plate metal cavity with GaAs medium of 100 μm width, 10 μm thickness, and 1.4 mm length is simulated. The frequency of the band-edge resonant-cavity mode is $\sim$ 3.15 THz, which is the desired "antenna-feedback" mode. Inset: Mode shape along lateral x dimension of cavity at a distance of 10 μm above the top metal cladding; the FWHM of the lateral electric-field profile is $\sim$ 130 μm. 43

3.4 **Comparison of electric-field squared modulus $|E|^2$ profile in conventional DFB (third-order DFB as an example) and antenna-feedback scheme.** (a) $|E|^2$ profile for third-order DFB cavity plotted along perpendicular y direction (cavity's height direction). (b) $|E|^2$ profile for antenna-feedback scheme with an expanded view close to top metal cladding. 44

3.5 **Geometry of full-wave 3D simulation** The modeled geometry for full-wave 3D simulation with the FEM solver [2]. Parallel-plate metallic terahertz QCL cavities of 1.4 mm length, 10 μm thickness, varying widths, and a grating period of $\Lambda = 21.7$ μm were implemented, which excite antenna-feedback resonant-cavity modes at $\nu \sim 3.1$ THz. . . . 45

3.6 **Full-wave 3D simulation to compute far-field radiation pattern of QCL cavities with antenna-feedback.** (a) Simulated far-field radiation pattern of the cavity with 100 μm width. The FWHM is $\sim 7^\circ \times 7^\circ$. (b) Far-field radiation pattern of the cavity with 70 μm width. The FWHM is $\sim 6^\circ \times 5^\circ$. 46

3.7 Measured beam pattern of antenna-feedback with 70 μm with Stirling cyrocooler at 50 K 47

3.8 **Beam pattern multiplication of a phased-array antenna model.** (a) Schematic of one-dimensional linear phased-array antenna model and a single radiative element. (b) Calculated array factor and simulated far field beam pattern from an array element. (c) Multiplication of array factor and element factor results in the far field beam pattern of phased-array antenna. 49
3.9 **Antenna-feedback scheme with $\sim$ 10 μm long longitudinal absorbing boundaries.** (a) Eigenmode spectrum for total length of cavity $\sim$ 1.4 mm. (b) Dominant TM polarized (E_y) electric-field along the whole length of cavity. (c) Zoomed in dominant E_y electric-field around the longitudinal center of cavity. (d) Zoomed in dominant E_z electric-field around the longitudinal center of cavity. 51
3.10 Antenna-feedback cavity for THz QCLs with duty cycle of 75% . . . 52
3.11 Antenna-feedback cavity for THz QCLs with total length $\sim$ 2 mm . . 53
3.12 **Electric-field distribution for third-order DFB with effective mode index $\sim$ 3.0 from 2D simulations.** (a) Dominant TM polarized (E_y) field, (b) In-plane (E_z) field around the longitudinal center of cavity. 53
3.13 **Electric-field distribution for third-order DFB with effective mode index $\sim$ 3.0 from 3D simulations.** (a) Dominant TM polarized (E_y) field from bottom view, (b) Dominant (E_y) field and in-plane (E_z) field around the longitudinal center of cavity from side view. 54
3.14 **Computed far-field radiation pattern of THz QCLs with third-order DFB cavity.** (a) Effective mode index $\sim$ 3.6 . (b) Effective mode index $\sim$ 3.0 55

3.15 **Structure 0 (one aperture for each grating period) for antenna-feedback $\sim$ 2 THz (schematic shown in Fig. 2.1(d))**. (a) Eigenmode spectrum for cavity of total length $\sim$ 1.4 mm. (b) Zoomed in dominant TM polarized (E_y) electric-field around the center of cavity for first-order DFB type mode with lower loss at lower frequency. (d) Zoomed in dominant TM polarized (E_y) electric-field around the center of cavity for antenna-feedback mode. 56

3.16 **Structure 1 (an extra aperture is implemented for one grating period of each two grating periods) to implement antenna-feedback scheme at $\sim$ 2 THz** . (a) Eigenmode spectrum for total length of cavity $\sim$ 1.4 mm. (b) Schematic of new structure 1 to implement antenna feedback at lower frequency $\sim$ 2 THz. (c) Dominant TM polarized (E_y) electric-field along the whole length of cavity for antenna-feedback mode as the lowest loss mode. (d) Dominant TM polarized (E_y) electric-field along the whole length of cavity for first-order DFB type mode with higher overall loss. 57

3.17 **Structure 2 (one extra aperture is implemented for each of grating period) for antenna-feedback at $\sim$ 3 THz** . (a) Eigenmode spectrum for total length of cavity $\sim$ 1.4 mm. (b) Schematic of new structure 2 to implement antenna feedback at $\sim$ 3 THz. (c) Dominant TM polarized (E_y) electric-field along the whole length of cavity for antenna-feedback mode as the lowest loss mode. Right: zoomed in (E_y) electric-field around the center of the cavity. (d) In-plane (E_z) electric-field along the whole length of cavity for antenna-feedback mode. Right: zoomed in (E_x) electric-field around the center of the cavity. 59

4.1 (a) Illustration of the antenna-feedback scheme for plasmonic lasers, which leads to generation of a hybrid surface-plasmon-polariton (SPP) mode in the surrounding medium of the laser's cavity. Here, a parallel-plate metallic cavity of a plasmonic laser is shown with slit-like apertures in its top metal cladding with a specific periodicity Λ as determined from equation (4.1), which lead to coupling of a guided SPP wave inside the cavity (interacting with the gain medium) with a single-sided SPP wave with a large spatial extent in the surrounding medium and propagating on the opposite side of the metal-cladding. (b) Schematic of terahertz plasmonic QCL with antenna-feedback grating implemented in the top-metal cladding with a periodicity Λ. The lateral and longitudinal absorbing boundaries are implemented to selectively excite the desired fundamental mode. A scanning electron microscope image of the fabricated QCLs is also shown. (c) The dominant electric-field component (E_y) of the lowest-loss resonant-cavity DFB mode is plotted along z axis, computed with finite-element (FEM) simulations using a commercial software package (Comsol 4.3). The height of the cavity is 10 μm. A hybrid SPP mode is excited in the surrounding medium along with the cavity SPP mode as illustrated in (a). 63

4.2 Optical image of a mounted QCL semiconductor chip out of which one of the QCLs with the antenna-feedback scheme is wire-bonded for electrical characterization. The QCL chip is soldered on a small copper chip that itself is screwed onto a bigger copper heat-sink to be mounted on the cold-plate of a cryogenic dewar. Multiple rounds of Silicon-dioxide deposition and cryogenic measurements were performed on the soldered and mounted QCL chip using PECVD. The tuning of the QCL's single-mode lasing spectrum is shown as a function of the thickness of the deposited oxide. Spectra were measured after each deposition step when the QCL was operated in a liquid-Nitrogen cooled dewar at 78 K in pulsed mode at an operating current of $\sim$ 570 mA (current-density $\sim$ 405 A/cm^2). A net tuning of $\sim$ 57 GHz tuning is demonstrated for an overall deposited thickness of $\sim$ 3700 nm. 65

4.3 (a) Emission frequency of the terahertz QCL with antenna-feedback as a function of the deposited thickness of Silicon-dioxide, expressed as a difference from its original emission frequency of $\sim$ 2.85 THz without any oxide. The QCL is biased slightly below the peak-power bias region where it radiates in a single-mode (detailed spectra with bias are shown in Fig. 4.5). (b) Maximum operating temperature ($T_{\max}$) and the detected peak optical power at 78 K for the QCL in pulsed operation, as a function of the thickness of the Silicon-dioxide. 68

4.4 Frequency difference of resonant lowest loss mode from terahertz QCL with antenna-feedback as a function of the thickness of Silicon-dioxide on top of the cavity from 2D simulations. 69

4.5 Light-current characteristics of the terahertz QCL with antenna-feedback scheme at different heat-sink temperatures. The dimensions of the QCL's cavity are 100 μm $\times$ 1.4 mm $\times$ 10 μm. The QCL is biased in pulsed mode with 400 ns wide pulses repeated at 100 kHz. The plot-insets show lasing spectra at 78 K as a function of increasing bias. (a) Original QCL without any oxide deposition, (b) QCL with 140 nm thick oxide leading to $\sim$ 13 GHz frequency tuning, (c) QCL with 700 nm thick oxide leading to $\sim$ 31 GHz frequency tuning, and (d) QCL with 3700 nm thick oxide leading to the maximum tuning of $\sim$ 57 GHz for the QCL still lasing at 78 K. 71

4.6 (a) Schematic showing orientation of the QCL and definition of angles for the shown far-field radiation patterns. The QCL was operated at 78 K in pulsed mode, and the radiation pattern was measured using a room-temperature pyroelectric detector of 2 mm diameter mounted on a $x - y$ movement stage. The radiation-pattern in (b) is for QCL without Silicon-dioxide deposition, in (c) is for QCL deposited with an oxide thickness of 140 nm, and in (d) is for an oxide thickness of 700 nm. 72

5.1 **Photonic structure 1 (one extra aperture is implemented for alternating grating periods) for second-order DFB at $\sim$ 3 THz.** (a) Eigenmode spectrum for total length of cavity $\sim$ 1.4 mm. (b) Schematic of new structure 1 for second-order DFB at $\sim$ 3 THz. (c) Dominant TM polarized (E_y) electric-field along the whole length of cavity for the lowest loss mode. Right: zoomed in (E_y) electric-field around the center of the cavity. (d) In-plane (E_z) electric-field along the whole length of cavity for the lowest loss mode. Right: zoomed in (E_z) electric-field around the center of the cavity. 78

5.2 Simulated beam pattern of second-order DFB with the new photonic cavity structure 1. 79

5.3 Picture of cryocooler operated at 50 K and copper mount to measure surface-emitting lasers 80
5.4 Measured light-current curve at different heat-sink temperatures of conventional second-order DFB with 100 μm width. Inset: measured spectra at different bias at $\sim$ 55 K. 81
5.5 Measured beam pattern of conventional second-order DFB with 100 μm width. Schematic on the left shows the orientation of QCLs and definition of angles. 82
5.6 Measured light-current curve at different heat-sink temperatures of new photonic structure 1 second-order DFB with 70 μm width. Inset: measured spectra at different bias at $\sim$ 55 K. 83
5.7 Measured beam pattern of second-order DFB with new photonic structure 1 with 70 μm width. 83
5.8 Measured light-current curve at different heat-sink temperatures of new structure 1 second-order DFB with 200 μm width. Inset: measured spectra at different bias at $\sim$ 55 K. 85
5.9 Measured beam pattern of second-order DFB with new photonic structure 1 with 200 μm width. 85

6.1 Schematic shows the unique characteristics of antenna-feedback that there is a coherent SPP mode on top of laser cavity in addition to that inside the cavity. 88

A.1 SEM images for top metal gratings of distributed-feedback. 93
A.2 SEM images for mesa etching profile. 94
A.3 SEM images for oxide layer. 95
A.4 SEM images for sidewall and bottom of cavities covered with metal. 96
A.5 SEM images of fabricated and wire bonded terahertz lasers with lateral loss sections. 97
A.6 SEM images of fabricated and wire bonded terahertz lasers with metal covering sidewall. 98
A.7 Schematic of mask design with each layer on top of each other for distributed-feedback with lateral loss sections. 99
A.8 Mask design with each layer on top of each other for distributed-feedback with metal covering sidewall. 100
A.9 Geometry for 2D simulations. 102
A.10 Finite element mesh for 2D simulations. 103

A.11 3D view of copper mount used for edge emitting devices and surface emitting devices. 105
A.12 3D view of copper mount used for edge emitting devices without cone that can bring the device very close to the dewar's window. 106
A.13 Side and top view of copper mount used for edge emitting devices without cone that can bring the device very close to the dewar's window. 107

Terahertz Plasmonic Lasers with Distributed-Feedback

Abstract

Plasmonic lasers generate coherent surface-plasmon-polaritons (SPPs) and could be realized at subwavelength dimensions in metallic cavities for applications in nanoscale optics. Plasmonic cavities are also utilized for terahertz quantum-cascade lasers (QCLs), which are the brightest available solid-state sources of terahertz radiation (frequency $\sim$ 1 THz - 10 THz, wavelength $\sim$ 300 μm - 30 μm). A long standing challenge for plasmonic lasers that are utilized as nanoscale sources of radiation, is their poor coupling to the far-field radiation. Unlike conventional lasers that could produce directional beams, plasmonic lasers have highly divergent radiation patterns due to their subwavelength apertures.

The primary goal of this thesis is to achieve narrow beam patterns for plasmonic lasers. This thesis theoretically and experimentally demonstrates a new technique for implementing distributed-feedback (DFB) that is distinct from any other previously utilized DFB schemes for semiconductor lasers. The so-termed *antenna-feedback* scheme leads to single-mode operation in plasmonic lasers, couples the resonant SPP mode to a highly directional far-field radiation pattern, and integrates hybrid SPPs in surrounding medium into the operation of the DFB lasers. Experimentally, the antenna-feedback method, which does not require the phase matching to a well-defined effective index, is implemented for terahertz QCLs, and single-mode terahertz QCLs with beam divergence as small as $4^\circ \times 4^\circ$ are demonstrated, which is the narrowest beam reported for any terahertz QCL to-date. Moreover, in contrast to negligible radiative-field in conventional photonic band-edge lasers, in which the periodicity follows the integer multiple of half-wavelength inside active medium, antenna-feedback breaks this integer-limit for the first time and enhances the radiative-field of lasing mode. A comprehensive analysis of antenna-feedback scheme is presented, including theory, design, simulation, and experimental results. Terahertz lasers with narrow-beam emission will find applications for integrated as

well as standoff terahertz spectroscopy and sensing. The antenna-feedback scheme is generally applicable to any plasmonic laser with a Fabry-Pérot cavity irrespective of its operating wavelength, and could bring plasmonic lasers closer to practical applications.

This thesis also demonstrates a new tuning mechanism for plasmonic lasers with distributed-feedback, in which refractive-index of the surrounding medium affects the resonant-frequency of DFB mode in the same vein as refractive-index of gain medium inside the cavity. Reversible, continuous, and mode-hop-free tuning of $\sim$ 57 GHz is realized for single-mode narrow-beam terahertz plasmonic QCLs, which emit at $\sim$ 2.8 THz and operate in a liquid-nitrogen cooled dewar. The tuning is based on post-process deposition/etching of a dielectric (Silicon-dioxide) on a QCL chip that has already been soldered and wire-bonded onto a copper mount. This is a considerably larger tuning range compared to previously reported results for single-mode terahertz QCLs with directional far-field radiation patterns. Also, the tuning is demonstrated at the much more practical operating temperature of $\sim$ 78 K, whereas all previous tuning results for terahertz QCLs have been reported at low-temperatures ($\sim$ 10 K). The key enabling mechanism for tuning is the new antenna-feedback scheme for plasmonic lasers as described in Chapter 2 and 3, which leads to generation of hybrid SPP mode propagating outside the cavity of the laser with a large spatial extent. The effect of dielectric deposition on QCLs' characteristics is investigated in detail including that on maximum operating temperature, peak output power and far-field radiation patterns. Single-lobed beam with low divergence (less than 7°) is maintained through the tuning range, which is the narrowest divergence for any tunable terahertz QCL to-date. The antenna-feedback scheme is ideally suited for modulation of plasmonic lasers due to the sensitive dependence of spectral and radiative properties of the laser on its surrounding medium.

Finally, preliminary work on high-power terahertz QCLs with single-mode operation and single-lobed far-field radiation patterns is reported based on surface-emitting second-order DFB with new photonic designs. Improved outcoupling of radiation from laser's cavity leads to enhanced output power; $\sim$ 50 mW peak output power is realized at $\sim$ 51 K, which is one of the highest reported output powers

from single-mode terahertz QCLs. Higher output power is due to broader emission area and increased radiative field from grating apertures. Better beam quality with single lobe is achieved without any central phase shift in such gratings, which is another advantage of the demonstrated scheme. A comparative study with conventional second-order DFB terahertz QCLs is presented, where such QCLs have lower output power and less desirable radiation patterns with two lobes in the far-field.

Thesis supervisor: Sushil Kumar
Title: Associate Professor

Chapter 1

Introduction

1.1 Terahertz (THz) and its applications

The terahertz frequency range (frequency $\sim$ 1 THz - 10 THz, wavelength $\sim$ 300 μm - 30 μm) of the electromagnetic spectrum as shown in Figure 1.1 has remained relatively unexplored as compared to the neighboring millimeter-wave and infrared spectral ranges, primarily due to the lack of convenient, efficient and high power radiation sources [3]. Many molecules and solids have strong and distinct spectral signatures at terahertz frequencies, which makes terahertz technology important for both science and commercial applications related to spectroscopy and imaging.

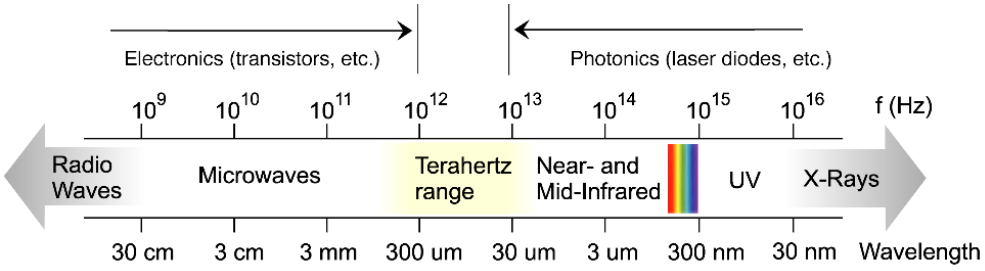

Figure 1.1: The terahertz frequency range in the eletromagnetic spectrum.

Imaging is one of the important applications [4, 5] since the terahertz radiation is

useful for security related chemically-active detection of concealed weapons, drugs, and explosives, even at trace amounts, since many packaging materials such as paper, plastics, and ceramics, which are opaque to visible frequencies, are transmissive at longer wavelengths. Many materials such as clothing and packaging are transparent at terahertz wavelengths, leading to possible applications in non-invasive inspection for industrial and pharmaceutical processes, security screening, mail inspection and biomedical imaging. For imaging, terahertz radiation provides distinct advantages in comparison to radiation at other wavelengths [6, 7, 8]. In comparison to microwaves, terahertz radiation provides a much better spatial resolution for imaging due to its shorter wavelength. When compared to imaging with high energy X-rays, imaging with terahertz radiation is non-invasive, and can provide much better contrast in terms of identification of different materials due to their different absorption and refraction indices in the terahertz frequency.

Interest in biological spectroscopy [9, 10] mainly arises from the fact that many molecules, for example, carbon-monoxide and carbon-dioxide, water, nitrogen, oxygen, to name a few, have strong characteristic rotational and vibrational absorption features in the terahertz, as opposed to the neighboring spectral regions. Also the dielectric resonances that occur due to various conformational and binding states in heavier molecules such as proteins and DNA could be probed in the terahertz region. Additionally, terahertz spectroscopy is relevant in condensed matter physics to study collective effects in materials such as superconductors, and charge density plasmas since the energy scales involved are of the order of 1 meV (for frequency ~ 1 THz, ~ 4 meV).

A multitude of applications for terahertz imaging and spectroscopy exist, be it in the fields of astronomy [11, 12] and remote-sensing and monitoring of earths atmosphere due to the fact that terahertz optical transitions are readily thermally excited due to their low-energies making them ideal for passive emission-spectroscopy. Other applications in electronics and manufacturing include end-point detection in plasma-etching processes and non-invasive inspection of semiconductor wafers. Hence, terahertz technology has applications in areas as diverse as astronomy, security-based imaging and chemical detection, cancer research, label-free DNA sensing,

non-destructive evaluation of pharmaceutical products, and so-forth. All of the aforementioned applications will benefit from compact coherent sources of radiation with narrow beam and high power to enable imaging in real-time, and to enable sensing with large, multi-pixel array detectors operating at room-temperature.

1.2 Quantum cascade lasers (QCLs)

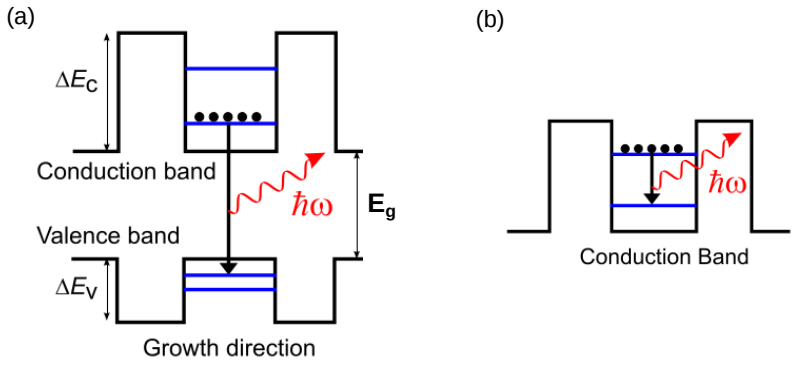

Figure 1.2: Interband versus intersubband optical transitions in two-dimensional quantum wells.

Figure 1.2 shows the comparison between interband and intersubband optical transitions in two-dimensional quantum wells of a semiconductor heterostructure schematically. An interband radiative transition involves an electron-hole recombination. Therefore, an interband laser is inherently bipolar by nature. The frequency of radiation is essentially determined by the bandgap E_g of the quantum well material (of the order of 1 eV or wavelegnth ~ 1.24 μm or frequency ~ 242 THz), while small tuning can be obtained by changing the width of quantum wells. The gain spectrum is typically broad and reflects the thermal distribution of carriers in the conduction and valence bands.

In contrast, intersubband optical transitions are within the subbands of conduction band (or valence band) itself [13]. This has two advantages. First, the radiative frequency can be set by design as a function of the width of the quantum wells.

Theoretically, emission for the radiative energy can be as high as the heterostructure band-offset or to as low as few meVs (and hence frequencies near 1 THz) as long as enough population inversion could be established between the desired subbands. Second, the energy dispersion of each of the subbands track in k space leads to a delta-function like joint density of states at the optical transition energy. This suggests that all inverted carriers should contribute to gain at the same transition energy, indicating that the gain could potentially be very large. However, this feature is offset by the fact that the non-radiative life- times for intersubband transitions are much faster (order of 1 ps) as compared to the non-radiative electron-hole recombination times in an interband diode-laser (order of 1 ns), mostly due to the fast polar longitudinal-optical (LO) phonon intersubband scattering mechanism in semiconductor heterostructures. Hence, small level lifetimes limit the amount of population inversion that can be achieved between the desired subbands. It is for this reason that intersubband lasers are typically made of multiple cascaded modules to obtain enough gain for lasing. The unipolar nature of intersubband transitions makes such a cascading possible.

The first semiconductor superlattice based intersubband laser was invented at Bell Labs in 1994 by J. Faist, F. Capasso, and co-workers [14]. Lasing was obtained at a wavelength of ~ 4.3 μm. This first semiconductor superlattice based intersubband laser was named as - quantum cascade laser(QCL).

Today, high-performance MIR-QCLs covering a wavelength range of ~ 4 μm - 10 μm with continuous-wave (cw) room-temperature operation, and optical power output of the order of 100 mW are available. QCLs that are broadly tunable by the use of external-cavity gratings have been demonstrated. Until now, most high performance MIR-QCLs were demonstrated in the InGaAs/InAlAs alloys on InP and later GaAs/ AlGaAs on GaAs [15].

1.3 Terahertz semiconductor quantum cascade lasers

Even though sensitive terahertz detectors have long existed [16], there has been a lack of compact solid-state terahertz sources that could provide large (larger than 1 mW) radiation intensities in continuous-wave (cw) operation. Output power from electronic sources such as transistors, Gunn oscillators, Schottky-diode frequency multipliers typically falls to micro-Watt levels for frequency larger than 1 THz. Sources such as photo-mixers and parametric-oscillators that utilize optical down-conversion to generate terahertz radiation also have low average power. Conventionally, the only available sources of high average power (larger than 1 mW) narrow-band terahertz (far-infrared) radiation were the gas lasers that utilize an optically pumped molecular gas (such as methane) to obtain laser action. Molecular gas lasers are typically bulky, large (often need to occupy an entire length of an optical table), and very expensive. Also, they are only available at certain discrete frequencies within the terahertz spectrum that restricts their usability for many applications.

In October of 2001, the first terahertz semiconductor quantum-cascade (QC) laser ($\sim$ 4.4 THz, $\sim$ 67 μm) was invented at Scuola Normale Superiore, Pisa, Italy [17]. Terahertz QC lasers are electrically pumped, and emit radiation due to intersubband optical transitions in semiconductor superlattices that could be engineered by design. Rapid progress in their development has followed [18, 19] and they can now match, and in some cases exceed, the performance metrics of molecular gas lasers.

1.4 Terahertz quantum cascade lasers with metal-metal waveguides

1.4.1 Strong terahertz mode-confinement in metal-metal microcavities

Dielectric waveguiding is impractical for terahertz electromagnetic mode confinement because it is difficult to grow thick claddings that are required for terahertz frequencies (thickness of the claddings needs to be of the order of the wavelength). In this case, microstrip-line like structures that are routinely employed in microwave engineering were found to be optimum for guiding the terahertz mode in QC lasers [20, 21, 22]. Parallel-plate metal-metal plasmonic waveguides are the most effective way of confining terahertz radiation from QC lasers owing to the low optical loss in metals at the long-wavelength terahertz frequencies. For such cavities, the vertical dimension is typically much smaller than the wavelength of the confined light (the maximum height of the cavity is limited by how thick of a semiconductor superlattice heterostructure can be grown by molecular beam epitaxy), as shown in Figure 1.3. In this case, the waveguide structure is truly a microcavity in the vertical dimension.

Metal-metal microcavities provide near unity mode confinement even if the lateral dimensions of the cavity become smaller than the wavelength, since the mode remains similar to TEM like for which there is no cutoff condition to prevent guided mode propagation at a particular frequency. The narrow laser cavity is with typical width of ~ 13 μm. An important aspect of such a subwavelength aperture is that there is a large mismatch between the mode shapes inside the waveguide, with one that propagates in free space. Correspondingly, the guided optical mode is tightly confined within the cavity with a mode confinement-factor of close to unity.

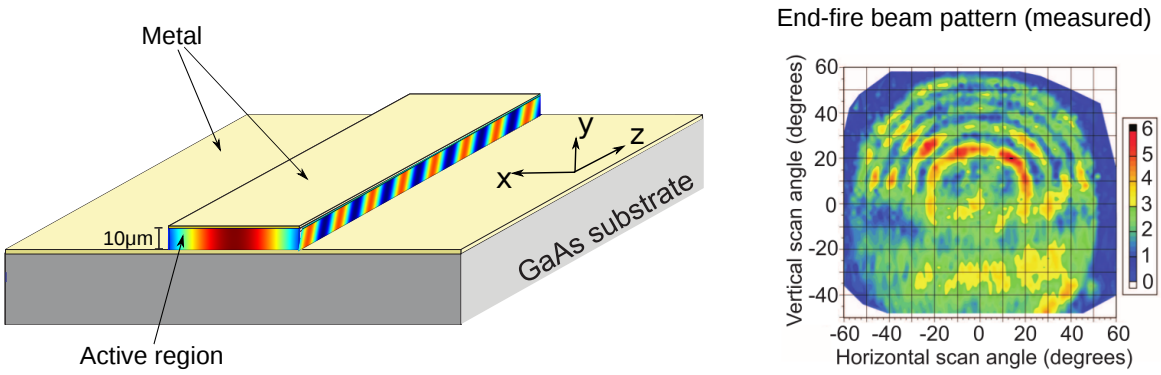

Figure 1.3: Left: Schematic of a metal-metal parallel plate ridge cavity, which confines the terahertz optical mode with very low losses at long wavelengths. Right: Measured far-field beam pattern of such a terahertz QCL [1]. Optical emission is highly divergent with distorted ring-like wavefronts.

1.4.2 Poor emission characteristics of terahertz QCLs with metal-metal microcavities

The best performing terahertz QC lasers utilize metal-metal microcavities, for the reasons explained above. However, the emission properties of such ridge cavity lasers are very poor. First, such lasers easily excite several lateral and longitudinal order modes simultaneously, invariably leading to multi-mode lasing across the gain bandwidth, which is typically up to 0.5 THz around the designed frequency. Also, the lasing modes often switch unpredictably as a function of applied bias. A multi-mode optical spectrum is measured from such a laser. For high-resolution sensing and spectroscopy applications, multi-mode lasing is undesirable and in some cases strictly unacceptable. Second, terahertz QC lasers have very poor beam patterns. Such a highly diffracted beam from a subwavelength aperture shows a ring-like beam pattern due to the microcavity laser acting like a radiating antenna at such long wavelengths [23]. The poor beam patterns make such a laser less attractive for coherent detection since the phase of the electromagnetic field shows a rapid variation spatially and also because the optical power is no longer concentrated in a small area, and hence only a small fraction of the output power could be utilized.

Third, while strong mode confinement reduces the lasers threshold, it also results in small out-coupling of radiation from the end-facets and the low output power.

1.5 Distributed-feedback (DFB)

A single-mode laser is highly desirable for a variety of spectroscopy applications. In order to achieve single frequency emission, an effective method-distributed feedback, is widely used in laser diode, optical fiber laser and quantum cascade lasers here. The structure builds a one-dimensional interference grating (Bragg scattering) and the grating provides optical feedback for the laser, in contrast to a Fabry-Perot lasers, where the facets of the chip form the two mirrors providing the feedback. The grating of distributed-feedback acts as the wavelength selective element, which can be constructed so as to reflect only a narrow band of wavelengths, and thus produce a single longitudinal lasing mode. Feedback can be understood as way of ensuring that part of the optical field passing through a given point returns to this point repeatedly [24]. At short wavelengths, a diffraction grating is fabricated and structured by etching the semiconductor itself. Figure 1.4 is an illustration of a semiconductor laser cavity with a periodic grating which we will use to describe the distributed-feedback (DFB) scheme. Any aspect of a cavity that periodically perturbs the propagating electromagnetic mode leads to Bragg diffraction of the wave inside the cavity. For a wave propagating from left to right with a wavevector k_{wg} ($k_{wg} = 2\pi n_{\mathrm{a}}/\lambda$ for a plane-wave, where n_{a} is the refractive index of the active medium and λ is the free-space wavelength), a wave is diffracted inside the cavity for which we can write the Bragg condition

$$k_{wg} \;=\; p\frac{2\pi}{\Lambda} - k_{wg} sin(\theta_{wg}) \tag{1.1}$$

where $2\pi/\Lambda$ is the grating wavevector, p is an integer (p = 1, 2, 3 . . .) that specifies the diffraction order, and θ_{wg} is the angle of diffraction.

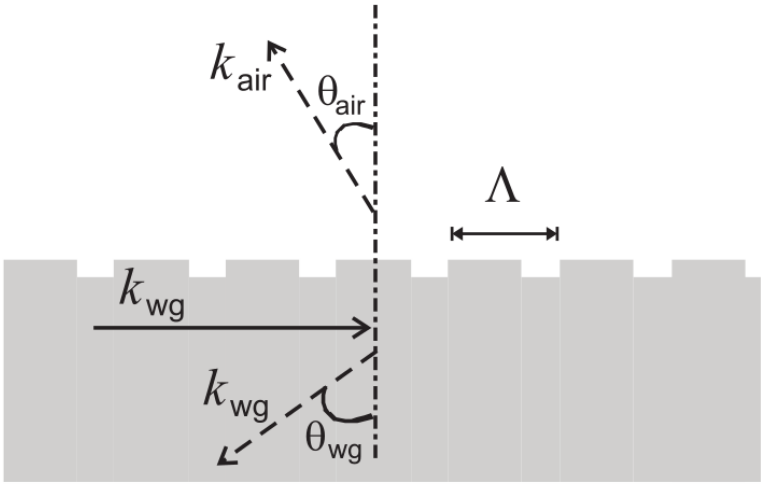

Figure 1.4: Schematic of a distributed Bragg grating implemented in a semiconductor gain medium to improve spectral and modal characteristics of laser cavities.

1.6 Terahertz QCLs with traditional distributed-feedback

Figure 1.5 shows the simulation results for THz QCLs with traditional distributed-feedback, where a second-order DFB cavity is shown as an example. A periodic grating is implemented in the top metal cladding for a parallel-plate metallic cavity by choosing the appropriate periodicity. Laser mode has the maximum amplitude at the interface of metal and dielectric active medium, so that a periodic perturbation in the metal layer could provide strong Bragg diffraction. In a second-order DFB, the first order Bragg diffraction provides the surface emission, while the periodic grating provides distributed-feedback due to the second order Bragg diffraction, i. e. p = 2 in equation (1.1) for $\theta_{wg} = \pi/2$ inside the cavity. Hence, a mode which is exactly periodic with the grating is the one that is excited due to its lowest loss. Note that the DFB structure could also be considered as a one-dimensional photonic crystal in which the above mode is the one at the top of the lower band-edge of the

eigenmode dispersion profile of the photonic crystal. The periodicity of the electric-field along the grating could also be seen from the field distribution in Figure 1.5. For dominant electric field of the lowest loss mode, each grating period is composed of one minimum and one maximum field distribution, serving as a clear feature of second-order DFB, while in-plane electric field is null under all grating apertures.

Experimentally, THz QCLs with second-order DFB cavity achieves the first single-mode terahertz QC laser in a metal-metal microcavity that lased in cw operation with a single-lobed beam-pattern [25]. To-date, this remains the best performing single-mode terahertz QC laser in terms of operating temperature (although, similar operating temperature has also recently been realized in only pulsed mode), and is one of the two reported THz QCLs DFB results which operate in cw mode at the temperature of liquid-Nitrogen (77 K) [26].

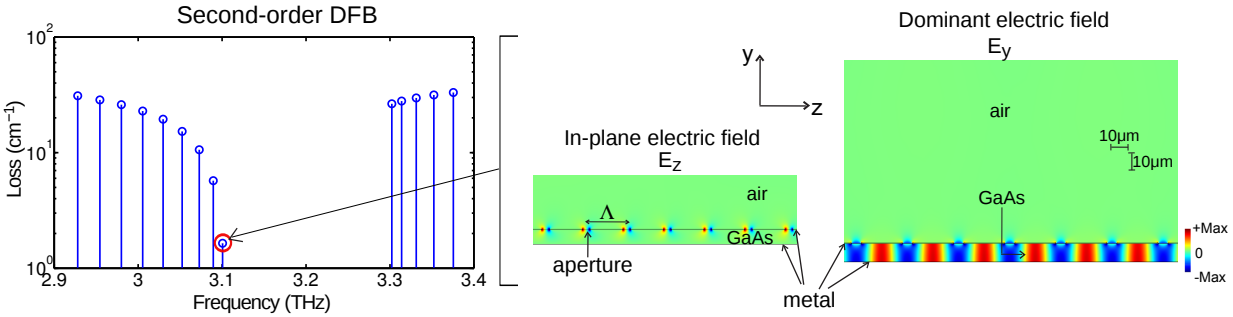

Figure 1.5: Simulation results for second-order DFB. From left to right: the eigenmode spectrum of conventional second-order DFB, in-plane electric field and dominant electric field of the lowest loss mode.

1.7 Overview

This thesis consists of 6 Chapters and is organized as follows. Chapter 1 gives an overview of terahertz frequency range and its main applications. Then the logical flow follows the introductions of quantum-cascade lasers (QCLs), terahertz

quantum-cascade lasers, terahertz quantum-cascade lasers with metal-metal waveguide and their corresponding emission characteristics, distributed-feedback (DFB) scheme generally utilized in semiconductors and specifically utilized in terahertz quantum-cascade lasers, simulation results of terahertz QCLs with second-order DFB are shown as an example. Chapter 2 focuses on description of the new antenna-feedback scheme developed for plasmonic lasers and terahertz quantum cascade lasers towards the primary goal of this thesis - narrow beam pattern from such lasers. A detailed theoretical study, simulation results and experimental results are presented. Fabrication process and experimental setup are demonstrated in this chapter as well. Chapter 3 establishes a comprehensive analysis of antenna-feedback for terahertz quantum-cascade lasers by both 2D and 3D simulations. Extensive finite-element simulations were used in the design process of various photonic structures and in the pursuit of optimized parameters. Chapter 4 describes a unique and novel tuning mechanism based on metal-clad plasmonic lasers with antenna-feedback. Post-process deposition/etching of a dielectric (Silicon-dioxide) on a QCL chip that has already been soldered and wire-bonded onto a copper mount was developed to improve tuning range significantly. Experimental results show that refractive-index of the lasers surrounding medium affects the resonant-frequency of DFB mode sensitively and dramatically. A large, reversible, continuous, and mode-hop-free tuning for single-mode narrow-beam terahertz plasmonic quantum-cascade lasers (QCLs) operated in a liquid-nitrogen cooled dewar are demonstrated. Second-order DFB with broader emission area can be very useful for surface-emitting lasers. Theoretical investigations for improved outcoupling loss and radiative field by 2D simulations from surface-emitting lasers are included in Chapter 5. A new photonic structure has been developed in Chapter 5 to experimentally achieve higher output power and better beam quality of single-lobed from such lasers. Chapter 6 makes a summary of plasmonic lasers with the new antenna-feedback to achieve ultra-narrow beam patterns and a large frequency tuning range, together with new surface-emitting distributed feedback to achieve higher power performance, serving as the primary goals of this thesis. A brief introduction of integrating antenna-feedback scheme into terahertz sensors and phase-locked laser arrays is presented in

the section of future outlook.

Chapter 2

Terahertz plasmonic lasers radiating in an ultra-narrow beam

2.1 Introduction

A surface-plasmon-polariton (SPP) is a coupled state between electromagnetic (EM) field and electron plasma oscillations at the interface between a metal and a dielectric, for which the EM field could be confined in subwavelength dimensions normal to the surface of metal. Consequently, metallic cavities supporting SPP modes have been used to realize SPP lasers (also known as plasmonic lasers or spasers) with subwavelength dimensions [27, 28, 29, 30, 31]. The energy in a spaser can remain confined as coherent SPPs or it can be made to leak out from the spaser as radiation. In many targeted applications in integrated optics and nanophotonics, spasers are developed as nanoscale sources of coherent electromagnetic (EM) radiation and show interesting properties such as ultrafast dynamics for applications in high-speed optical communications. Parallel-plate metallic cavities supporting SPP modes are also utilized for terahertz quantum-cascade lasers (QCLs) [17] to achieve low-threshold and high-temperature performance [32] owing to the low-loss of SPP modes at terahertz frequencies that are much smaller than the plasma frequency in metal. The most common type of plasmonic lasers with long-range SPPs, which

include terahertz QCLs, utilize Fabry-Pérot type cavities in which at least one dimension is longer than the wavelength inside the dielectric [33, 34, 35, 22]. One of the most important challenges for such plasmonic lasers is their poor coupling to free-space radiation modes owing to the subwavelength mode confinement in the cavity, which leads to small radiative efficiency and highly divergent radiation patterns. This problem is also severe for terahertz QCLs based on metallic cavities and leads to low-output power and undesirable omnidirectional radiation patterns from Fabry-Pérot cavities [1, 23].

A possible solution to achieve directionality of far-field emission from spasers is to utilize periodic structures with broad-area emission, which has been used for both short-wavelength spasers [36, 37, 38, 39, 40, 41] as well as terahertz QCLs [42, 43]. On chip phased-locked arrays [44, 45] or metasurface reflectors composed of multiple cavities [46] have also been utilized for directional emission in terahertz QCLs. However, edge-emitting Fabry-Pérot cavity structures with narrow cavity widths are more desirable, especially for electrically pumped spasers to achieve small operating electrical power and better heat removal from the cavity (along the width of the cavity in lateral dimension, through the substrate) for continuous-wave (cw) operation. In this chapter, we theoretically and experimentally demonstrate a new technique for implementing distributed-feedback (DFB) in plasmonic lasers with Fabry-Pérot cavities, which is termed as an *antenna-feedback* scheme. This DFB scheme has no resemblance to the the multitude of DFB methods that have been conventionally utilized for semiconductor lasers. The key concept is to couple the guided SPP mode in a spasers cavity to a single-sided SPP mode that can exist in its surrounding medium by periodic perturbation of the metallic cladding in the cavity. Such a coupling is possible by choosing a Bragg grating of appropriate periodicity in the metallic film. This leads to excitation of coherent single-sided SPPs on the metallic cladding of the spaser, which couple to a narrow-beam in the far-field. The narrow beam emission is due in part to the cavity acting like an end-fire phased-array antenna at the microwave frequencies, as well as due to the large spatial extent of a coherent single-sided SPP mode that is generated on the metal film as a result of the feedback scheme. Experimentally, the antenna-feedback method is implemented

for terahertz QCLs for which the method is shown to be an improvement over the recently developed third-order DFB scheme for producing directional beams [47] since it does not require any specific design considerations for phase-matching [48]. The emitted beam is more directional and the output power is also increased due to increased radiative field by virtue of this specific scheme.

2.2 New antenna-feedback scheme for plasmonic lasers

Single-mode operation in spasers with Fabry-Pérot cavities could be implemented in a straightforward manner by periodically perturbing the metallic film that supports the resonant SPP modes. The schematic in Fig. 2.1(a) shows an example of a periodic grating in the top metal cladding for a parallel-plate metallic cavity that could be utilized to implement conventional p-th order DFB by choosing the appropriate periodicity. Since the SPP mode has maximum amplitude at the interface of metal and dielectric active medium, a periodic perturbation in the metal film could provide strong Bragg diffraction up to high-orders for the counter-propagating SPP waves inside the active medium with incident and diffracted wavevectors k_i and $k_d = -k_i$ respectively, such that

$$k_i \;=\; p\frac{2\pi}{\Lambda} + k_d \tag{2.1}$$

where Λ is the grating period, $2\pi/\Lambda$ is the grating wavevector, and p is an integer ($p = 1, 2, 3\ldots$) that specifies the diffraction order. For plane-wave like modes at frequencies far away from the plasma resonance in metal, $k_i \approx 2\pi n_\mathrm{a}/\lambda$, where λ is the free-space wavelength corresponding to the SPP mode and n_a is the effective propagation index in active medium (approximately the same as refractive index of the medium), the so-called Bragg mode with $\lambda = 2n_\mathrm{a}\Lambda/p$ is resonantly excited because it is, by design, the lowest-loss mode in the DFB cavity within the gain spectrum of the active medium. For terahertz QCLs with metallic cavities, first-order [49] and

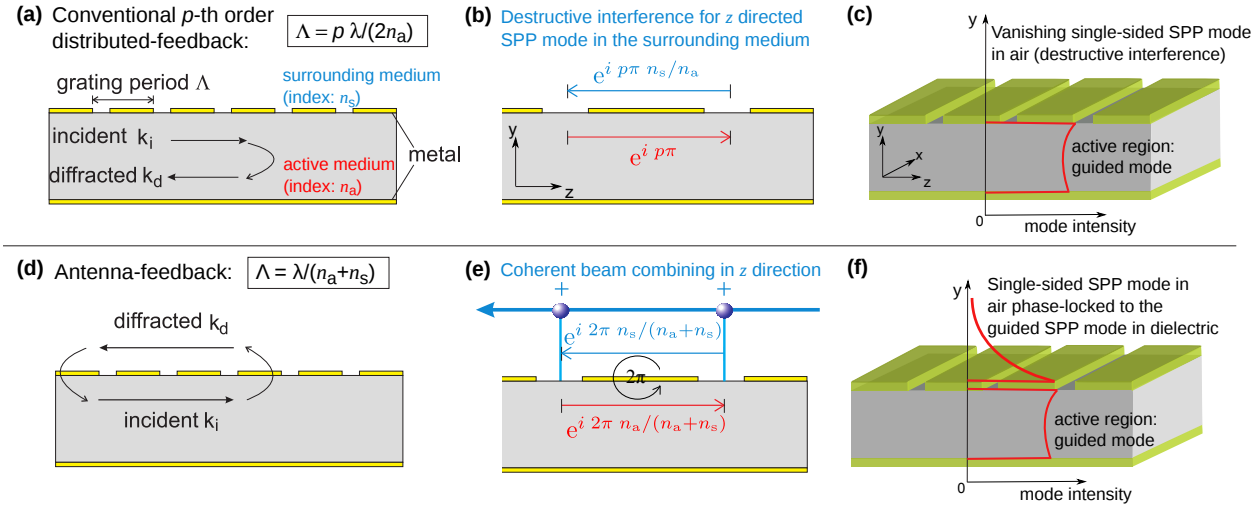

Figure 2.1: The antenna-feedback concept for plasmonic lasers. (a) The general principle of conventional distributed-feedback (DFB) that could be implemented in a spaser by introducing periodicity in its metallic cladding. A parallel-plate metallic cavity is illustrated; however, the principle is equally applicable to spaser cavities with a single metal-cladding. (b) If the periodicity in (a) is implemented by making holes or slits in the metal-cladding, the guided SPP wave diffracts out through the apertures and generates single-sided SPP waves on the cladding in the surrounding medium. The figure shows phase-mismatch between successive apertures for SPP waves on either side of the cladding. Coherent single-sided SPP waves in the surrounding medium cannot therefore be sustained owing to destructive interference with the guided SPP wave inside the cavity, as illustrated in (c). (d) Principle of an antenna-feedback grating. If the periodicity in the metal film allows the guided SPP mode to diffract outside the cavity, a grating period could be chosen that leads to the first-order Bragg diffraction in the opposite direction, but in the surrounding medium rather than inside the active medium itself. Similarly, the single-sided SPP mode in the surrounding medium undergoes first-order Bragg diffraction to couple with the guided SPP wave in the opposite direction inside the cavity. (e) The grating in (d) leads to a fixed phase-condition at each aperture between counter propagating SPP waves on the either side of metal-cladding. First, this leads to significant build up of amplitude in the single-sided SPP wave in the surrounding medium, as illustrated in (f). Second, emission from each aperture adds constructively to couple to far-field radiation in the end-fire (z) direction. As argued in the text, both of these aspects lead to narrow far-field emission profile in the $x-y$ plane.

second-order [50, 25] DFBs have been implemented to achieve robust single-mode operation. However, these conventional DFB techniques do not achieve directionality of far-field radiation in both directions. There is phase mismatch for SPP waves on either side of metal claddings and destructive interference between successive apertures, as shown in Fig. 2.1(b) for propagating SPP waves. Therefore, no coherent single-sided SPP waves can be established on the metallic cladding in the surrounding medium as demonstrated in Fig. 2.1(c). Consequently, 2D photonic-crystal DFB structures have been utilized for broad-area (surface) single-mode emission [51, 52] for which diffraction-limited beams could be achieved at the expense of large cavity dimensions.

In contrast to conventional DFB methods in which periodic gratings couple forward and backward propagating waves inside the active medium itself, the antenna-feedback scheme couples a single-sided SPP wave that travels in the surrounding medium with the SPP wave traveling inside the active medium as illustrated in Fig. 2.1(d). The SPP wave inside the active medium with incident wavevector $k_i \approx 2\pi n_\mathrm{a}/\lambda$ is diffracted in the opposite direction in the surrounding medium with wavevector $k_d \approx -2\pi n_\mathrm{s}/\lambda$. For the first-order diffraction grating ($p = 1$), equation (2.1) results in

$$\frac{2\pi n_\mathrm{a}}{\lambda} = \frac{2\pi}{\Lambda} - \frac{2\pi n_\mathrm{s}}{\lambda} \tag{2.2}$$

that leads to excitation of a DFB mode with $\lambda = (n_\mathrm{a} + n_\mathrm{s})\Lambda$, which is different from any of the p-th order DFB modes that occur at $\lambda = 2n_\mathrm{a}\Lambda/p$. Hence, the antenna-feedback mode could always be excited by just selecting the appropriate grating period Λ such that the wavelength occurs close to the peak-gain wavelength in the active-medium. For GaAs/AlGaAs based terahertz QCLs, $n_\mathrm{a} \sim 3.6$, $n_\mathrm{s} = 1$, and hence for a chosen grating-period Λ, the first-order DFB, antenna-feedback, and second-order DFB modes occur at wavelengths 7.2 Λ, 4.6 Λ, and 3.6 Λ respectively. The typical gain-bandwidth of terahertz QCLs is less than 20% of the peak-gain wavelength, which suggests that the grating has to be designed specifically to excite the antenna-feedback mode.

The antenna-feedback scheme leads to excitation of a coherent single-sided SPP

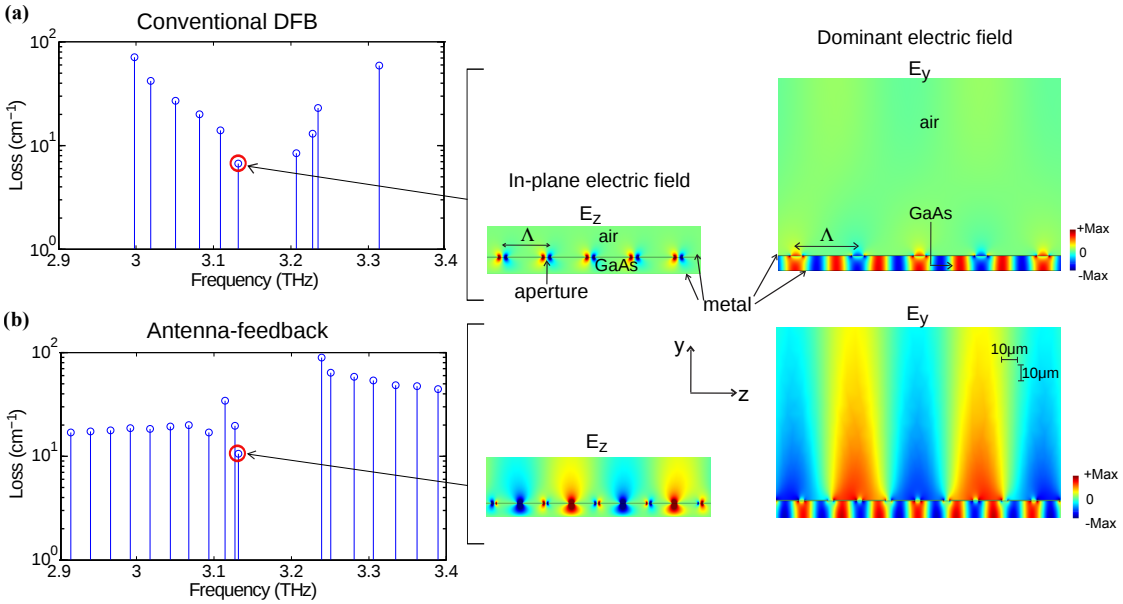

Figure 2.2: Comparison between conventional DFB (third-order DFB as an example) and antenna-feedback schemes for terahertz QCL cavities. The figure shows SPP eigenmode spectrum and electric-field for the eigenmode with lowest loss calculated by finite-element simulations of parallel-plate metallic cavities as in Fig. 2.1, with GaAs as dielectric ($n_a = 3.6$) and air as surrounding medium ($n_s = 1$). Simulations are done in 2-D (i. e. cavities of infinite-width) for 10 μm thick and 1.4 mm long cavities, and metal and active-layers are considered lossless. A periodic grating with apertures of (somewhat arbitrary) width 0.2Λ in the top-metal cladding are implemented for DFB. Λ is chosen to excite the lowest-loss DFB mode at similar frequencies close to ~ 3 THz. The eigenmode spectrum shows frequencies and loss for the resonant-cavity modes, which reflects combination of radiation loss and the loss at longitudinal absorbing regions. Radiation loss occurs through diffraction from apertures, and the amplitude of in-plane electric-field E_z is indicative of the outcoupling efficiency. The major fraction of EM energy for the resonant modes exists in TM polarized (E_y) electric-field. A photonic bandgap in the eigenmode spectrum is indicative of DFB effect due to the grating. The antenna-DFB grating excites a strong single-sided SPP standing-wave on top of the metallic grating (in air) as also illustrated in Fig. 2.1(f). Also, the radiative loss for the third-order DFB grating is smaller since the lowest-loss eigenmode has zeros of E_z under the apertures, which leads to smaller net outcoupling of radiation. The loss is ~ 6.7 cm^{-1} and ~ 10.6 cm^{-1} for the lowest loss resonant cavity mode of third-order DFB and antenna-feedback scheme, respectively.

standing-wave on the metallic cladding of the spaser, which is phase-locked to the resonant-cavity SPP mode inside the active medium as shown in Fig. 2.1(f). Both waves maintain exact same phase relation at each aperture location, where they exchange electromagnetic (EM) energy with each other due to diffraction as illustrated in Fig. 2.1(e). The SPP wave in the surrounding medium is excited due to scattering of EM field at apertures that generates a combination of propagating quasi-cylindrical waves and SPPs [53, 54] that propagate along the surface of the metal-film. The scattered waves thus generated at each aperture superimpose constructively in only the end-fire (z) direction owing to the phase-condition thus established at each aperture. For coupling to far-field radiation, the radiation is therefore analogous to that from an end-fire phased array antenna that produces a narrow beam in both x and y directions.

A third-order DFB technique was recently shown to achieve emission in a narrow beam for terahertz QCLs with Fabry-Pérot cavities [47]. It can achieve high directionality for the radiated beam in both directions perpendicular to propagation, so long as the effective propagation index of the SPP wave inside the active medium could be made ~ 3.0 by complex deep dry etching in the slits [47] or lateral corrugated geometry [26]. The so-called phase matching condition is possible for GaAs-based QCLs by cavity engineering [48] since the $n_{\mathrm{GaAs}} \sim 3.6$ is close to 3.0. The antenna-feedback technique in this work offers similar outcome as a perfectly matched third-order DFB with improved directionality as well as a novel outcoupling mechanism of the radiated beam from terahertz QCLs. It is to be noted that the antenna-feedback scheme is automatically phase-matched and hence it could be utilized for any type of spaser without any restrictions on the required index in the active medium.

2.3 Simulation results

Fig.2.2 shows comparison of the eigenmode spectrum of a terahertz QCL cavity with conventional DFB, taking third-order DFB as an example versus antenna-feedback

gratings computed using a finite-element solver [2]. Fig. 2.2(a) shows results from a third-order DFB grating with $\Lambda = 41.7$ μm and (b) shows results from antenna-feedback grating with $\Lambda = 21.7$ μm. The occurrence of band-gaps in the spectra is indicative of the DFB effect. In both cases, the lower-frequency band-edge mode is the lowest-loss mode by way of DFB action, since the DFB modes result in a standing-wave being established along the length of the cavity with an envelope shape that vanishes close to the longitudinal boundaries (end-facets). In both cases, lossy sections are implemented in the cavities at both longitudinal ends of the cavity to implement absorbing boundaries, which eliminates reflection of guided SPP modes from the end-facets. As can be seen from the field-plot of the band-edge mode in Fig. 2.2(b), for antenna-feedback grating, a standing-wave for the single-sided SPP wave is additionally established in air. In contrast, third-order DFB leads to negligible amplitude of the single-sided SPP wave in air, as mentioned previously and illustrated schematically in Fig. 2.1(c). For the dominant TM polarized (Ey) electric field of antenna-feedback, the hybrid SPPs mode bound to the top metal layer consists of both quasi-cylindrical waves and SPPs, which are evanescent-field with a free-space propagation constant. Particularly at long wavelengths, such as mid infrared and THz region, SPPs and quasi-cylindrical waves complexly mix with each other [53], contributing to the large spatial extent of SPP mode in surrounding medium as shown in Fig. 2.2(b), which does not exist for any conventional DFB, such as first-order, second-order and third-order DFB. In addition, hybrid SPPs on top of metallic grating and standing-wave inside laser cavity show clearly different periodicity, with the ratio of free space wavelength over guided wavelength, which further confirms that the excitation of the coherent SPP wave on both side of top metallic surface contribute to feedback and coupling mechanism with antenna-feedback scheme. The absorbing boundaries at the longitudinal ends of the cavity [55] increase the relative loss of the modes that are further away from the band-edge mode, which helps in mode discrimination and will lead to excitation of the desired band-edge mode for single-mode operation of the spaser. The active region and metal layers are modeled as lossless since the exact loss contribution due to each is not clear in literature for terahertz QCLs at cryogenic temperatures. If lossy metal

is used, the relative loss of various resonant modes for the DFB cavities are not impacted and neither are the mode-shapes and the corresponding resonant frequencies. For the band-edge modes in Fig. 2.2(a) and Fig. 2.2(b), a loss of ~ 5 cm^{-1} was estimated as a contribution from the absorbing boundaries. Consequently, the radiative (outcoupling) loss of of the third-order DFB is ~ 1.7 cm^{-1} as compared to ~ 5.6 cm^{-1} for the antenna-feedback. The radiative loss of the third-order DFB is smaller since the band-edge mode has zeros of the radiative field (E_z) being located at each aperture, since the grating period Λ is integer multiple of half-wavelengths in the GaAs/AlGaAs active medium ($\Lambda = 3\lambda_{\mathrm{GaAs}}/2$, where $\lambda_{\mathrm{GaAs}} \equiv \lambda/n_{\mathrm{GaAs}}$). Such a low-outcoupling efficiency is also existent in surface-emitting terahertz QCLs with second-order DFB [25]. For the cavity with antenna-feedback, the radiative loss is higher because the grating period is not an integer multiple of half-wavelengths inside the active medium ($\Lambda \sim 0.78\lambda_{\mathrm{GaAs}}$) that leads to large amplitudes of the radiative-field (E_z) in alternating apertures as shown in the figure. As a consequence, the output power from terahertz QCLs with antenna-feedback should be greater than that with conventional DFB gratings, which is an additional advantage of the antenna-feedback scheme for terahertz QCLs. This was also verified experimentally from the measured output power. The recently developed second-order DFB QCLs with graded periodicity [56] achieve high-power emission for the same reason, i. e. non-zero radiative field under the metallic apertures.

2.4 Fabrication of antenna-feedback for THz QCLs

The active-medium of the QCLs is based on a three-well resonant-phonon design with GaAs/$Al_{0.10}Ga_{0.90}$As superlattice (design RTRP3W197, wafer number VB0464), which is described in Ref. [57], and was grown by molecular-beam epitaxy. The QCL superlattice is 10 μm thick with an average n-doping of 5.5×10^{15} cm^{-3}, and surrounded by 0.05 μm and 0.1 μm thick highly-doped GaAs contact layers at 5×10^{18} cm^{-3} on either side of the superlattice. Fabrication of QCLs with parallel-plate metallic cavities followed a Cu-Cu thermocompression wafer bonding technique

as in Ref. [25] with standard optical contact lithography. Following wafer-bonding and substrate removal, as shown in Fig. 2.3, positive-resist lithography was used to selectively etch away the 0.1 μm thick highly-doped GaAs layer from all locations where top-metal cladding would exist on individual cavities except in ~ 5 μm wide regions at the outer rectangular boundaries of the top-metal layer due to overlapping mask layers. The removal of this layer beneath the top-metal does not impact electrical transport significantly except adding a small voltage drop at the top contact during QCL operation. Importantly, this lithography step allows radiative outcoupling from the apertures in the finally fabricated QCL cavities; and simultaneously serves to implement longitudinal and lateral absorbing boundaries as illustrated in Fig. 2.7(a) by leaving the highly-doped GaAs layer exposed at both longitudinal and lateral edges of the QCL cavity. The absorbing boundaries result in a highly lossy propagation of the SPP modes in those regions [55]. While the longitudinal boundaries help in DFB mode discrimination, the lateral boundaries are useful to eliminate higher-order lateral guided modes by making them more lossy in comparison to the fundamental mode [25, 51, 47].

Ti/Au metal layers of thickness 25/200 nm were used as the top metal cladding, using an image-reversal lithography mask for implementing gratings in the metal layers, as shown in Fig. 2.4. Another positive-resist lithography step was used to cover the grating-metal with photoresist to be used as a mask for wet-etching of ridges in a H_2SO_4:H_2O_2:H_2O 1:8:80 solution for $\sim$ 22 minutes. After etching the 10 μm thick superlattice active region when the bottom metal layer is exposed, an over-etch of ~ 1 minute was followed up to reduce the slope on the sidewalls of the QCL's cavities to allow for a more uniform current-density distribution through the height of the cavity (in y direction). A Ti/Au contact was used as the backside-metal contact for the finally fabricated QCL chips to assist in soldering. Before deposition of backside-metal of the wafer, the substrate was mechanically polished down to a thickness of ~ 170 μm to improve heat-sinking.

For measurements, a cleaved chip consisting of QCLs with antenna-feedback gratings of different periods along with some Fabry-Pérot ridge QCLs and third-order DFB QCLs was In-soldered on a Cu block as shown in Fig. 2.5 , the QCL to

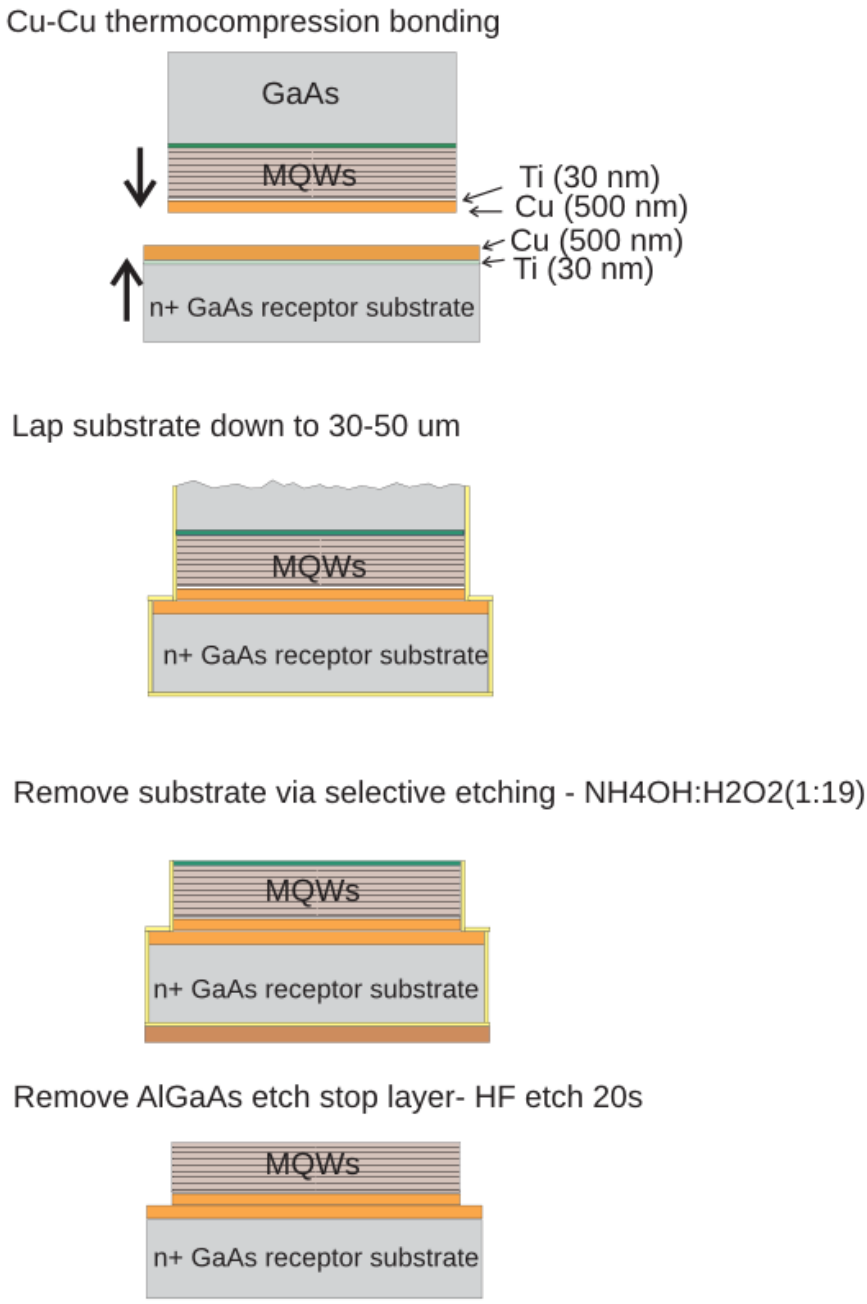

Figure 2.3: Schematic of fabrication steps for THz QCLs with distributed-feedback (part1).

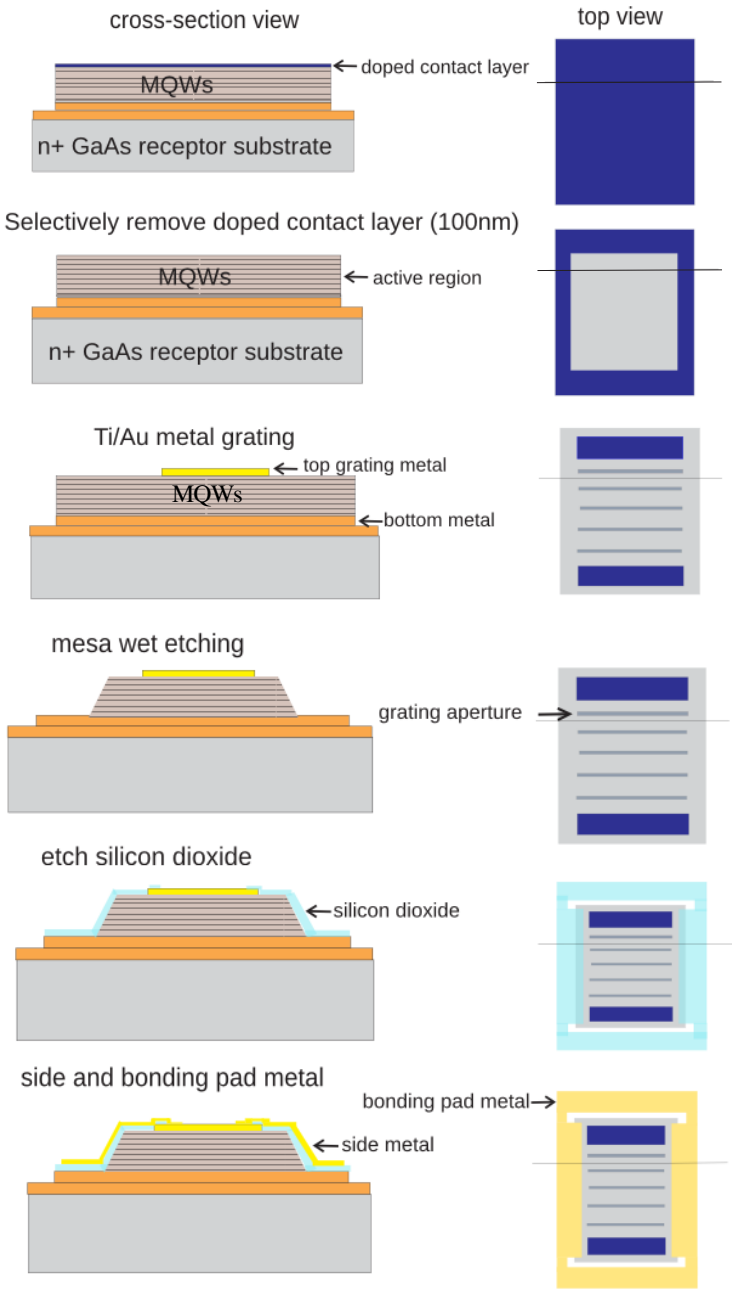

Figure 2.4: Schematic of fabrication steps for THz QCLs with distributed-feedback (part2).

be tested was wire-bonded for electrical biasing, and the Cu block was mounted on the cold-stage of a liquid Nitrogen vacuum cryostat for measurements. Initial measurements of the fabricated QCL cavities did not yield lasing devices at 78 K. It was then realized that the ~ 13 μm wide lateral absorbing boundaries on each side were perhaps introducing high optical losses in the cavities. The finally fabricated wafers were then etched again (post-fabrication) in a H_2SO_4:H_2O_2:H_2O 1:8:80 solution for ~ 15 seconds, which is likely to etch away most of the exposed highly-doped GaAs layer. However, ~ 5 μm wide highly-doped GaAs layer remains unetched underneath the top-metal cladding on all four outer boundaries of the cladding, which serves to perform the role of an absorbing region. The post-etched devices lased upon re-testing, and their robust single-mode operation suggests that both lateral and longitudinal absorbing boundaries were able to suppress undesired resonant-modes in the cavity as desired.

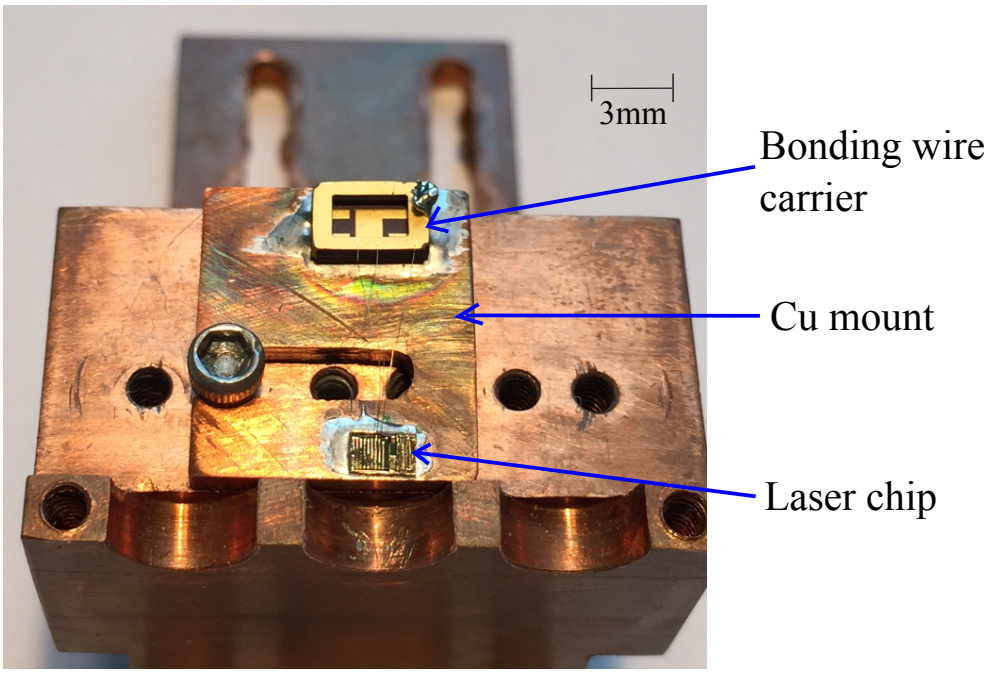

Figure 2.5: Picture of laser chip on a Cu mount.

The emitted optical power was measured with a deuterated triglycine sulfate pyroelectric detector (DTGS) and calibrated with a terahertz thermopile powermeter (ScienTech model AC2500H) without any optical component or cone collecting optic inside the cryostat to improve collection of radiated power in the case of DFB QCLs. (A Winston cone was used to collect power, but only for the Fabry-Pérot-cavity QCL reported in Fig. 2.11.) Polymethylpentene (TPX) is used as the window material of liquid Nitrogen cooled dewar (Infrared Lab Inc. HDL-5 dewar system). TPX is optically transparent in UV, visible and THz ranges. Index of refraction is ~ 1.46 and is relatively independent on wavelength. For example, at wavelength of 300 μm, index of refraction of TPX is ~ 1.46 (Source: TYDEX Company). Losses are very low up to mm-wavelengths. TPX has excellent heat resistance and is highly resistant to most organic and inorganic commercial chemicals. The spectra were measured at 78 K in linear-scan mode with a resolution of 0.2 cm^{-1} (6 GHz) using a Bruker Fourier-transform infrared spectrometer (FTIR) under vacuum, with a room-temperature DTGS detector placed inside the FTIR. The experimental setup is shown in Fig. 2.6. Far-field radiation patterns were measured with a DTGS pyroelectric cell detector mounted on a computer-controlled two-axis ($x - y$ plane) moving stage in the end-fire (z) direction at a distance of 65 mm from the QCLs' end-facets as shown in Fig. 2.8. The detector's size leads to spatial averaging of the measured beam with a step-size of 1.7°, which has a negligible impact on the measured beam-width.

2.5 Experimental demonstration of antenna-feedback for THz QCLs

Fig. 2.7 shows experimental results from terahertz QCLs implemented with antenna-feedback gratings. Details about fabrication and measurement methods are presented above. Fig. 2.7(b) shows representative L-I curves versus heat-sink temperature for a QCL with $\Lambda = 24$ μm. The QCL operated up to a temperature of 124 K. In comparison, multi-mode Fabry-Pérot cavity QCLs on the same chip that did

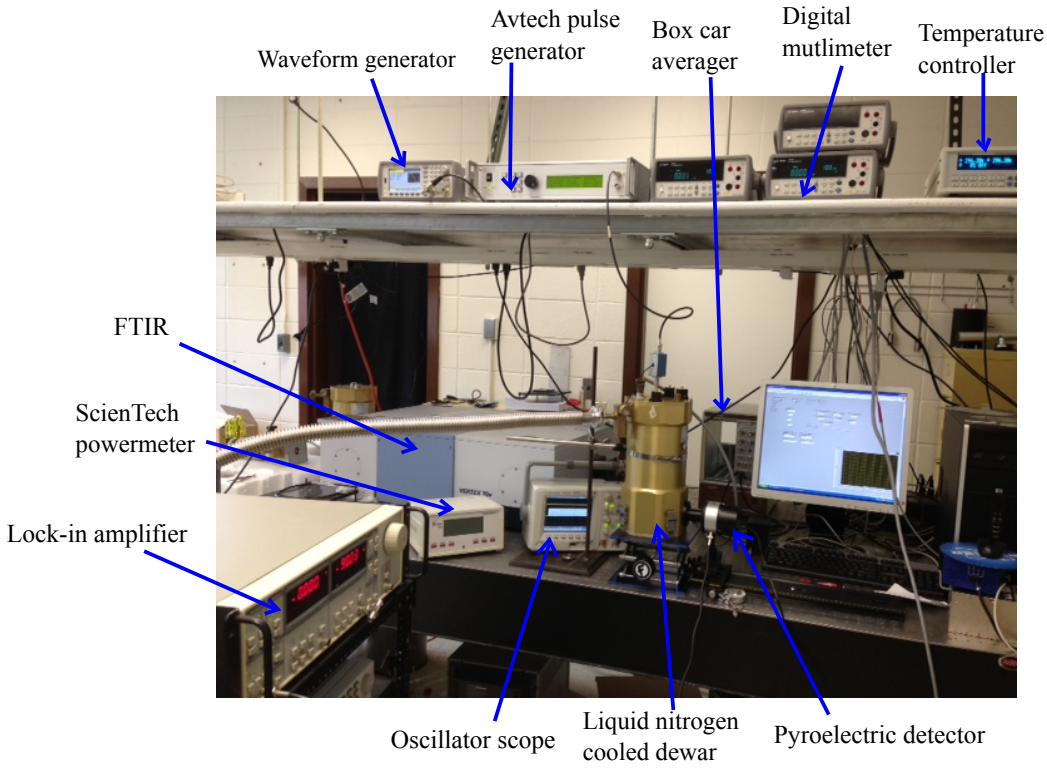

Figure 2.6: Experimental setup for measurements of THz QCLs.

not include longitudinal or lateral absorbing boundaries operated up to $\sim$ 140 K. Light-current characteristics and spectra at different bias with Fabry-Pérot cavity are shown in section 2.6. The temperature degradation due to absorbing boundaries is relatively small and similar to previous reports of DFB terahertz QCLs [25]. The inset shows measured spectra at different bias at 78 K. Most QCLs tested with different grating periods showed robust single-mode operation except close to peak-bias when a second-mode was excited for some devices at a shorter-wavelength, which suggests it is likely due to a higher-order lateral model being excited due to spatial-hole burning in the cavity. Peak-power output of $\sim$ 1.5 mW was detected from the antenna-feedback QCL measured directly at the detector without using any collecting optics. For comparison, a terahertz QCL with third-order DFB (without phase matching) and similar dimensions was also fabricated on the same chip, which operated up to a similar temperature of $\sim$ 124 K and emitted peak-power output

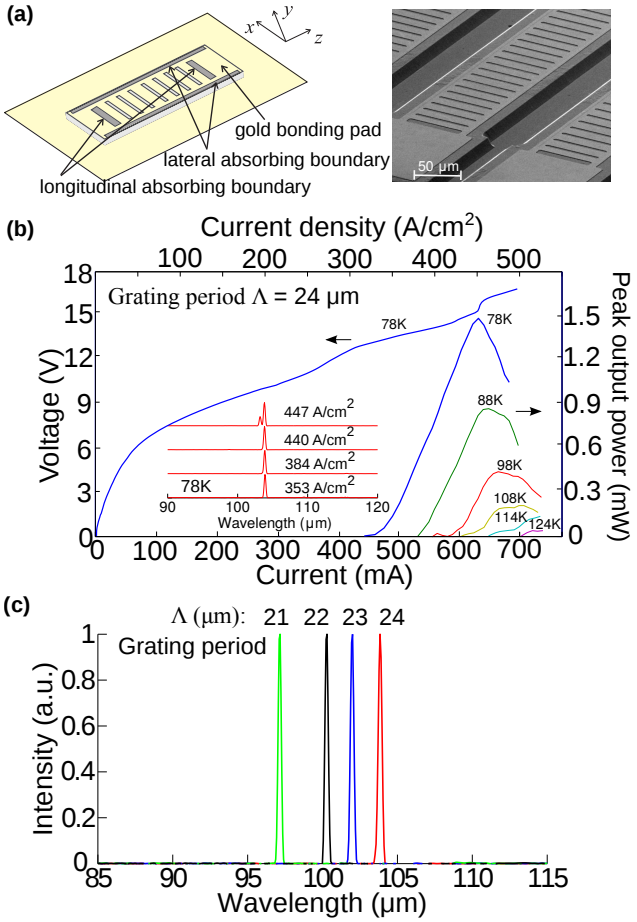

Figure 2.7: Lasing characteristics of terahertz QCLs with antenna-feedback. (a) The schematic on left shows the QCL's metallic-cavity with antenna-feedback grating implemented in top metal cladding. The active-medium is 10 μm thick and based on a 3 THz GaAs/$Al_{0.10}Ga_{0.90}As$ QCL design. A scanning-electron microscope image of the fabricated QCLs is shown on the right. (b) Experimental light-current-voltage characteristics of a representative QCL with antenna-feedback of dimensions 1.4 mm $\times$ 100 μm at different heat-sink temperatures. The QCL is biased with low duty-cycle current pulses of 200 ns duration and 100 kHz repetition rate. Inset shows lasing spectra for different bias where the spectral linewidth is limited by instrument's resolution. The emitted optical power is measured without any cone collecting optic inside the cryostat. (c) Measured spectra for four different antenna-feedback QCLs with varying grating periods Λ, but similar overall cavity dimensions. The QCLs are biased at a current-density $\sim$ 440 A/cm^2 at 78 K.

of ~ 0.45 mW (see section 2.6). The antenna-feedback gratings lead to greater radiative outcoupling compared to conventional DFB schemes for terahertz QCLs, as discussed in the previous section.

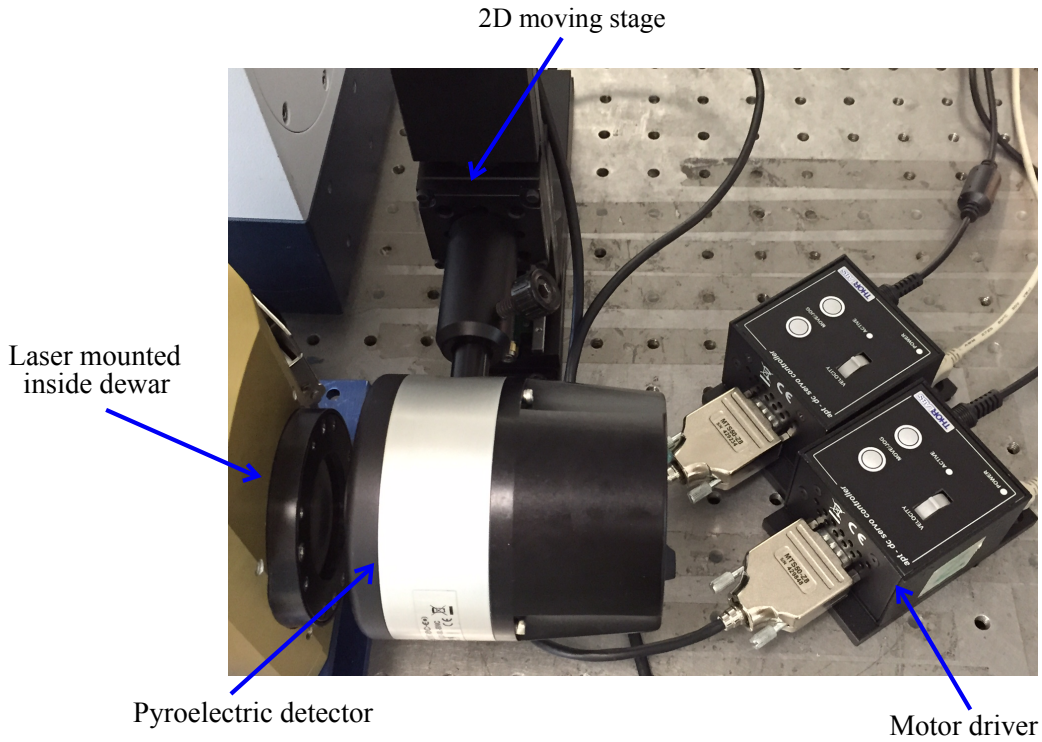

Figure 2.8: Experimental setup for beam measurement.

Fig. 2.7(c) shows spectra measured from four different terahertz QCLs with antenna-feedback gratings of different grating periods Λ. The single-mode spectra scales linearly with Λ, which is the clearest proof that the feedback mechanism works as expected and the lower band-edge mode is selectively excited in each case. Using $\lambda = \Lambda(n_a + 1)$ from equation (2.2), the effective propagation index of the SPP mode in the active medium n_a is calculated as 3.59, 3.53, 3.46, and 3.33 for QCLs with Λ of 21 μm, 22 μm, 23 μm, and 24 μm respectively. The effective mode-index n_a decreases because a larger Λ introduces larger sized apertures in the metal film since the grating duty-cycle was kept same for all devices. Consequently, a greater amount of field couples to the single-sided SPP mode in air for increasing Λ, thereby

reducing the modal confinement in the active medium that reduces the propagation index of the guided SPP mode further.

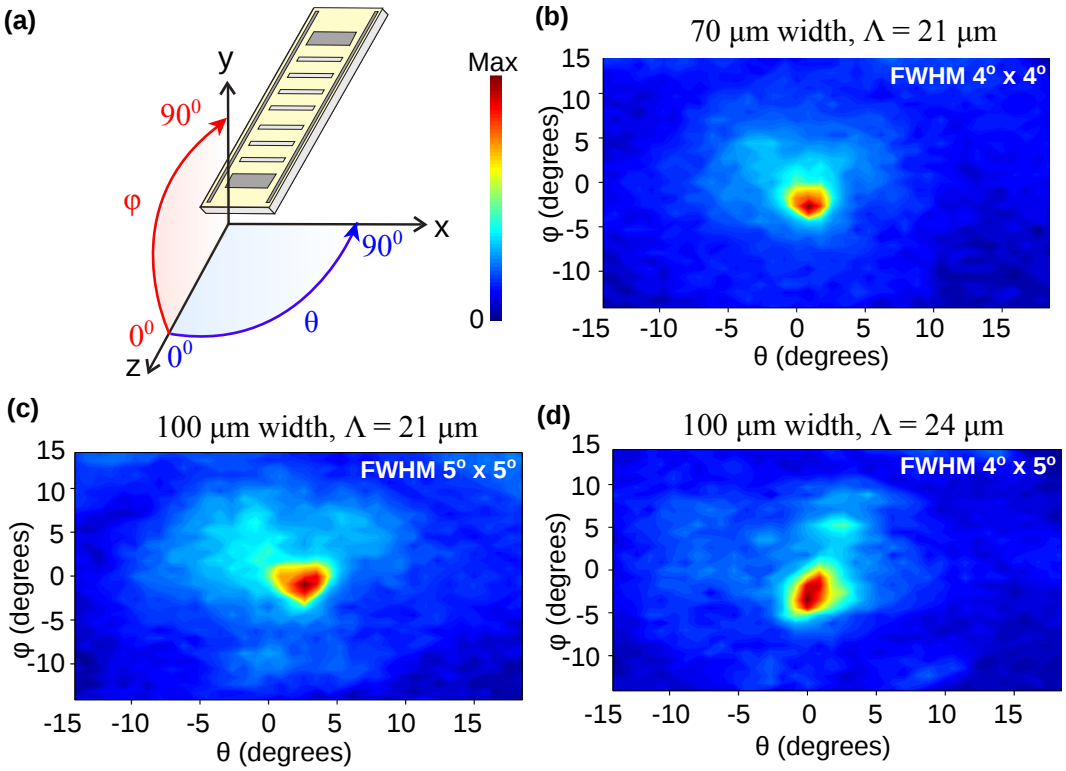

Figure 2.9: Far-field radiation-patterns of terahertz QCLs with antenna-feedback. (a) Schematic showing orientation of QCLs and definition of angles. The QCLs were operated at 78 K in pulsed mode and biased at $\sim$ 440 A/cm^2 while lasing in single-mode. The plots are for QCLs with $\sim$ 1.4 mm long cavities and (b) 70 μm width and $\Lambda = 21$ μm grating emitting at $\sim$ 3.1 THz, (c) 100 μm width and $\Lambda = 21$ μm grating emitting at $\sim$ 3.1 THz, and (d) 100 μm width and $\Lambda = 24$ μm grating emitting at $\sim$ 2.9 THz respectively.

Experimental far-field beam patterns for antenna-feedback QCLs with varying designed parameters are shown in Fig. 2.9. Single-lobed beams in both lateral (x) and vertical (y) directions were measured for all QCLs. As shown in Fig. 2.9(b), the full-width half-maximum (FWHM) for the QCL with 70 μm width, $\Lambda = 21$ μm is $\sim 4^\circ \times 4^\circ$, which is the narrowest reported beam-profile from any terahertz QCL to-date. In contrast, previous schemes for emission in a narrow-beam have resulted

in divergence angles of $6^\circ \times 11^\circ$ using very long (> 5 mm) cavities and a phased-matched third-order DFB scheme [48] and $7^\circ \times 10^\circ$ using broad-area devices with 2D photonic-crystals [52] for single-mode terahertz QCLs, and $4^\circ \times 10^\circ$ [58] and $12^\circ \times 16^\circ$ [59] for multi-mode QCLs using metamaterial collimators. Figs. 2.9(c) and 2.9(d) show representative beam patterns from QCLs with wider cavities of 100 μm width, for the smallest and largest Λ in the range of fabricated devices respectively. The beam divergence is relatively independent of Λ as expected. More importantly, the measurements show that the wider cavities result in a slightly broader beam. Such a result is counter-intuitive because typically a laser emits in a narrower beam as its cavity's dimensions are increased due to an increase in the size of emitting aperture. Such a behavior is unique for a spaser with antenna-feedback, and is discussed along with full-wave 3D FEM simulation of the beam pattern in section 3.1. It can be argued that the size of the beam could be further narrowed by utilizing narrower cavities for terahertz QCLs, which will be extremely beneficial to develop cw sources of narrow-beam coherent terahertz radiation.

In this thesis, all measurements are presented in pulsed mode operation. Continuous-wave (cw) operation was achieved for cavity width of both 100 μm and 70 μm at 50 K operated in Stirling cryocooler. Robust single mode spectrum was measured from antenna-feedback scheme. For example, for antenna-feedback scheme with 100 μm width and grating period 24 μm, wavelength of continuous-wave lasing is ~ 104 μm. In cw operation, we have not done the beam pattern measurements.

2.6 Experimental characteristics of third-order DFB QCL and a Fabry-Pérot-cavity QCL

Figure 2.10 shows *L-I* characteristics of a representative terahertz QCL with third-order DFB without well defined phase-matching condition that was fabricated on the same chip by standard lithography to pattern grating on top metallic layer, and with similar dimensions as that of the antenna-feedback QCLs whose data is reported in Fig. 2.7. Using the phase condition $\lambda = 2n_{\mathrm{a}}\Lambda/p$ as determined from

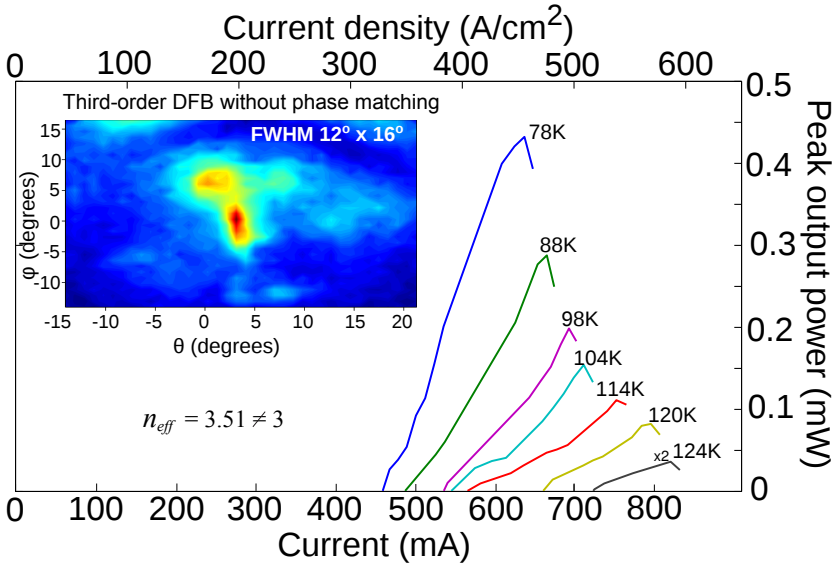

Figure 2.10: Lasing characteristics of a terahertz QCL with third-order DFB without phase matching. Light-current characteristics of a terahertz QCL with third-order DFB in pulsed operation. The QCL is fabricated on the same chip, and the cavity dimensions are similar to the QCLs with antenna-feedback. The inset shows the measured far-field radiation-pattern with the same angular definitions as in Fig. 2.9(a). The QCL emitted predominantly in single-mode at $\lambda = 103.0$ μm ($\nu = 2.91$ THz) with grating period 44 μm .

equation 2.1 for $p = 3$ (third-order DFB), an effective-mode index of $n_{\rm a} = 3.51$ is estimated for the resonant-cavity SPP mode in the active medium of the cavity. For ideal phase-matching, a mode-index value of 3.0 is required, hence the phased-matching condition is not satisfied for this QCL. Consequently, the measured FWHM of the far-field radiation pattern $\sim 12^\circ \times 16^\circ$ for this QCL is not as good as that for phased-matched third-order DFB QCLs with reduced effective mode index [48, 47, 26]. Elongated and multi-lobed beam pattern for third-order DFB when refractive index is close to 3.6 is observed in Ref. [47]. The peak output power for the third-order DFB QCL without phase matching is ~ 0.45 mW at 78 K, which is about three times less than that obtained for the antenna-feedback QCL with similar dimensions lasing at similar frequency. The output power slope efficiencies

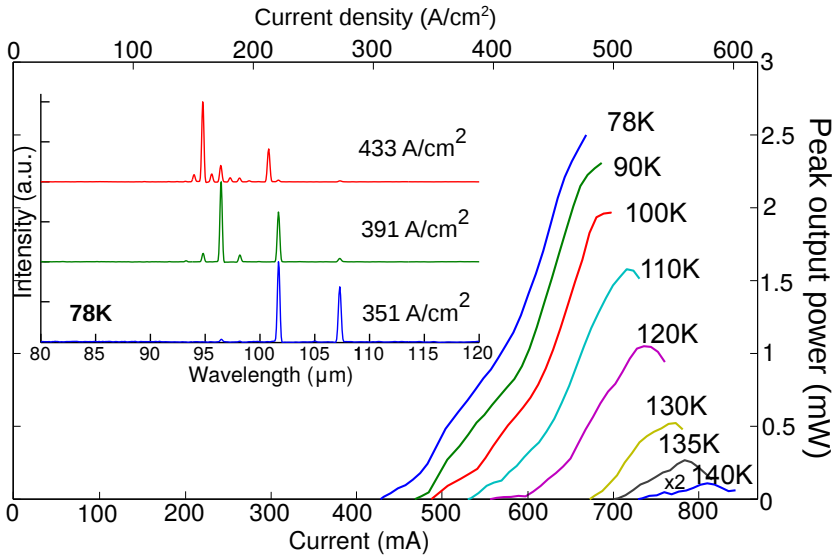

Figure 2.11: Lasing characteristics of a terahertz QCL with Fabry-Pérot cavity. Light-current characteristics of a QCL with Fabry-Pérot cavity at different heat-sink temperatures in pulsed operation. Output power was collected with a Winston cone placed close to laser facet due to the highly divergent beam pattern of Fabry-Pérot type THz QCLs. The inset shows lasing spectra at different bias at $\sim$ 78 K. .

at 78 K are 4 mW/A and 13 mW/A respectively for the third-order DFB QCL and antenna-feedback QCL respectively. The optical power was measured without cone collecting optics. The relative differences in the measured optical power are in good agreement with the radiative losses estimated via 2D FEM simulations for similar cavity dimensions as in Fig. 2.2. The maximum operating temperature of this QCL is almost similar to that of the antenna-feedback QCL, which suggests that radiative loss is a relatively small fraction of the overall waveguide loss in both types of DFB QCL cavities. This also suggests that there is a scope for enhancing the radiative efficiency to increase optical power output without causing a significant degradation in temperature performance of terahertz QCLs with antenna-feedback. Calculation of surface-outcoupling efficiency as in Ref. [60] is outside the scope of this work due to the large uncertainty in the absolute loss contribution of metal layers, absorbing

boundaries, as well as the active region itself. The optimized phase-matched third-order DFB [26] with bound-to-continuum design shows lower current-density and higher efficiency without absorbing regions. Since the feedback of the laser mode is achieved by SPP mode propagating on the surface for antenna-feedback, technique of covering waveguide sidewall with metal [25] or lateral corrugated grating [26], which does not absorb effective outcoupled laser radiation from antenna-feedback, can replace lateral absorber layer here and will further enhance the outcoupling efficiency. L-I characteristics at different heat-sink temperature of a representative terahertz QCL with Fabry-Pérot (FP) cavity is shown in Fig. 2.11. Exposed highly-doped lossy contact layer serving as absorber introduces $\sim$ 15 K temperature degradation for DFB cavity. Because sub-wavelength mode confinement in FP cavities results in highly divergent output beams of THz QCLs with parallel-plate metallic cavities, the output power is measured with a Winston cone and the detector was placed adjacent to the cryostat window. The diameter of the circular opening of cone is $\sim$ 1.9 mm. The frequency of gain medium covers $\sim$ 2.8 THz to $\sim$ 3.2 THz at $\sim$ 78 K.

2.7 Summary

In this chapter, we have presented a novel antenna-feedback scheme to achieve single-mode operation and a highly directional far-field radiation pattern from plasmonic lasers with subwavelength apertures and Fabry-Pérot type cavities. It is conceptually different from any other previously utilized DFB schemes for solid-state lasers, and is based on phase-locking of a single-sided surface-plasmon-polariton (SPP) mode on (one of) the metal film(s) in the spaser's cavity with the guided SPP mode inside the spaser's active medium. The phase-locking is established due to strong Bragg diffraction of the SPP modes by periodically perforating the metal film in the form of a grating of holes or slits. The uniqueness of the method lies in the specific value of the grating's period, which leads to the spaser's cavity radiating

like an end-fire phased-array antenna for the excited DFB mode. Additionally, coherent single-sided SPPs are also generated on the metal film that have a large spatial extent in the surrounding medium of the laser's cavity, which could have important implications for applications in integrated plasmonics. Coherent SPPs with large spatial extent could make it easy to couple SPP waves from the plasmonic lasers to other photonic components, and could also potentially be utilized for plasmonic sensing. Experimentally, the scheme is implemented in terahertz QCLs with subwavelength metallic cavities. A beam-divergence angle as small as $4^\circ \times 4^\circ$ is achieved for single-mode QCLs, which is narrower than that achieved with any other previously reported schemes for terahertz QCLs with periodic photonic structures. Compared with the third-order DFB method, the new antenna-feedback scheme is easier to implement for fabrication by standard lithography techniques without any other complex fabrication technique to precisely match a well defined effective mode index, and achieves a superior radiative outcoupling owing to the fact that the grating period is not an integer multiple of half-wavelengths of the standing SPP-wave inside the active medium. Terahertz QCLs with antenna-feedback could lead to the development of new modalities for terahertz spectroscopic sensing and wavelength tunability due to access of a coherent terahertz SPP wave on top of the QCL's cavity, possibilities of sensing and imaging at standoff distances of few tens of meters, and development of integrated terahertz laser arrays with a broad spectral coverage for applications in terahertz absorption spectroscopy.

Chapter 3

Analysis and design of terahertz quantum cascade lasers with new antenna-feedback scheme

This chapter presents a comprehensive design and analysis for the novel antenna-feedback scheme, which achieves a highly directional far-field radiation pattern from plasmonic lasers with subwavelength apertures and Fabry-Pérot type cavities. The antenna-feedback scheme is compared with conventional DFBs on various aspects, such as characteristics of electric field distribution, SPP mode on top of subwavelength metallic cavity and energy density profile along the whole length of laser cavity. Antenna-feedback scheme strongly couples the surface-plasmon-polariton (SPP) mode on the metal layer with the guided SPP mode inside the active medium. Role of the longitudinal absorbing boundaries is discussed. Antenna feedback with different absorber lengths, duty cycles and lengths are discussed as well. Third-order DFB with and without phase-matching condition is presented. Calculated beam pattern from 3D simulations and geometry used in 3D simulations are shown. Beam pattern multiplication theory of a phased-array antenna model is introduced to analyse the narrow beam output of antenna-feedback scheme. In addition, new photonic structures are proposed for antenna-feedback scheme to further improve

output power $\sim$ 3 THz and robustly operate at lower frequency $\sim$ 2 THz.

3.1 Analysis of antenna-feedback scheme

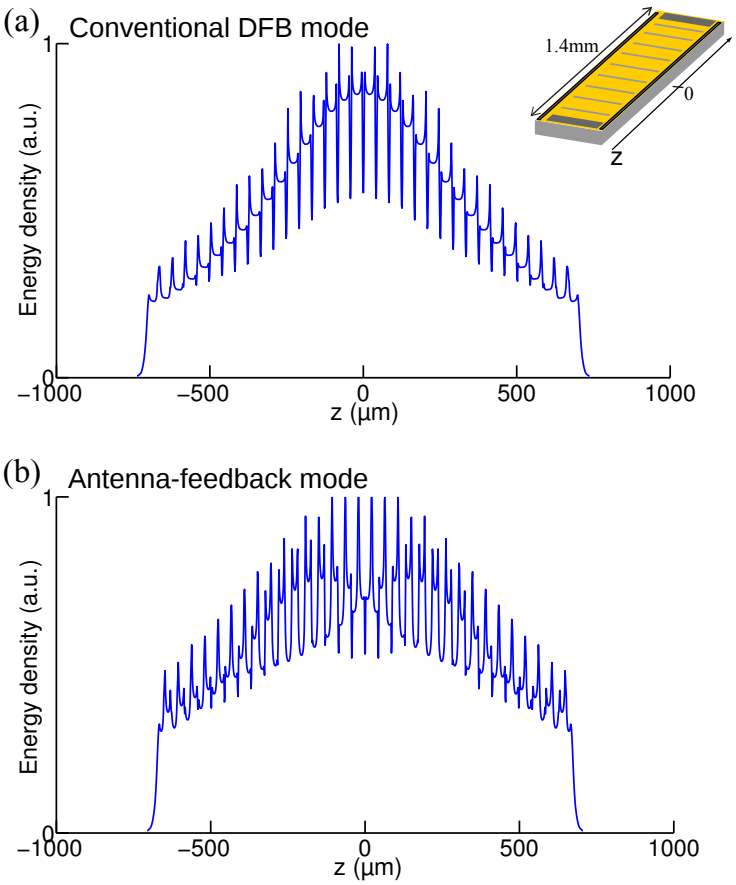

Figure 3.1: Energy-density profiles along the length of the metallic cavities (in z direction) for the band-edge DFB modes for (a) third-order DFB cavity, and (b) cavity with antenna-feedback respectively.

Figure 3.1 shows energy-density profile for the resonant band-edge modes of the cavities with third-order DFB and antenna-feedback schemes respectively, along the entire length of the cavity ($\sim$ 1.4 mm). Energy-density is calculated and summed up along the cavity's height (10 μm) from 2D simulations (that effectively model cavities

of infinite width). The eigenmode spectra and electric-field distributions for the cavities are shown in Fig. 2.2. Both third-order DFB and antenna-feedback schemes show non-uniform envelope shapes, which gradually decrease from the center to the end-facets of cavity and provide indication of typical DFB action due to coupling of propagating waves along the length of cavity as per the corresponding schematics in Fig. 2.1.

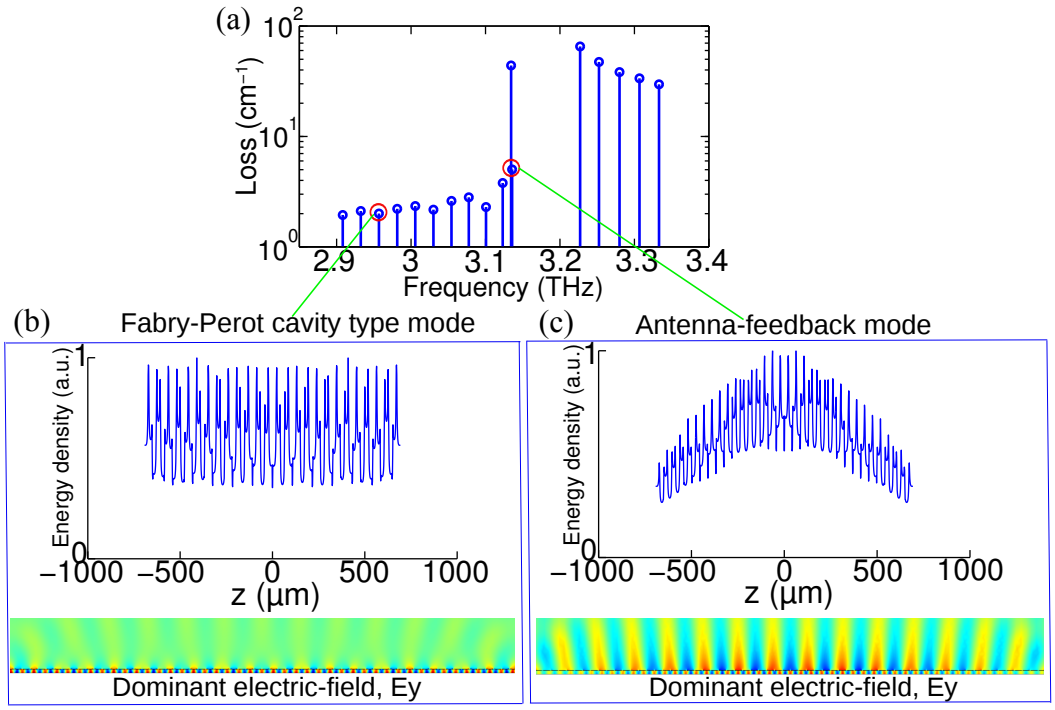

Figure 3.2: Role of longitudinal absorbing boundaries in resonant-cavities with antenna-feedback. (a) Eigenmode spectrum of QCL metallic cavity with antenna-feedback gratings in the top metallic layer, but without longitudinal absorbing boundaries at the two ends of the cavity. The dimensions of the cavity are otherwise similar to that for the result in Fig. 2.2(b). (b) Energy density profile along the length of the ~ 1.4 mm long cavity and dominant electric field E_y of a Fabry-Pérot cavity type mode that exists sufficiently away from the photonic bandgap. (c) Energy density profile and electric-field profile along the length of the cavity for the "desired" antenna-feedback mode that exists at the edge of the photonic bandgap. The z direction is along the length of laser ridge, as marked in Fig. 3.1.

A thin highly-doped GaAs layer below the top-metal cladding was left unetched at the regions close to longitudinal facets, serving as the longitudinal absorbing boundary to ensure the excitation of the desired antenna-feedback mode as the lowest-loss lasing mode. Firstly, such absorbing boundaries reduce the end-facet reflectivities that strengthens the distributed-feedback coupling for the antenna-feedback scheme. Secondly, the longitudinal absorber boundaries play an important role in providing the necessary mechanism for mode-discrimination, to selectively excite the desired band-edge antenna-feedback mode for lasing. Figure 3.2(a) shows the eigenmode spectrum of the antenna-feedback scheme without longitudinal absorbing boundaries. There exist the Fabry-Perot type modes with uniform energy density profile along the whole length of laser cavity and large electric field distribution close to end facets of the cavity, as shown in Fig. 3.2(b). However, the loss of such modes is small due to highly reflective end-facets. The desired antenna-feedback mode, located at the lower bandedge, shows non-uniform energy-density profile along the length of cavities as an indicator of DFB action and strong coupling between plasmonic mode on top of metallic layer and guided mode in the active core, as seen from Fig. 3.2(c). However, its radiative loss is higher due to the improved and large radiative field of antenna-feedback mode and hence, it cannot be excited for lasing in the absence of longitudinal absorbing boundaries. When longitudinal absorbing boundaries are introduced, the relative loss of the modes with large intensity closer to longitudinal ends of cavity, which are further away from the photonic bandgap, will be selectively and significantly increased. Therefore, the antenna-feedback mode is excited for lasing as the robust lowest-loss mode as seen from the eigenmode spectrum in Fig. 2.2(b).

In 2D simulations, a loss of ~ 5 cm^{-1} was estimated as a contribution from the absorbing boundaries. Third-order DFB with and without absorbing boundaries are compared, the loss difference is ~ 5 cm^{-1} and the energy density plot keeps the same non-uniformity. Therefore, ~ 5 cm^{-1} can be roughly represents the loss introduced by the absorbing boundaries.

Figure 3.3 shows lateral mode shape of the antenna-feedback mode at approximately the longitudinal center of the cavity from 3D simulation. The SPP mode

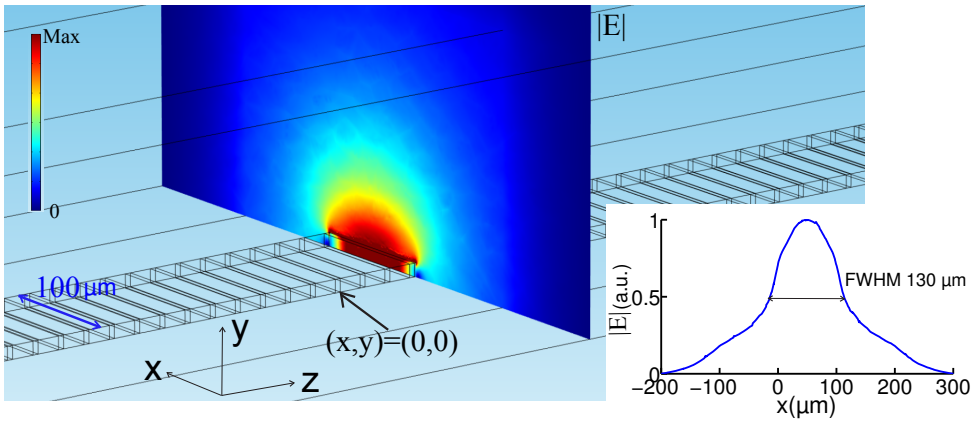

Figure 3.3: Electric-field profile of the SPP mode in surrounding medium of the plasmonic laser's cavity with antenna-feedback gratings from 3D simulation. A parallel-plate metal cavity with GaAs medium of 100 μm width, 10 μm thickness, and 1.4 mm length is simulated. The frequency of the band-edge resonant-cavity mode is $\sim$ 3.15 THz, which is the desired "antenna-feedback" mode. Inset: Mode shape along lateral x dimension of cavity at a distance of 10 μm above the top metal cladding; the FWHM of the lateral electric-field profile is $\sim$ 130 μm.

in surrounding medium extends in both lateral and vertical directions significantly, and the extent of the mode in lateral (x) dimension is greater than the width of the cavity itself. The FHWM of the mode shape along the lateral (x) dimension of the cavity at a distance of $\sim$ 10 μm above top gratings (picked arbitrarily to keep it slightly away from location where finite-element mesh in simulation changes abruptly) is $\sim$ 130 μm. This large effective wavefront created on top of the waveguide leads to a narrow far-field, i.e. a narrow "element-factor" in the terminology of the radiation from a phased-array antenna. While the narrowing of "array-factor" due to constructive interference of radiation from all apertures in end-fire direction is also at play; it is not the dominant effect to cause narrow beaming for terahertz QCLs in this work for short-length cavities ($<$ 2 mm). In contrast, for third-order DFB QCLs with phase-matching, beam narrowing is primarily due to the narrow array-factor only, which is why very long cavities ($<$ 5 mm) are needed to achieve

beam divergence values of less than $\sim 10^{\circ}$ [48].

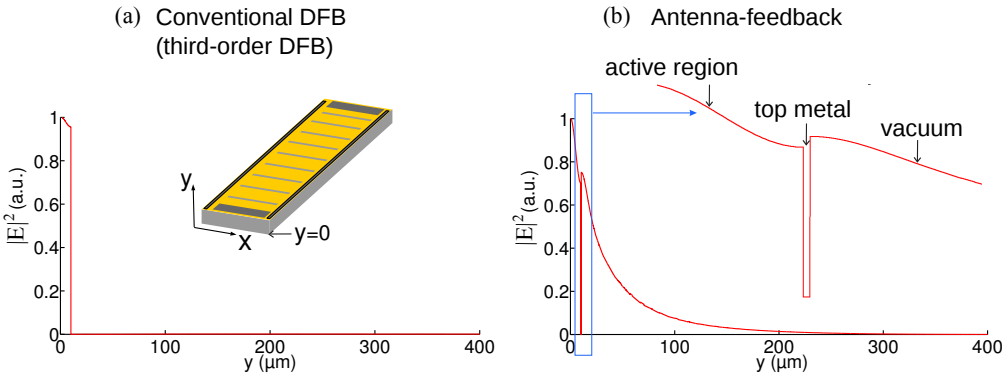

Figure 3.4: Comparison of electric-field squared modulus $|E|^2$ profile in conventional DFB (third-order DFB as an example) and antenna-feedback scheme. (a) $|E|^2$ profile for third-order DFB cavity plotted along perpendicular y direction (cavity's height direction). (b) $|E|^2$ profile for antenna-feedback scheme with an expanded view close to top metal cladding.

Figure 3.4 shows the electric-field squared modulus $|E|^2$ profile inside the cavity and above the metal cladding for both conventional DFB and antenna-feedback scheme from 2D simulations. Layer sequence follows active region with 10 μm thickness, top metal layer with 400 nm thickness (lossless metal) and air region. At the location above metal cladding, the mode-intensity in conventional DFB immediately decays to zero. In contrast, for antenna-feedback scheme, the sub-wavelength plasmonic resonant-optical mode inside the cavity is phased-locked with a SPP mode that travels on top of the metal cladding outside the cavity. The SPP wave is relatively tightly bound to the top metal cladding and decays in the length of the order of the wavelength in vacuum. The decay length is independent of the loss in metal or thickness in metal or various duty cycles of grating (which was verified via finite-element simulations). The establishment of a hybrid SPP mode on top of the cavity in vacuum is unique in antenna-feedback scheme. In a third-order DFB terahertz QCL, even with effective mode index getting close to 3.0, the feedback mechanism remains same as that in conventional DFB lasers, i.e. distributed-feedback couples

propagating modes inside the cavity without involving the propagating SPP waves in the surrounding medium. Correspondingly, no standing SPP wave (with large amplitude) is established in the surrounding medium in a third-order DFB QCL's cavity as it does in antenna-feedback scheme. This could be verified by simulating a terahertz QCL cavity structure with third-order DFB gratings, but with the refractive index of the active region arbitrarily set to a value of ~ 3.0 to satisfy the so-called "phase-matching" condition in simulation.

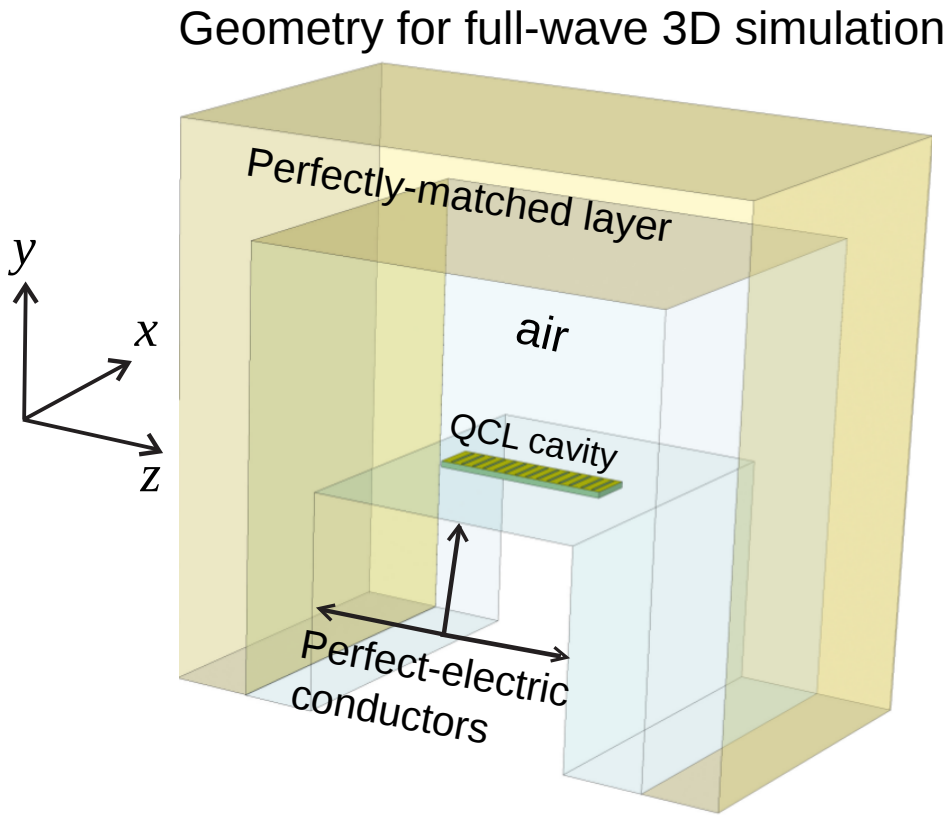

Figure 3.5: Geometry of full-wave 3D simulation The modeled geometry for full-wave 3D simulation with the FEM solver [2]. Parallel-plate metallic terahertz QCL cavities of 1.4 mm length, 10 μm thickness, varying widths, and a grating period of $\Lambda = 21.7$ μm were implemented, which excite antenna-feedback resonant-cavity modes at $\nu \sim 3.1$ THz.

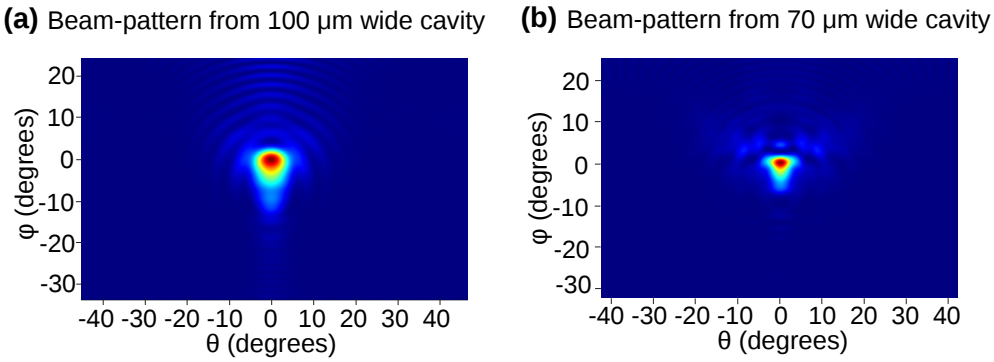

Figure 3.6: Full-wave 3D simulation to compute far-field radiation pattern of QCL cavities with antenna-feedback. (a) Simulated far-field radiation pattern of the cavity with 100 μm width. The FWHM is $\sim 7^\circ \times 7^\circ$. (b) Far-field radiation pattern of the cavity with 70 μm width. The FWHM is $\sim 6^\circ \times 5^\circ$.

The confinement factor Γ is defined as the fraction of the mode that is inside the active-medium. The following equation is used to compute the confinement factor of antenna-feedback scheme for THz QCLs.

$$ConfinementFactor = \frac{\int 12.9|E_y|^2_{wg}}{\int 12.9|E|^2_{wg} + \int |E|^2_{air}} \tag{3.1}$$

For THz QCLs, according to the intersubband selection rule, only transitions with the E field polarized along the growth axis are permitted. Therefore, only TM polarized field (E_y) contributes to gain. For antenna-feedback with similar dimension as shown in Fig. 2.2, typical calculated confinement factor from 2D simulations is ~ 70 %. Active region with 10 μm thickness and air domain above the cavity are utilized as the domains in the surface integration of calculation.

The narrow-beam emission from plasmonic lasers with antenna-feedback is due to a combination of two factors that are related to the radiative behavior of phased-array antennas. In addition to the *array-factor* that leads to narrower beams for more number of elements in a phased-array (i. e. in this case, a longer length of the spaser's cavity), the far-field radiation pattern is additionally narrowed owing to an *element-factor*, which is defined as the far-field radiation pattern due to an

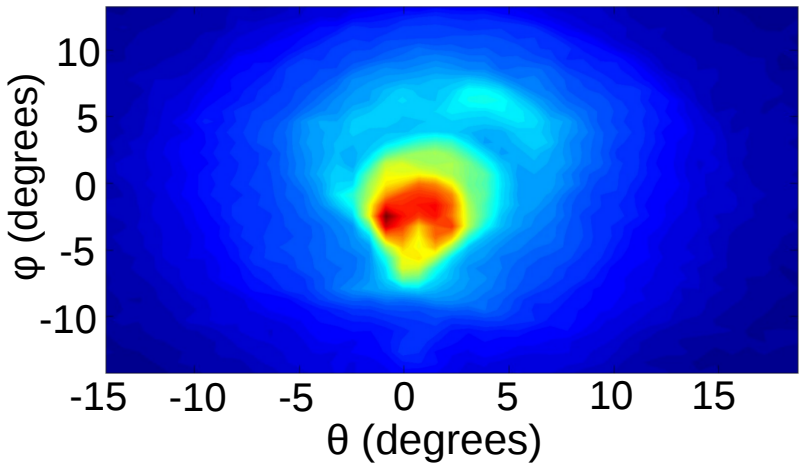

Figure 3.7: Measured beam pattern of antenna-feedback with 70 μm with Stirling cyrocooler at 50 K .

individual emitter of the phased-array [61]. The large spatial extent of the single-sided SPP wave in the surrounding medium results in a narrower element-factor compared to an omnidirectional point-source emitter.

As measured experimentally and shown in Fig. 2.9, the antenna-feedback terahertz QCL cavities with a narrower width of 70 μm resulted in a beam with smaller divergence as compared to the 100 μm wide cavity. This seemingly unique behavior from antenna-feedback QCLs serves to further validate the concept of the specific feedback scheme, in which the cavity radiates like a phased-array antenna. A narrower cavity causes greater lateral spread of the single-sided SPP mode (in the x dimension) in the surrounding medium, especially when the cavity's width is sub-wavelength. A single-sided SPP mode with a broader cross-section in the $x-y$ plane will lead to a more directional far-field radiation pattern owing to a narrower element-factor for the phased-array antenna structure.

To further validate the experimental results of Fig. 2.9, full-wave 3D FEM simulations were carried out for terahertz QCL cavities with antenna-feedback. Figure 3.6 shows the computed far-field radiation patterns for band-edge DFB mode for terahertz QCL cavities implemented with antenna-feedback gratings in the top metal cladding. The in-built perfectly-matched layers (PMLs) in the FEM solver [2]

serve as an effective absorbing boundary for computation of the radiation pattern. The PMLs' parameters are coarsely adjusted to achieve minimum reflection at terahertz frequencies and transform the propagating waves to exponentially decaying waves. The PMLs are placed far enough to avoid interaction with the single-side SPP standing-wave in the near-field of the cavity. Considering the computer's memory limitations, laterally absorbing boundaries are not modeled in the cavity, which does not impact the simulation's results since the DFB mode could always be found, even though it is not the lowest loss mode in the eigenmode spectrum of the cavity due to other higher order lateral modes that can have even lower propagation loss. All metal layers are modeled as perfectly conducting surfaces to limit the mesh size in the geometry. In order to set up a far-field calculation, a far-field domain node is implemented that is a single closed surface surrounding all radiating apertures in the cavity. The distribution of far EM field is based on the Fourier transform of the near-field as implemented in the FEM solver. Simulated 3D beam patterns demonstrate single-lobed beams with narrow divergence for the band-edge mode with antenna-feedback as shown in the figure. The shape and FWHM of the computed radiation-pattern is in close agreement with the experimentally measured beams that are shown in Fig. 2.9. The FWHM of simulated beam patterns is slightly larger than that of the measured results. The difference are likely due to the relative simplification of implemented 3D model, which does not account for the sloped sidewall profile of the ridges and also the fact the ground plane around the QCL's cavity is different for the measured chip as compared to that in the simulated geometry.

Fig.2.9 in Chapter 2 shows the far-field radiation-patterns of terahertz QCLs with antenna- feedback at 78 K, the laser is mounted in a liquid nitrogen cooled dewar. Figure 3.7 shows the measured beam pattern of antenna-feedback with 70 μm, grating period 21 μm with Stirling cyrocooler at 50 K with TPX window of chamber. FWHM of measured beam pattern is $\sim 6^\circ \times 7^\circ$, slightly broader beam is likely due to the vibration of chamber introduced by the Stirling cryocooler. The device is biased at 416 mA.

The antenna-feedback scheme allows the metal-cavity semiconductor laser to

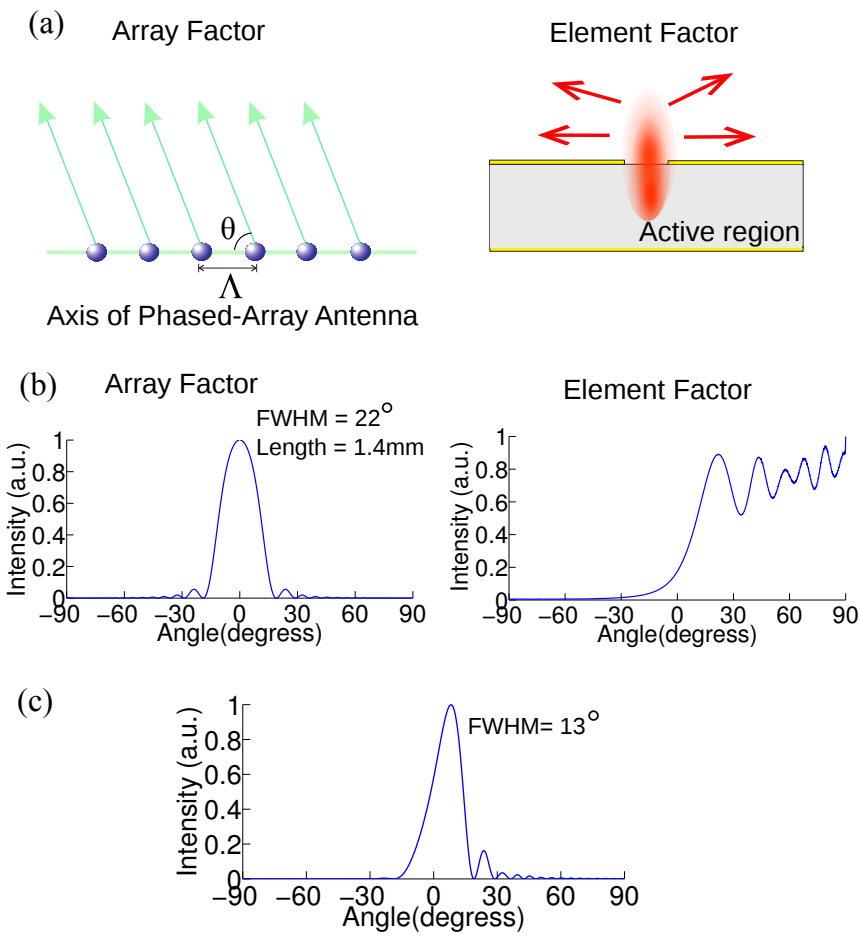

Figure 3.8: Beam pattern multiplication of a phased-array antenna model. (a) Schematic of one-dimensional linear phased-array antenna model and a single radiative element. (b) Calculated array factor and simulated far field beam pattern from an array element. (c) Multiplication of array factor and element factor results in the far field beam pattern of phased-array antenna.

emit with high directionality along the end-fire direction, much like phased-array antennas commonly used in radio or microwave frequency. Phased-array antenna consists of an assembly of single emitters. Array factor is a function of the geometry of the array and the excitation phase relation between individual elements. Element factor is the radiative pattern of individual elements. According to the beam pattern

multiplication theorem of phased-array antenna, the array pattern is the multiplication of array factor and array element pattern (element factor). This approach can be effectively applied to beam pattern calculation of the antenna-feedback scheme to give a deeper understanding of emission characteristics. Since the light out coupled from antenna-feedback laser is along the cavity length direction, it corresponds to the concept of end-fire array in microwave, which directs the radiation along the axis of the array (end-fire direction). The grating period in antenna-feedback represents the distance between each element along the axis of end-fire array, as shown in Figure 3.8(a), which determines the progressive phase between each succeeding element. Element factor is treated as a single emitting aperture calculated from 2D simulation. Antenna-feedback scheme is engineered that it can effectively provide feedback for the mode inside and outside the cavity and the grating period is especially designed to couple the laser light out of cavity and direct it into free space along the axis of the array simultaneously, because only in this end-fire direction can the field add in phase, while destructive addition happens in other directions, as can be seen from the calculated array factor in Figure 3.8(b), which has a single peak at zero degree (or 180 degree), corresponding to end-fire direction. full-width half-maximum (FWHM) of the array factor is $\sim 22^\circ$ calculated with total length ~ 1.4 mm from a simple point source model. Beam pattern is able to be studied analytically for the one-dimensional linear array, by multiplying the array factor and beam pattern radiation characteristic of each element. The FWHM of beam pattern after multiplication is $\sim 13^\circ$, as shown in Figure 3.8(c), as a result of this simplified analytical element factor and antenna model with identical emitting elements without considering any DFB action.

Eigenmode spectrum for total length of cavity ~ 1.4 mm for antenna-feedback scheme with ~ 10 μm long longitudinal absorbing boundaries is shown in Fig. 3.9(a) as compared with Fig. 2.2(b), where ~ 40 μm long longitudinal absorbing boundaries are utilized. The desired antenna-feedback mode, located at the lower bandedge with lowest loss, is excited and shows non-uniform electric field distribution along the length of cavities as an indicator of DFB action as seen from Fig. 3.9(a)(b). Fig. 3.9(c)(d) shows the dominant E_y electric-field magnified, in which there is

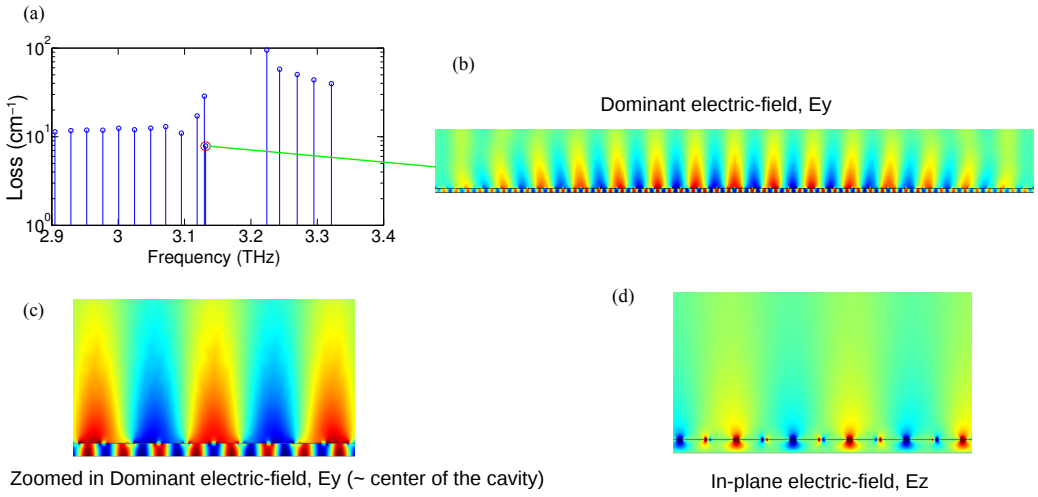

Figure 3.9: Antenna-feedback scheme with $\sim$ 10 μm long longitudinal absorbing boundaries. (a) Eigenmode spectrum for total length of cavity $\sim$ 1.4 mm. (b) Dominant TM polarized (E_y) electric-field along the whole length of cavity. (c) Zoomed in dominant E_y electric-field around the longitudinal center of cavity. (d) Zoomed in dominant E_z electric-field around the longitudinal center of cavity.

strong coupling between the SPP mode on top of metallic layer and the guided mode in the active core, and in-plane E_z electric-field around the longitudinal center of cavity (large radiative field in alternating apertures), respectively. Fig. 3.9 suggests that the antenna-feedback mode can be excited for lasing as the robust lowest-loss mode even with shorter length of longitudinal absorbing boundary, which will be beneficial to reduce overall waveguide loss of laser cavity.

Antenna-feedback scheme with duty cycle of 80% (namely a periodic grating with apertures of width 0.20Λ in the top-metal cladding) are implemented for DFB, the results are shown in Fig.2.2 (b). A comparison is shown in Fig. 3.10 with different duty cycle 75% (width of apertures is 0.25Λ). The total loss and the radiative loss of the desired lowest loss antenna-feedback mode increased to $\sim$ 11.6 cm^{-1} and $\sim$ 6.6 cm^{-1}, respectively. Confinement factor reduces to 67%. The unique characteristics of antenna-feedback mode maintains as can be seen from the electric field distributions and the energy density profile. Therefore, larger aperture size of antenna-feedback scheme can be used to increase the output power. However,

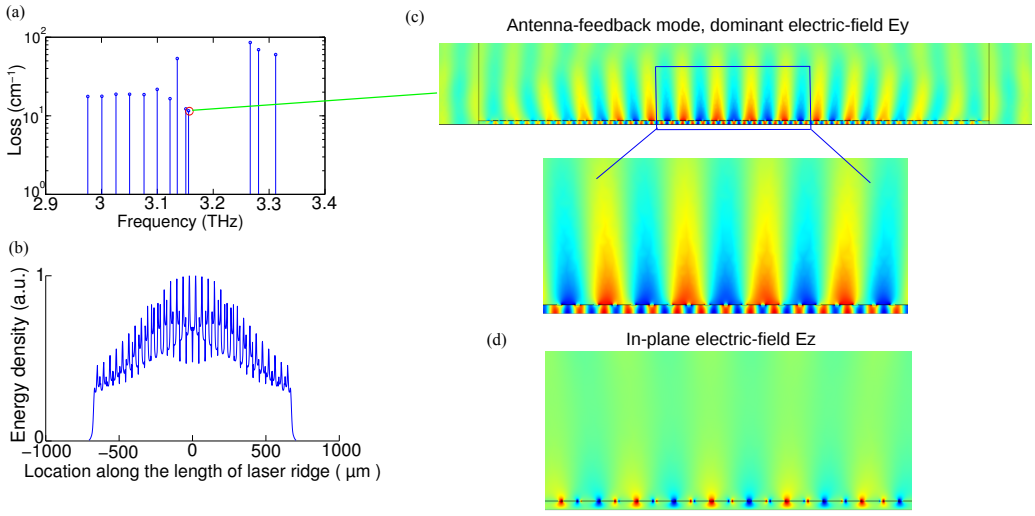

Figure 3.10: Antenna-feedback cavity for THz QCLs with duty cycle of 75% .

uniform current flow in top metallic layer has to be considered in real laser device since top metal layer is also utilized to transport the current of the laser device for terahertz QCLs with metal-metal waveguide. 2D simulation of antenna-feedback cavity for THz QCLs with total length $\sim$ 2 mm is shown in Fig. 3.11. Longer cavity introduces more non-uniform energy density profile along the length of cavity for antenna-feedback.

The establishment of a SPP mode on top of the cavity in vacuum is unique in antenna-feedback scheme. In a third-order DFB terahertz QCL, even with effective mode index getting close to 3.0, the feedback mechanism remains the same as in conventional DFB lasers, i.e. distributed-feedback couples propagating modes inside the cavity without involving the propagating SPP waves in the surrounding medium. Correspondingly, no standing SPP wave (with large amplitude) is established in the surrounding medium in a third-order DFB QCL's cavity as it does in antenna-feedback scheme. This could be verified by simulating a terahertz QCL cavity structure with third-order DFB gratings, but with the refractive index of the active region arbitrarily set to a value of $\sim$ 3.0 to satisfy the phase-matching condition in simulations, as shown in Fig. 3.12 from 2D simulations and Fig. 3.13 from 3D simulations, where both bottom view and side view of the electric field distributions

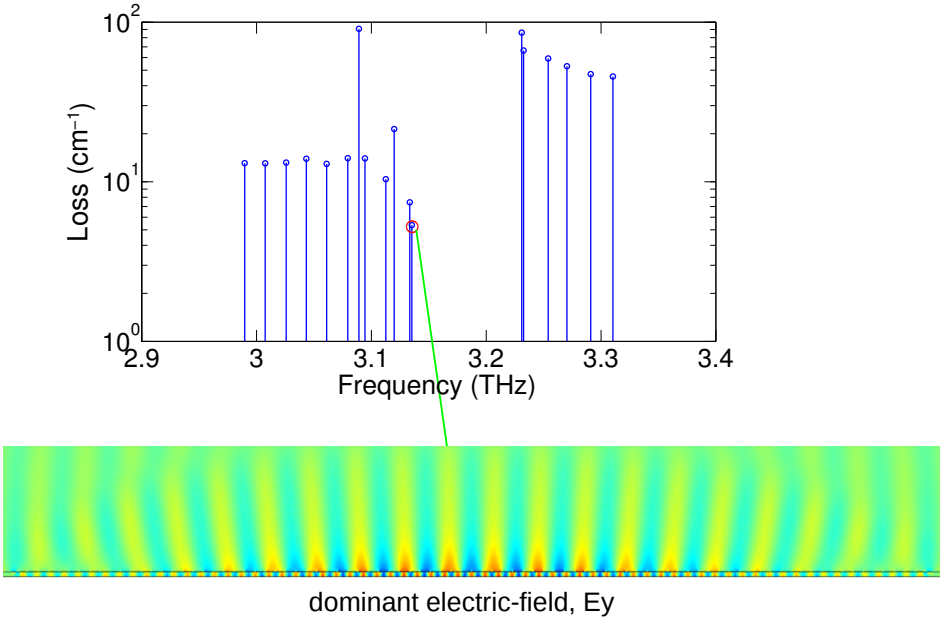

Figure 3.11: Antenna-feedback cavity for THz QCLs with total length ~ 2 mm .

are presented.

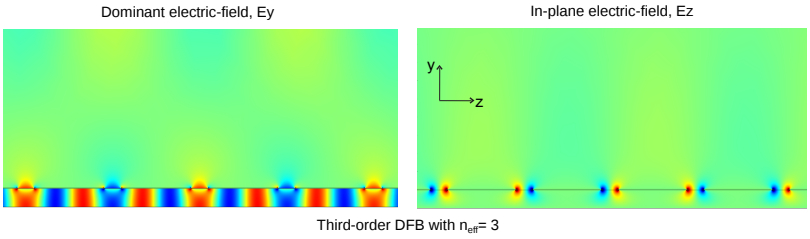

Figure 3.12: Electric-field distribution for third-order DFB with effective mode index ~ 3.0 from 2D simulations. (a) Dominant TM polarized (E_y) field, (b) In-plane (E_z) field around the longitudinal center of cavity.

Fig. 3.14 shows the computed far-field radiation pattern from 3D simulations of THz QCLs with third-order DFB cavity with effective mode index ~ 3.6 and ~ 3.0 , respectively. When effective mode index is ~ 3.6 , the phase-matching

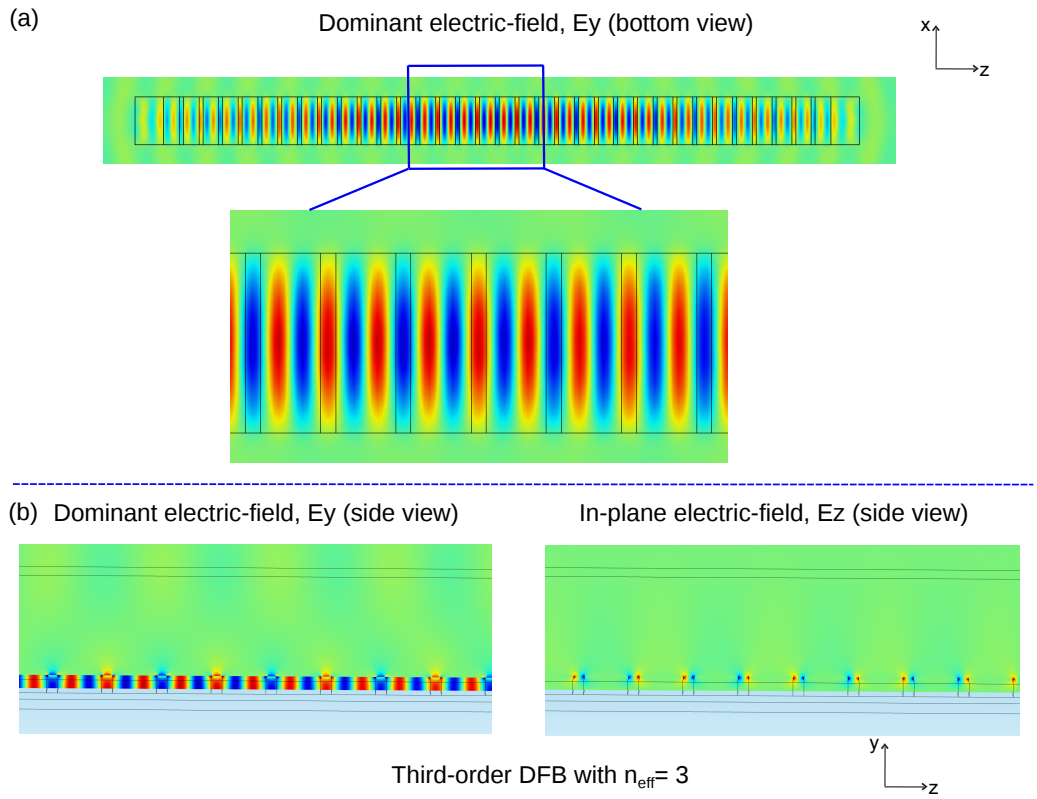

Figure 3.13: Electric-field distribution for third-order DFB with effective mode index ~ 3.0 from 3D simulations. (a) Dominant TM polarized (E_y) field from bottom view, (b) Dominant (E_y) field and in-plane (E_z) field around the longitudinal center of cavity from side view.

condition could not be satisfied, which leads to a divergent and multi-lobed beam. As long as effective mode index gets closer to ~ 3.0 , far-field radiation pattern gets collimated gradually and demonstrates ring shape with FWHM is $\sim 24^\circ \times 14^\circ$, in good agreement with the measured beam pattern in Ref. [26].

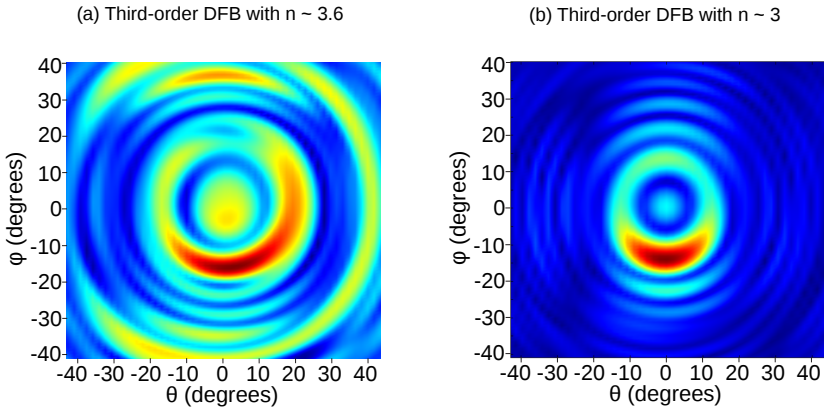

Figure 3.14: Computed far-field radiation pattern of THz QCLs with third-order DFB cavity. (a) Effective mode index ~ 3.6 . (b) Effective mode index ~ 3.0 .

3.2 Photonic engineering of antenna-feedback scheme

The low-frequency THz spectral region, specifically $\sim 1-2$ THz, will find important applications in the general areas of defense and security. This spectral region provides some low-loss atmospheric transmission windows in which THz sensing and detection is possible for short-range standoff distances. Also materials such as clothing, ceramics, and plastics are semi-transparent at low-THz frequencies while the wavelength is shorter than microwaves to allow good spatial resolution with small aperture devices, for potential development of hand-held sensing/imaging systems. Recently, there were demonstrations of THz QCLs based on a scattering-assisted (SA) injection design technique at low-frequency around or below 2 THz, such as ~ 2.1 THz QCLs that lased up ~ 144 K [63].

For antenna-feedback scheme at lower frequency ~ 2 THz, the frequency difference between the antenna-feedback mode and the upper band first-order DFB type mode is smaller due to the increased grating period. Fig. 3.15(a) shows the eigenmode spectrum for a cavity of total length ~ 1.4 mm with antenna-feedback scheme

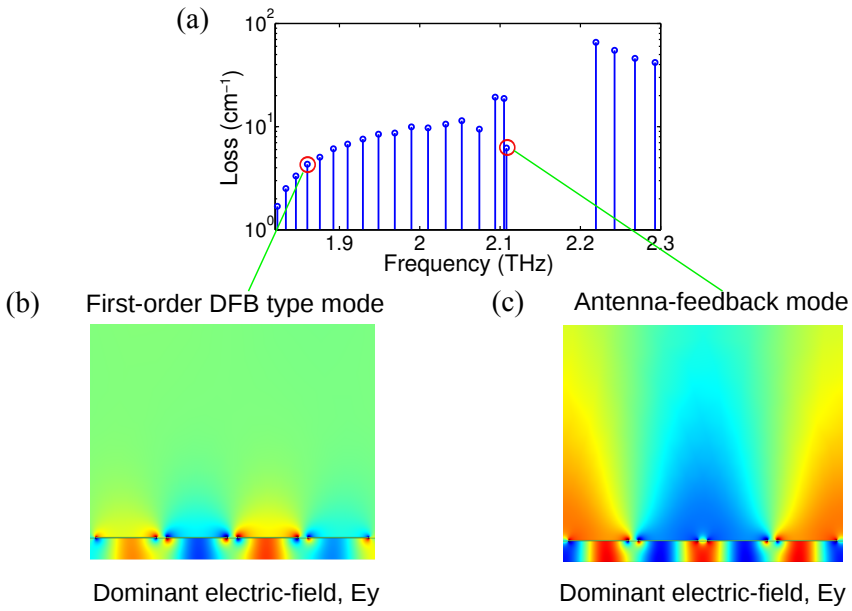

Figure 3.15: Structure 0 (one aperture for each grating period) for antenna-feedback ~ 2 THz (schematic shown in Fig. 2.1(d)). (a) Eigenmode spectrum for cavity of total length ~ 1.4 mm. (b) Zoomed in dominant TM polarized (E_y) electric-field around the center of cavity for first-order DFB type mode with lower loss at lower frequency. (d) Zoomed in dominant TM polarized (E_y) electric-field around the center of cavity for antenna-feedback mode.

$\sim$ 2 THz with schematic shown in Fig. 2.1(d), namely one grating aperture per grating period. There exist first-order DFB type modes at the lower frequency with lower loss as shown Fig. 3.15(b) . Antenna-feedback mode at the bandedge shows higher loss due to its enhanced radiative characteristics compared with conventional DFB modes as discussed in section 2. Thus, within the typical bandwidth of gain medium of THz QCLs, desired antenna feedback mode will be prevented from lasing with lower frequency $\sim$ 2 THz design of active medium since the first-order DFB type mode will reach threshold firstly.

A new photonic structure is proposed to excite antenna-feedback mode with narrow beam pattern and increased radiative efficiency as shown in Fig. 3.16(b).

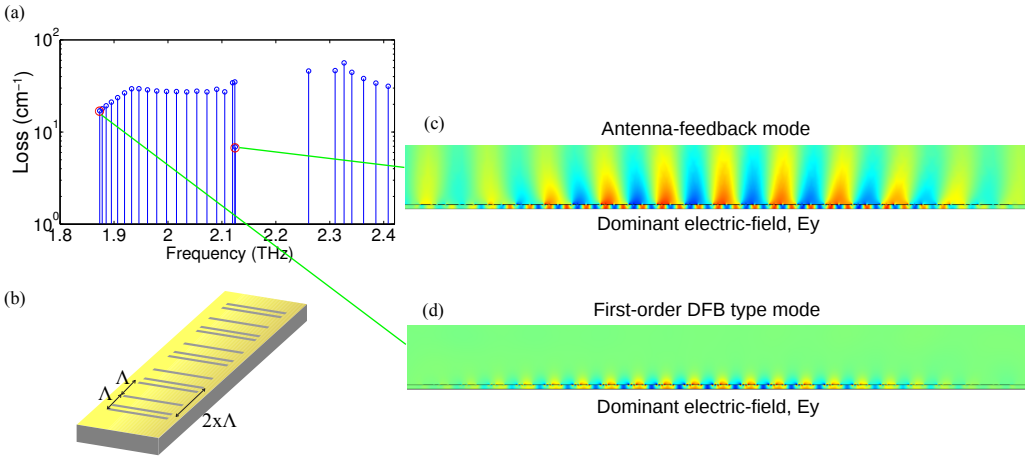

Figure 3.16: Structure 1 (an extra aperture is implemented for one grating period of each two grating periods) to implement antenna-feedback scheme at $\sim$ 2 THz . (a) Eigenmode spectrum for total length of cavity $\sim$ 1.4 mm. (b) Schematic of new structure 1 to implement antenna feedback at lower frequency $\sim$ 2 THz. (c) Dominant TM polarized (E_y) electric-field along the whole length of cavity for antenna-feedback mode as the lowest loss mode. (d) Dominant TM polarized (E_y) electric-field along the whole length of cavity for first-order DFB type mode with higher overall loss.

Based on the unique design on the grating period of antenna-feedback scheme, an extra aperture is implemented for alternating grating periods. The length of metal strip between original and adding aperture (spacing between two closely spaced slits) is $\sim 0.2\Lambda$, where Λ is the grating period of antenna-feedback scheme. This spacing between the two slits is able to serve as the parameter to control the radiative losses to enhance output power. The distance between each pair of adding apertures is 2Λ, as marked in Fig. 3.16(b). For antenna-feedback mode, 2Λ corresponds to the second-order diffraction grating of antenna-feedback mode, therefore, antenna-feedback mode with its unique characteristics can be maintained, as shown in Fig. 3.16(c). For the upper-band first-order DFB type mode, 2Λ corresponds to the resonant mode at the frequency around upper-band second-order DFB mode, which is the high outcoupling loss mode. As a result, this new method shown in

Fig. 3.16 can effectively and selectively increase the loss of the first-order DFB type mode while exciting the desired antenna-feedback mode as the robust lowest loss mode ~ 2 THz.

To further improve output power from antenna-feedback scheme at ~ 3 THz, we propose so-called structure 2 based on antenna-feedback scheme. As shown in the schematic in Fig. 3.17(b), one more aperture is implemented for each of grating period, forming a double-slit per period structure. The length of metal strip between original and adding aperture is $\sim 0.15\Lambda$. The distance between each pair of adding apertures is also fixed with Λ, so that the desired antenna-feedback effect is well maintained and further enhanced. Second-order DFB achieves improved outcoupling output power with similar dual-slit per unit cell structure [64]. Dominant TM polarized (E_y) electric-field along the whole length of cavity for antenna-feedback mode as the lowest loss mode and zoomed in (E_y) electric-field around the center of the cavity are shown in Fig. 3.17(c). The loss increases to ~ 14.5 cm^{-1} due to the increased outcoupling efficiency from this double-slit photonic cavity.

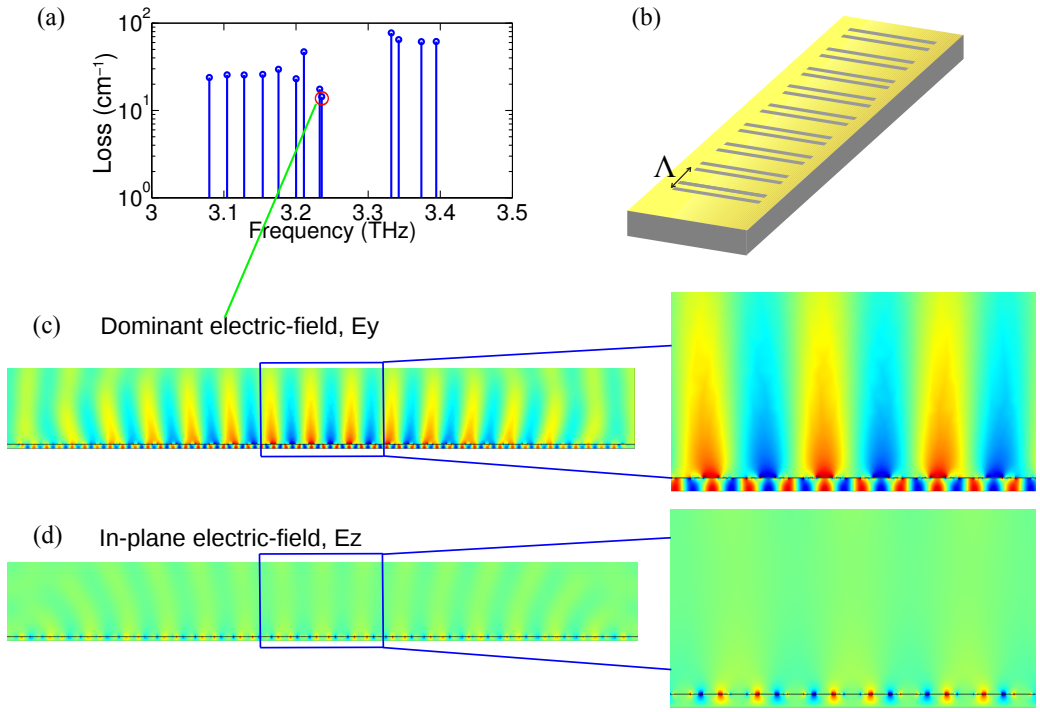

Figure 3.17: Structure 2 (one extra aperture is implemented for each of grating period) for antenna-feedback at ~ 3 THz . (a) Eigenmode spectrum for total length of cavity ~ 1.4 mm. (b) Schematic of new structure 2 to implement antenna feedback at ~ 3 THz. (c) Dominant TM polarized (E_y) electric-field along the whole length of cavity for antenna-feedback mode as the lowest loss mode. Right: zoomed in (E_y) electric-field around the center of the cavity. (d) In-plane (E_z) electric-field along the whole length of cavity for antenna-feedback mode. Right: zoomed in (E_x) electric-field around the center of the cavity.

Chapter 4

Large tuning of narrow-beam terahertz plasmonic lasers operating above liquid-nitrogen temperature

4.1 Introduction and various tuning methods for THz QCLs

Tunable single-mode terahertz QCLs are required for various applications such as high-resolution heterodyne spectroscopy and sensing. Output power in milliwatt level above liquid-nitrogen temperature, narrow beam pattern and large tunability are highly desired for THz QCLs. This chapter reports $\sim$ 57 GHz continuous and mode-hop-free tuning from single-mode terahertz quantum-cascade lasers (QCLs) emitting at $\sim$ 2.8 THz in a liquid-nitrogen cooled dewar at 78 K. The tuning is based on post-process deposition of Silicon-dioxide on a mounted and wire-bonded QCL implemented with the new antenna-feedback scheme (as discussed in Chapter 2), in which the lasing frequency of the resonant distributed-feedback mode can be tuned sensitively by changing the refractive-index of the surrounding medium. The

effect of dielectric deposition on laser's characteristics is demonstrated, including maximum lasing temperature, peak output power and far field beam pattern. A low-divergence beam quality is maintained. Compared with previous results that were demonstrated at low-temperatures($\sim$ 10K), an improved and broader tuning range is achieved at higher operating temperatures ($\sim$ 78K) for terahertz QCLs, which are more suitable and desired for practical applications.

Plasmonic lasers that utilize metal-clad cavities confine electromagnetic energy in the form of surface-plasmon-polaritons (SPPs) at subwavelength dimensions. They have seen a rapid development for targeted applications in nanoscale optics and integrated optical sensing. The most common types of plasmonic lasers utilize Fabry-Pérot type cavities in which one dimension is not subwavelength and is typically much longer than the other two dimensions [33, 34, 35]. For applications requiring spectral purity (single-mode operation) at the desired wavelength, tunability is a desired characteristic that is challenging to implement for such lasers. This stems from the difficulty in external control of the resonant-cavity mode such as that in conventional external-cavity tuning techniques for semiconductor lasers, since the subwavelength characteristics of such lasers lead to poor coupling between the cavity-modes with free-space propagating modes. Prior work on the development of tunable plasmonic lasers has primarily focused on changing the gain medium of the cavity itself [65, 66]. Terahertz quantum-cascade lasers (QCLs) [17, 32, 67] with metallic cavities [22] are one such subset of plasmonic lasers, which also suffer for such challenges with respect to their tunability.

Terahertz QCLs are the brightest available solid-state sources [68] of coherent terahertz radiation. They have witnessed significant development in the past decade in multiple areas such as wave engineering with distributed-feedback (DFB) techniques [43], output-power [69], temperature performance and frequency-coverage [70, 19, 71], and frequency tunability [72]. Single-mode terahertz QCLs are specifically required for a multitude of applications in sensing and spectroscopy. However, due to limits on accuracy of lithography utilized to implement DFB, it is still challenging to achieve single-mode emission from DFB QCLs at the exact desired frequency for applications such as high-resolution heterodyne spectroscopy [73, 74]. Frequency

tuning post-fabrication is desired to overcome this problem. Up to now, a variety of tuning techniques for terahertz QCLs have been demonstrated. Temperature tuning is simple but lacks large tunability [25]. Techniques such as applying external-cavities [75, 76] or modal perturbation using electromechanical methods [77, 78, 79] have the ability to achieve large tuning range but at the cost of discontinuous tuning, or system complexity and poor radiation patterns and temperature performance for such QCLs respectively.

A static-tuning technique based on post-process dielectric deposition was recently demonstrated for terahertz QCLs with third-order DFB operating at ~ 10 K with a tuning of ~ 5 GHz [80]. (The tuning could be extended while the QCL is in operation, but only temporarily, by deposition of solid nitrogen through multiple-cycle condensation to ~ 25 GHz in a liquid-Helium cryostat). Along similar lines, we here demonstrate a greatly enhanced continuous tuning range of ~ 57 GHz for single-mode QCLs emitting at 2.8 THz and operating at 78 K, achieved by deposition of Silicon-dioxide post-fabrication, and with significantly improved beam profiles. Prior work on large (> 20 GHz) tuning in Refs. [77, 78, 80] is achieved by perturbing the lateral evanescent mode of metallic cavities, which requires the cavities to be made very narrow (deep-subwavelength, $\lesssim 10$ μm wide cavities with the standard 10 μm thickness), and thereby makes the fabrication very challenging (with the requirement of sophisticated dry-etching techniques) as well as degrades the temperature and power performance of the QCLs considerably. In contrast, the tuning in this thesis places no such restrictions on the dimensions of the QCL cavity and is demonstrated for wide cavities processed with routine wet-etching methods. The large tuning is facilitated by a "antenna-feedback" scheme for plasmonic lasers (details are discussed in Chapter 2), which was experimentally implemented for terahertz QCLs with metallic cavities [62]. This mode-hop free tuning performance can be controlled by the thickness of the deposited Silicon-dioxide, it is also reversible, and can be implemented on already mounted and soldered QCL chips, which makes it attractive for future commercialization of single-mode terahertz QCLs. Importantly, in contrast to all previous tuning results for terahertz QCLs that have been

demonstrated at temperatures close-to that of liquid-Helium, the work in this chapter achieves a large tuning for QCLs operating in a liquid-Nitrogen cooled dewar since the tuning mechanism does not impact the gain of the QCL sensitively. Neither does the tuning method mandate a large dynamic range in current for the QCL in operation, which is in contrast with the methods relying on frequency-pulling due to Stark-shifted gain spectrum with changing electrical bias of the QCL that requires operation at low-temperatures [81, 82, 83].

4.2 Description of the tuning technique

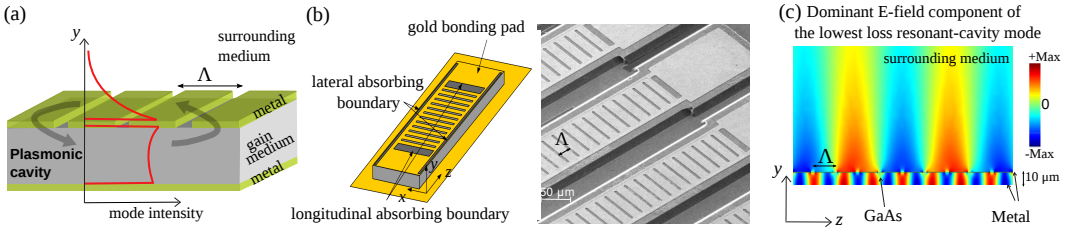

Figure 4.1: (a) Illustration of the antenna-feedback scheme for plasmonic lasers, which leads to generation of a hybrid surface-plasmon-polariton (SPP) mode in the surrounding medium of the laser's cavity. Here, a parallel-plate metallic cavity of a plasmonic laser is shown with slit-like apertures in its top metal cladding with a specific periodicity Λ as determined from equation (4.1), which lead to coupling of a guided SPP wave inside the cavity (interacting with the gain medium) with a single-sided SPP wave with a large spatial extent in the surrounding medium and propagating on the opposite side of the metal-cladding. (b) Schematic of terahertz plasmonic QCL with antenna-feedback grating implemented in the top-metal cladding with a periodicity Λ. The lateral and longitudinal absorbing boundaries are implemented to selectively excite the desired fundamental mode. A scanning electron microscope image of the fabricated QCLs is also shown. (c) The dominant electric-field component (E_y) of the lowest-loss resonant-cavity DFB mode is plotted along z axis, computed with finite-element (FEM) simulations using a commercial software package (Comsol 4.3). The height of the cavity is 10 μm. A hybrid SPP mode is excited in the surrounding medium along with the cavity SPP mode as illustrated in (a).

Plasmonic lasers, of which the terahertz QCLs with metallic cavities are a specific

example, lead to highly divergent far-field radiation patterns owing to the subwavelength dimensions of their radiating apertures. The antenna-feedback scheme for plasmonic lasers [62] couples the resonant surface-plasmon-polariton (SPP) mode in the cavity to a highly directional far-field radiation pattern. This occurs by exciting hybrid SPPs with a large spatial extent in the surrounding medium of the cavity by the mechanism of Bragg diffraction, which is affected by implementation of a grating in the metal-cladding of the plasmonic laser as illustrated in Fig. 4.1(a). With the choice of a specific periodicity in the grating, the resonant SPP wave inside the cavity is coupled via distributed-feedback (DFB) to a hybrid SPP wave that can propagate in the surrounding medium on the opposite side of the metal-film being used in the cavity of the plasmonic laser.

For terahertz QCLs with metallic cavities the antenna-feedback scheme could be implemented by introducing slit-like-apertures in its top metallic cladding as shown schematically in Fig. 4.1(b). For a chosen grating periodicity Λ, a DFB mode with free-space wavelength λ (and frequency $\nu = c/\lambda$) given by the equation

$$\lambda \;=\; (n_{\mathrm{c}} + n_{\mathrm{s}})\,\Lambda \tag{4.1}$$

is resonantly excited for the case when the coupling between the SPP wave in the cavity and the SPP wave in the surrounding medium is via first-order Bragg diffraction [62]. Here, n_{c} is the effective propagation index of the SPP wave inside the cavity (which is approximately the same as the refractive-index of the cavity's active medium) and n_{s} is the effective propagation index of the hybrid SPP wave in the surrounding medium (which is approximately the same as the refractive-index of the surrounding medium).

Equation (4.1) is distinctly different from that of any other solid-state DFB laser reported in literature, in that the refractive index of the surrounding medium is equally important in setting the resonant-frequency of the DFB mode of the laser as is the refractive index of the active medium inside the cavity. In other conventional solid-state lasers, the effect of the surrounding medium on the resonant-frequency is primarily a function of the fraction of evanescent mode of the cavity that propagates in its surroundings (typically represented by a mode-confinement factor, Γ), which

is also the case for the tunable terahertz QCL reported in Ref. [80]. However, in the antenna-feedback scheme, the contribution of the surrounding medium is related to phase-matching [62] rather than depending on the fraction of the overall electromagnetic energy propagating outside the cavity. Consequently, the resonant-frequency of the DFB mode depends sensitively on the refractive-index of the surrounding medium which can be altered to tune the frequency of the plasmonic laser, and is the technique employed for terahertz QCLs presented here. To the best of our knowledge, this is a unique mechanism to tune the frequency of a solid-state laser for which there is no analogous precedent in literature.

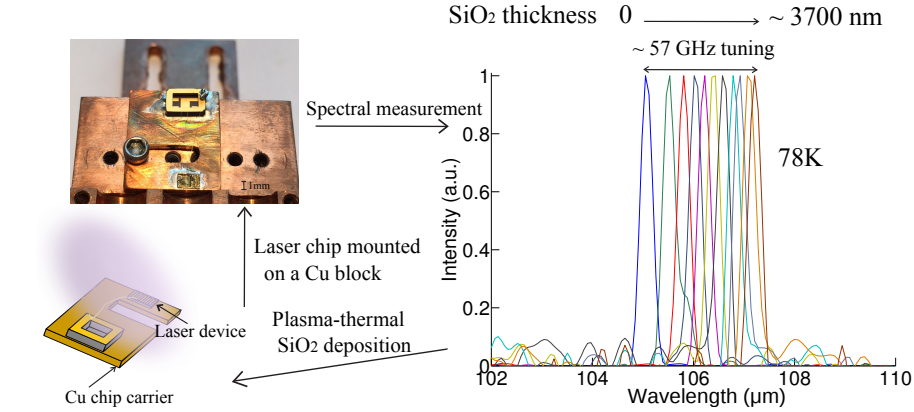

Figure 4.2: Optical image of a mounted QCL semiconductor chip out of which one of the QCLs with the antenna-feedback scheme is wire-bonded for electrical characterization. The QCL chip is soldered on a small copper chip that itself is screwed onto a bigger copper heat-sink to be mounted on the cold-plate of a cryogenic dewar. Multiple rounds of Silicon-dioxide deposition and cryogenic measurements were performed on the soldered and mounted QCL chip using PECVD. The tuning of the QCL's single-mode lasing spectrum is shown as a function of the thickness of the deposited oxide. Spectra were measured after each deposition step when the QCL was operated in a liquid-Nitrogen cooled dewar at 78 K in pulsed mode at an operating current of $\sim$ 570 mA (current-density $\sim$ 405 A/cm^2). A net tuning of $\sim$ 57 GHz tuning is demonstrated for an overall deposited thickness of $\sim$ 3700 nm.

A 10 μm thick terahertz QCL structure was grown by molecular beam epitaxy with a three-well resonant-phonon GaAs/$Al_{0.10}Ga_{0.90}As$ design scheme [57]. The

metallic QCL cavities with antenna-feedback gratings were fabricated using standard wafer-wafer thermocompression bonding and contact lithography technique. The fabrication steps are discussed in details in Chapter 2. A scanning electron microscope image of the finally fabricated QCL devices is shown in Fig. 4.1(b). Fig. 4.1(c) shows a 2D finite-element (FEM) simulation of the dominant TM-polarized (E_y) electric-field for a typical cavity (of infinite-width, for 2D simulation) with antenna-feedback gratings in the top-metal cladding. As can be seen, the the resonant DFB mode excites a single-sided SPP wave in the surrounding medium, which is established as a standing-wave on the top-metal cladding with a large spatial extent in the vertical dimension (y direction). Hence, any changes in the refractive index of the surrounding medium serve to change the effective propagation constant n_{s} of the single-sided SPP mode, which tunes the excitation frequency of the resonant-DFB mode according to equation (4.1).

4.3 Results

The active-medium of the QCLs is based on a three-well resonant-phonon design with GaAs/$Al_{0.10}Ga_{0.90}$As superlattice (design RTRP3W197, wafer number VB0464), which is described in Ref. [57], and was grown by molecular-beam epitaxy. The QCL superlattice is 10 μm thick with an average n-doping of 5.5×10^{15} cm^{-3}, and surrounded by 0.05 μm and 0.1 μm thick highly-doped GaAs contact layers at 5×10^{18} cm^{-3} on either side of the superlattice. Fabrication of QCLs with parallel-plate metallic cavities followed a Cu-Cu thermocompression wafer bonding technique as in Ref. [25] with standard optical contact lithography. Lateral and longitudinal absorbing boundaries were implemented by exposing the highly doped GaAs layer in the finally fabricated cavities, and the fabrication procedure is the same as in Ref. [62]. Ti/Au metal layers of thickness 25/200 nm were used as the top metal cladding, using an image-reversal lithography mask for implementing gratings in the metal layers. Another positive-resist lithography step was used to cover the grating-metal with photoresist to be used as a mask for wet-etching of ridges in a

H_2SO_4:H_2O_2:H_2O 1:8:80 solution. A Ti/Au contact was used as the backside-metal contact for the finally fabricated QCL chips to assist in soldering. Before deposition of backside-metal of the wafer, the substrate was mechanically polished down to a thickness of ~ 170 μm to improve heat-sinking.

By deposition of Silicon-dioxide post-fabrication (after the QCL chip is already mounted and wire-bonded on a copper mount), the lasing frequency of the resonant antenna-feedback mode is tuned sensitively. Fig. 4.2 shows the variation of a specific QCL's wavelength of emission when increasing the thickness of blanket deposited Silicon-dioxide on the entire QCL chip. As expected from equation (4.1), the lasing wavelength undergoes a red-shift with increasing thickness of the oxide, since then, the effective propagation index n_s for the SPP wave in the surrounding medium of the QCL will increase. The measured QCL has a grating period $\Lambda = 25$ μm and the cavity's dimensions are 100 μm $\times$ 1.4 mm $\times$ 10 μm. A cleaved chip consisting of QCLs with antenna-feedback gratings was In-soldered on a Cu block, the QCL to be tested was wire-bonded for electrical biasing, and the Cu block was mounted on the cold-stage of a liquid Nitrogen vacuum cryostat for measurements. In this experiment, the frequency of the QCL was first measured without any dielectric deposition, and it radiated in a single-mode at ~ 2.85 THz ($\lambda \sim 105$ μm). Afterwards, the resonant-frequency is changed by depositing Silicon-dioxide on top of the mounted QCL chip using a plasma-enhanced chemical vapor deposition (PECVD) system. The deposited thickness is carefully calibrated by simultaneously including a bare GaAs wafer in the PECVD chamber for each deposition step. QCL's spectra were measured at 78 K in linear-scan mode with a resolution of 0.2 cm^{-1} using a FTIR with room-temperature pyroelectric detector. Multiple cycles of spectral measurement and oxide-deposition were implemented and the tuning results are collected and shown in Fig. 4.2, which illustrates a large red-shift tuning with this mechanism. Finally, a mode-hop-free and continuous tuning of ~ 57 GHz was achieved after an overall deposited thickness of ~ 3700 nm. Further tuning could not be realized since QCL stopped lasing at 78 K beyond the stated thickness. The spectra shown in Fig. 4.2 were all measured at similar bias currents. When etching away the deposited SiO_2 on top of the laser device by buffered-HF (BOE 7 : 1)

etchant, the QCL was characterized again and its emission properties including the lasing wavelength returned to its original value, which illustrates that tuning by post-process deposition of SiO_2 on terahertz QCLs here is a reversible method.

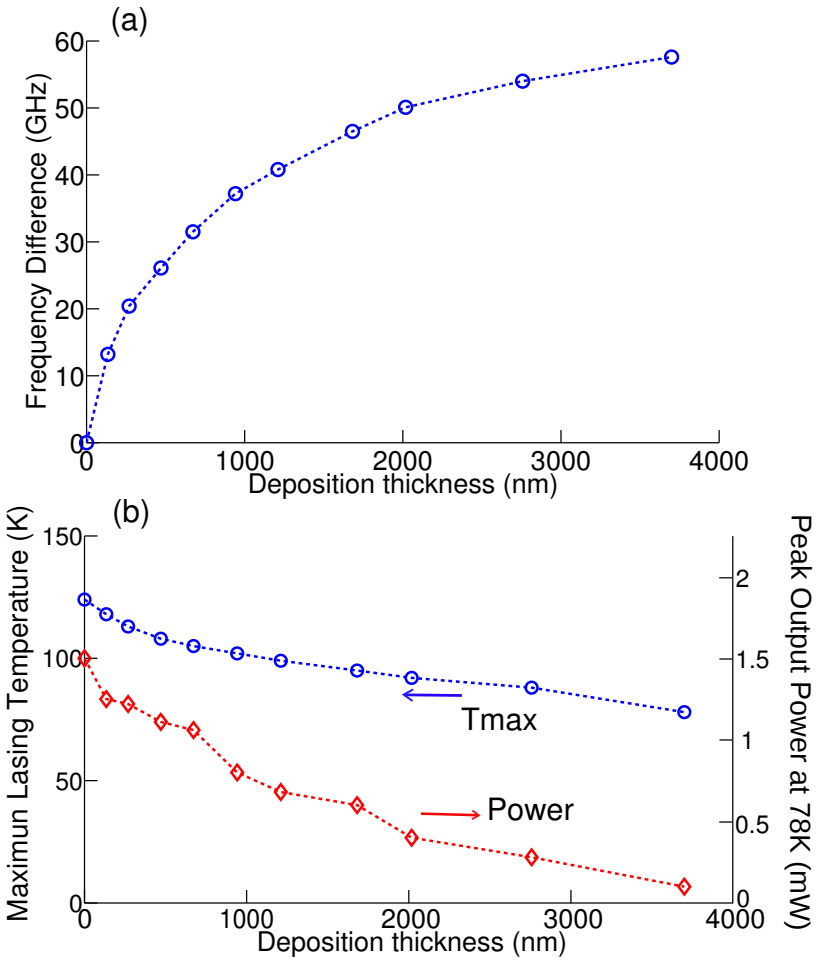

Figure 4.3: (a) Emission frequency of the terahertz QCL with antenna-feedback as a function of the deposited thickness of Silicon-dioxide, expressed as a difference from its original emission frequency of ~ 2.85 THz without any oxide. The QCL is biased slightly below the peak-power bias region where it radiates in a single-mode (detailed spectra with bias are shown in Fig. 4.5). (b) Maximum operating temperature ($T_{\max}$) and the detected peak optical power at 78 K for the QCL in pulsed operation, as a function of the thickness of the Silicon-dioxide.

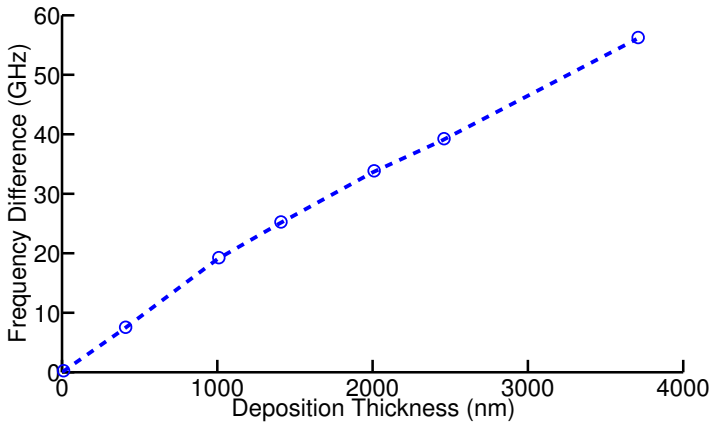

Figure 4.4: Frequency difference of resonant lowest loss mode from terahertz QCL with antenna-feedback as a function of the thickness of Silicon-dioxide on top of the cavity from 2D simulations.

Figure 4.3(a) characterizes the variation of the QCL's emission frequency as a function of thickness of the deposited Silicon-dioxide. The variation is non-linear, and the rate of tuning as a function of oxide-thickness decreases as more oxide is deposited. A 2D finite-element simulation was not able to reproduce this non-linear tuning since the hybrid SPP mode in the surrounding medium of the cavity in the vertical direction (above the cavity) has a large spatial extent. Correspondingly, the tuning computed with 2D simulations is predominantly linear for an overall oxide thickness of few microns as shown in Figure 4.4. However, it is argued that the non-linear tuning behavior as observed here is due to the complex spatial nature of the SPP mode in the surrounding medium in the lateral dimensions [62], which could only be captured by 3D simulations that are outside the scope of this present work due to hardware limitations in performing such simulations. And since thin-film oxide deposited by PECVD is a lossy material at terahertz frequencies, accurate choice of imaginary part of thin-film oxide is unknown, especially at low deposition temperature around 100 degree C for the consideration of the Indium-soldered mounted QCL wafer in this case. The dependency of measured maximum lasing temperature

and peak output power at 78 K with oxide thickness is shown in Figure 4.3(b). Without any post-process deposition of the oxide, this terahertz QCL device lased up to 124 K with peak output-power of $\sim$ 1.5 mW at 78 K. When deposition thickness reaches $\sim$ 3700 nm and $\sim$ 57 GHz tuning is obtained, the maximum lasing temperature of this device is slightly above 78 K and the peak output-power reduces to $\sim$ 100 μmW at 78 K. The emitted optical power was measured with a deuterated triglycine sulfate pyroelectric detector (DTGS) (Gentec THz 2I-BL-BNC) and calibrated with a terahertz thermopile power-meter (ScienTech model AC2500H) without any optical component or cone collecting optic inside the cryostat. The power values are reported without any corrections to the detected signal.

Two factors contribute to the decrease in maximum lasing temperature and output-power of the QCL with increasing oxide thickness. First, thin-film oxide deposited by PECVD is a lossy material at terahertz frequencies for which the absorption coefficient could be as high as 20 cm^{-1} [84]. Secondly, the confinement factor Γ of the resonant-cavity mode, which is the fraction of the mode that resides in the active-medium, decreases as thicker oxide is deposited. This is primarily because the higher electric-permittivity of the oxide $\epsilon_{\text{ox}} \sim 4.4\epsilon_0$ (at terahertz frequencies). As a consequence the effective threshold gain is increased for exciting the resonant-cavity mode, which also reduces optical power due to an increase in the effective modal propagation loss in the cavity as well as reduction in the net dynamic range for lasing current. A precise analytical or numerical estimation of the net effect of oxide thickness on the threshold gain and QCL's temperature and power performance is beyond the scope of this work because, first, in case of terahertz QCLs various transport parameters as well as waveguide loss parameters cannot be predicted accurately, and second, the estimation of Γ requires 3D finite-element simulation of the QCL's cavity with deposited oxide that cannot be done due to aforementioned reasons.

Figure 4.5 shows light-current (*L-I*) characteristics in pulsed operation for the QCL operated at different heat-sink temperatures along with its lasing spectra at different bias when varying deposition thickness of the Silicon-dioxide. At start when no oxide is deposited, the QCL operated up to a maximum temperature $T_{\text{max}} \sim$

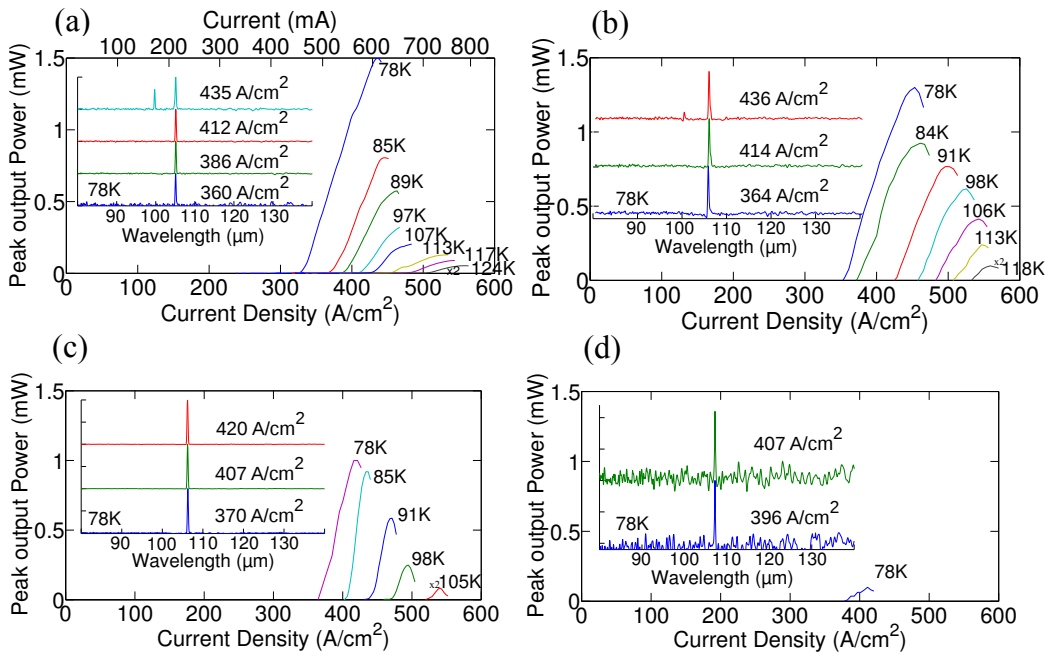

Figure 4.5: Light-current characteristics of the terahertz QCL with antenna-feedback scheme at different heat-sink temperatures. The dimensions of the QCL's cavity are 100 μm $\times$ 1.4 mm $\times$ 10 μm. The QCL is biased in pulsed mode with 400 ns wide pulses repeated at 100 kHz. The plot-insets show lasing spectra at 78 K as a function of increasing bias. (a) Original QCL without any oxide deposition, (b) QCL with 140 nm thick oxide leading to $\sim$ 13 GHz frequency tuning, (c) QCL with 700 nm thick oxide leading to $\sim$ 31 GHz frequency tuning, and (d) QCL with 3700 nm thick oxide leading to the maximum tuning of $\sim$ 57 GHz for the QCL still lasing at 78 K.

124 K with peak output-power of $\sim$ 1.5 mW at 78 K. With $\sim$ 140 nm thick oxide, the maximum operating temperature reduced to 118 K and the peak output-power was similarly lowered to $\sim$ 1.25 mW at 78 K. The QCL predominantly radiates at a single frequency around 2.84 THz which corresponds to the desired DFB mode of the cavity. However, at higher current-densities closer to peak operating bias ($>$ 420 A/cm^2), a second mode at shorter-wavelength is excited, which suggests that a higher-order lateral mode was likely excited due to spatial-hole burning in the cavity (since such a mode has a smaller effective propagation index n_c in the cavity). The excitation of the higher-order lateral mode ceases in the entire operating range

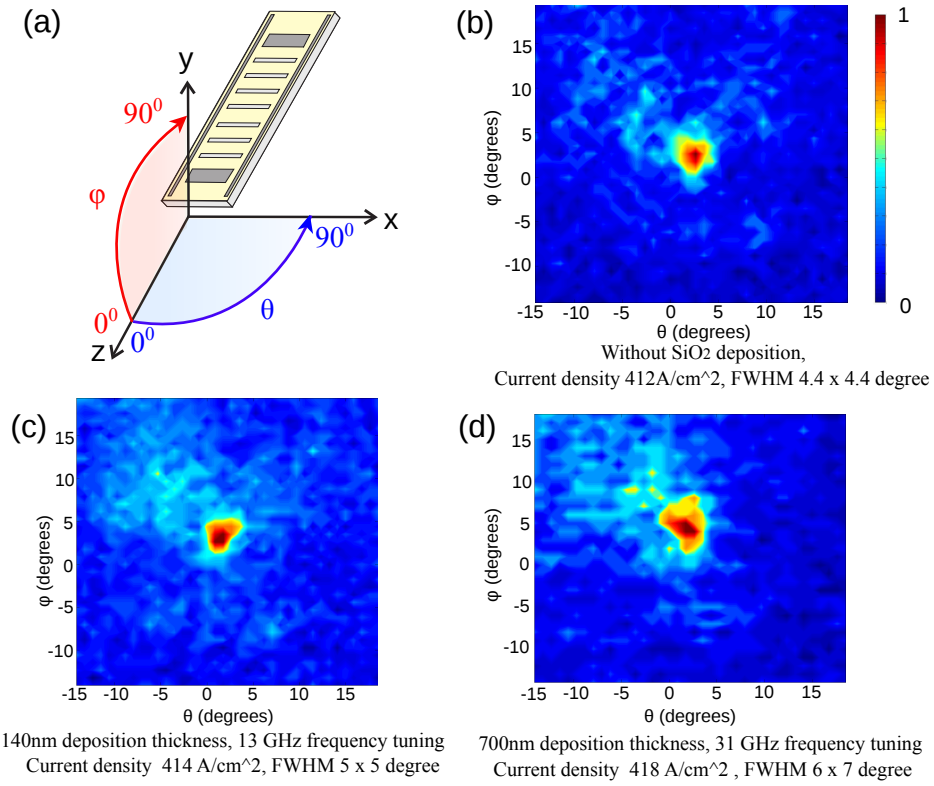

Figure 4.6: (a) Schematic showing orientation of the QCL and definition of angles for the shown far-field radiation patterns. The QCL was operated at 78 K in pulsed mode, and the radiation pattern was measured using a room-temperature pyroelectric detector of 2 mm diameter mounted on a $x-y$ movement stage. The radiation-pattern in (b) is for QCL without Silicon-dioxide deposition, in (c) is for QCL deposited with an oxide thickness of 140 nm, and in (d) is for an oxide thickness of 700 nm.

of the QCL as thicker oxide is deposited. When the oxide thickness is increased to $\sim$ 700 nm corresponding to $\sim$ 31 GHz frequency tuning, the QCL lased up to 105 K with peak output-power of $\sim$ 1 mW at 78 K. Single mode spectra with lasing frequency $\sim$ 2.82 THz were measured under all bias conditions over the whole dynamic range, namely from threshold until negative differential-resistance (NDR) as shown in Figure 4.5(c). When total thickness of the deposited oxide is $\sim$ 3700 nm, only limited spectra were recorded at current-densities of $\sim$ 396 A/cm^2 and $\sim$

407 A/cm^2 respectively while the QCL is still operating at 78 K in a liquid-Nitrogen cooled dewar. The QCL stopped lasing at 78 K when additional oxide was deposited. The threshold current-densities at 78 K for the aforementioned plots as shown in Fig. 4.5 are $\sim$ 328 A/cm^2, $\sim$ 350 A/cm^2, $\sim$ 364 A/cm^2, $\sim$ 390 A/cm^2 respectively, which increase with the thickness of the deposited oxide. From the data presented in Fig. 4.3 and Fig. 4.5 it can be noted that more than 60 % of the available tuning (i. e. $\sim$ 35 GHz tuning) could be realized by depositing less than 1 μm thick Silicon-dioxide, in which case there is no significant degradation in maximum operating temperature or power output from the QCL.

Radiation in a directional (narrow) beam is one of the most important and attractive characteristics of terahertz plasmonic QCLs with the antenna-feedback scheme [62]. Figure 4.6 shows the measured beam patterns of the QCL at 78 K for varying thicknesses of the deposited oxide. Far-field radiation patterns were measured with a DTGS pyroelectric cell detector mounted on a computer-controlled two-axis moving stage in the end-fire (z) direction at a distance of 65 mm from the QCL's end-facets. Without any oxide, the QCL emits in a single-lobed beam with narrow divergence with full-width half-maximum (FWHM) of $\sim 4.4^\circ \times 4.4^\circ$ as shown in Fig. 4.6(b). After 140 nm thick oxide was deposited, the radiation pattern remained single-lobed but with a slightly increased FWHM of $\sim 5^\circ \times 5^\circ$. A further deposition of oxide to a thickness of 700 nm increased the FWHM of the main lobe to $\sim 6^\circ \times 7^\circ$. The small increase in beam divergence for thicker oxide deposition is likely due to reduction in spatial extent of the SPP mode on top of the cavity with oxide thickness. Due to the limits in the sensitivity of the of the room-temperature DTGS detector, the radiation patterns could not be measured with a reasonable signal-to-noise ratio after deposition of even thicker oxide. However, since the QCL continues to radiate in the same cavity mode, it should retain its characteristic radiation into single-lobed narrow beams.

4.4 Discussion

Plasmonic lasers utilize metallic cavities to confine the electromagnetic mode at subwavelength dimensions. However, poor radiative coupling to free-space makes it difficult to statically or dynamically tune their emission frequency, which is required for practical applications. The tuning mechanisms demonstrated so-far involve an alteration of the gain-medium itself. Terahertz QCLs with metallic cavities suffer from the similar challenges that have prevented the development of tunable QCLs that could work at high-temperatures. In this chapter, we show that the antenna-feedback scheme for plasmonic lasers offers an ideal solution for both static tuning (as demonstrated here) or dynamic tuning and frequency modulation (in principle), while simultaneously achieving single-mode operation and narrow-beam emission from the sub-wavelength plasmonic cavities. The antenna-feedback scheme leads to the establishment of a hybrid SPP standing-wave in the surrounding medium of the laser's cavity with a large spatial extent. The emission frequency of the plasmonic laser depends sensitively on the effective propagation index of the SPP mode in the surrounding medium, which could be altered independently of the gain medium used inside the laser's cavity. Consequently small perturbations in the refractive-index of the surrounding medium could lead to large modulation in the laser's emission frequency. To the best of our knowledge, this is a unique mechanism to tune the frequency of a solid-state laser for which there is no analogous precedent in prior literature.

For terahertz QCLs, the antenna-feedback scheme was implemented for wide cavities that could operate well above the temperature of liquid-Nitrogen, in contrast with previous tuning techniques that have mostly utilized ultra-narrow cavities for access to the evanescent cavity modes. ~ 57 GHz static tuning is demonstrated for single-mode narrow-beam terahertz QCLs emitting at 2.8 THz, based on post-process deposition of Silicon-dioxide on an already soldered and mounted QCL chip. A beam divergence of $< 7^{\circ}$ was maintained through the tuning range. The degradation of maximum operating-temperature and power output is small for a large fraction of the tuning range. More than 50 % of the available tuning ~ 30 GHz

tuning) could be realized by depositing ~ 0.7 μm thick Silicon-dioxide, in which case $T_{\max}$ reduces from 124 K to 105 K and the peak output-power reduces from 1.5 mW to 1 mW. The tuning is reversible and continuous, and could pave the way for future commercialization of DFB terahertz QCLs for targeted applications in sensing and high-resolution spectroscopy. Whereas all previous tuning results for terahertz QCLs were demonstrated at operating temperatures close to that of liquid-Helium, the results presented here are for QCLs operating at the much more practical temperature of 78 K, while simultaneously achieving significantly more directional beams compared to previous reports.

Chapter 5

High power surface-emitting THz QCLs with single-lobed beam

For a second-order distributed-feedback grating, grating-period is the same as the wavelength of propagating mode inside the semiconductor. The grating acts like a phased-array antenna in the vertical direction to produce surface emission. Additionally, such a grating provides a strong feedback into the cavity for DFB action. The surface-emitting DFB laser achieves robust single-mode operation determined from the periodicity of the grating, as opposed to the unpredictable multi-mode lasing behavior of Fabry-Perot cavity. Also, it provides an improved beam-pattern profile with a divergence of 5 degree in the longitudinal direction, but very broad in the lateral emission due to the sub-wavelength width of the cavity [25]. This is an inherent characteristic of surface-emitting DFB lasers in rectangular ridge geometry [50, 25, 55], especially at terahertz frequencies where the ridge width could be smaller than the wavelength. Although wider ridges could be made to circumvent this problem, higher current flow leads to higher heat-dissipation that prevents operation in cw mode. In addition, conventional second-order DFB does not solve the problem of efficient out-coupling. In fact, it is the in-plane field that causes emission in the surface normal direction, which has nulls precisely at the grating apertures as shown in Chapter 1. Therefore, the surface-loss of the lasing mode is small, which

translates to negligible outcoupling of radiation, and hence very low output power. Moreover, for conventional second-order DFB, double-lobed far field beam has been reported without central phase shift [85], which makes it less attractive for various applications.

5.1 A new grating design for surface-emitting terahertz QCLs

For conventional second-order DFB, in-plane radiative field is always null under the apertures since the grating period is exactly the same as the guided wavelength, which leads to negligible outcoupling loss and small output. In this chapter, we propose a new photonic structure for second-order surface-emitting DFB, in which another aperture is introduced to alternating grating periods, as shown in Fig. 5.1(b). As a result, the surface loss of the lowest loss mode increases largely to ~ 8.6 cm^{-1}, as shown in Fig. 5.1(a), as compared with ~ 1 cm^{-1} for the conventional second-order DFB. The major fraction of EM energy for the resonant modes exists in TM polarized (E_y) electric-field, as can be seen from Fig. 5.1(c), each grating period corresponds to a group of one maximum, one minimum and one null field distribution of the lowest loss mode, which is a typical second-order DFB mode feature and a clear indication that the desired surface-emitting characteristics is maintained by employing this new photonic structures. More importantly, non-zero radiative field is achieved, as demonstrated in Fig. 5.1(d), which will lead to improved output power of second-order DFB. In this simulation, grating period is $\Lambda = 28.5$ μm, the frequency of the lowest loss resonant-mode is ~ 3.07 THz. The length of the grating aperture and the width of metal between original and adding aperture are 0.1Λ and 0.15Λ, respectively. These two key parameters can be optimized so as to get the maximum outcoupling loss and improve output power of terahertz QCLs.

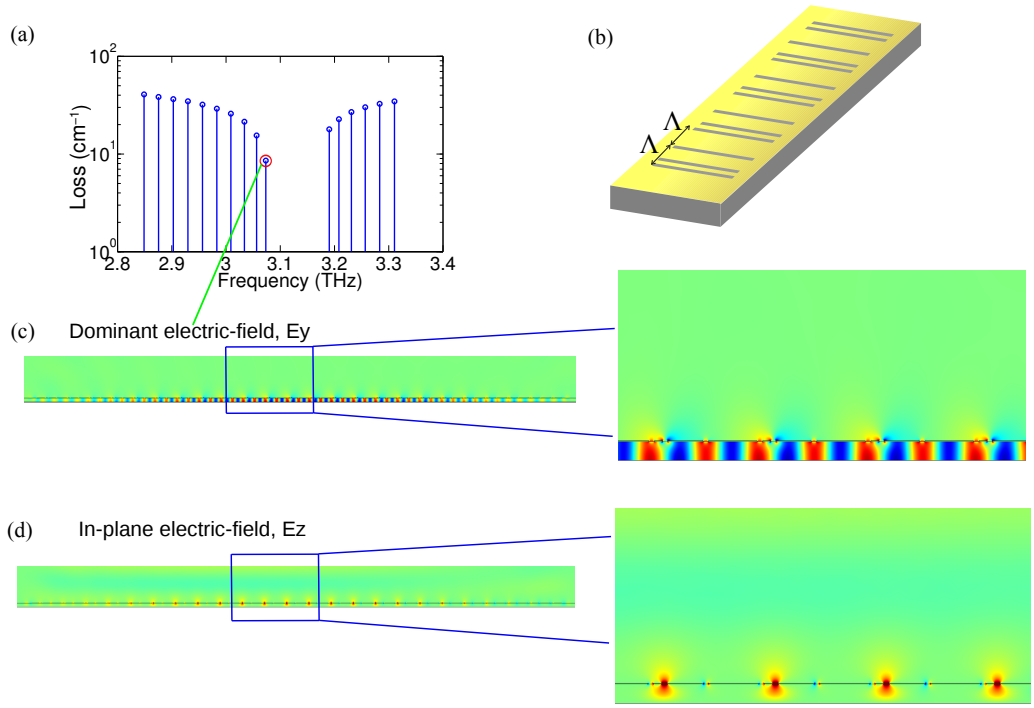

Figure 5.1: Photonic structure 1 (one extra aperture is implemented for alternating grating periods) for second-order DFB at $\sim$ 3 THz. (a) Eigenmode spectrum for total length of cavity $\sim$ 1.4 mm. (b) Schematic of new structure 1 for second-order DFB at $\sim$ 3 THz. (c) Dominant TM polarized (E_y) electric-field along the whole length of cavity for the lowest loss mode. Right: zoomed in (E_y) electric-field around the center of the cavity. (d) In-plane (E_z) electric-field along the whole length of cavity for the lowest loss mode. Right: zoomed in (E_z) electric-field around the center of the cavity.

5.2 Beam pattern from 3D simulations

Terahertz QCLs with conventional second-order DFB produces doubled-lobed beam without any central phase shift due to the fact that the radiation from each half of the device adds destructively in the direction normal to the laser surface, resulting in a null in the center of the far-field radiation pattern. The phase shift can be added in the top metal grating with length equals to half of the grating period. Adding

such a phase shift has the effect of propagating each plane wave in the Floquet-Bloch expansion of the symmetric and antisymmetric modes by a length of half of grating period so that it produces a sign change for the odd-order plane waves in the Floquet-Bloch expansion but has no effect on the even-order plane waves. In the presence of the phase shift, the symmetric component of the field has the same sign on both ends of the device and it transforms the antisymmetric near field pattern into one which is symmetric along the length of the device. Consequently, the radiated component is in phase throughout the length of the device and produce a single main lobe in the far-field.

For second-order DFB with the new photonic design shown in Fig. 5.1, there is no such requirement of an additional π phase shift in the cavity. Radiation from both halves of the device add constructively in the surface normal direction, resulting in a single-lobed far-field beam pattern, as shown in the beam pattern from 3D simulations in Fig. 5.2. The surface-emitting terahertz QCLs with this new designed second-order Bragg grating is able to obtain narrow beam-pattern in the longitudinal direction(along the length direction of laser ridge) without any phase shift at the center of the laser cavity.

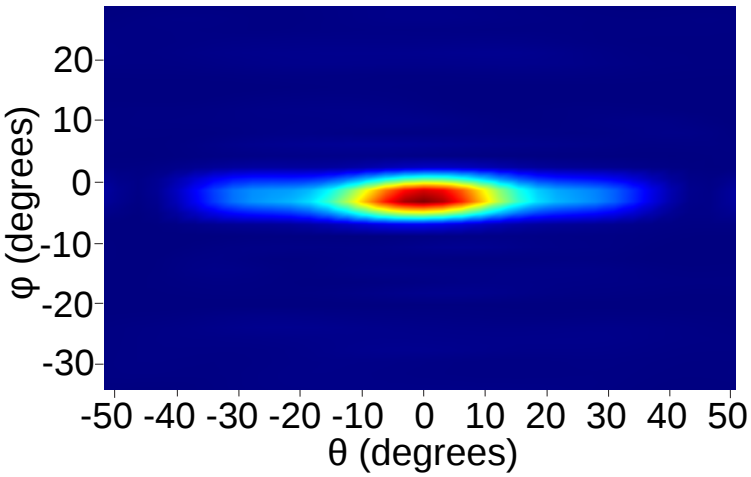

Figure 5.2: Simulated beam pattern of second-order DFB with the new photonic cavity structure 1.

5.3 Experimental results

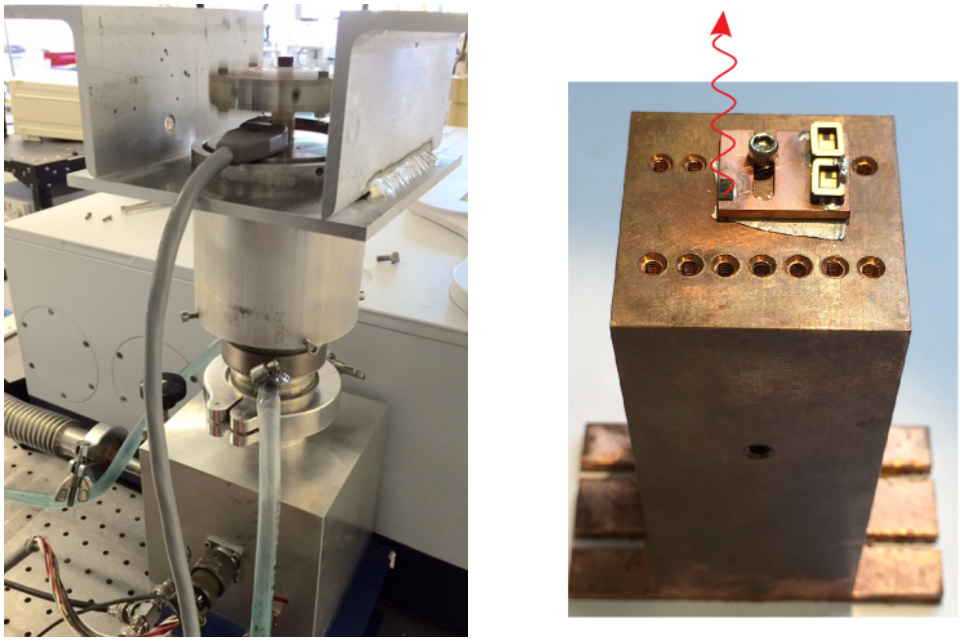

Figure 5.3: Picture of cryocooler operated at 50 K and copper mount to measure surface-emitting lasers .

5.3.1 Conventional second-order DFB with 100 μm width

Surface-emitting THz QCLs were mounted on a custom-designed Cu mount, and this Cu mount was installed in a Stirling cryocooler, as shown in Fig. 5.3, which could be operated to low temperature $\sim$ 51 K. Fig. 5.4 shows L-I curves versus heat-sink temperature for a QCL with a conventional second-order DFB with grating period $\Lambda = 26$ μm, $\sim$ 100 μm width and $\sim$ 1.25 mm length. The QCL lased up to a temperature of 124 K. The inset shows the measured spectra with different bias at $\sim$ 55 K, a robust single-mode operation under all bias conditions is achieved within the entire dynamic ranges. The lasing wavelength is $\sim$ 92.2 μm (lasing frequency is $\sim$ 3.25 THz). Peak-power output of $\sim$ 5 mW at $\sim$ 51 K was detected from this THz QCL with the conventional second-order DFB grating measured directly at the

detector without using any collecting optics.

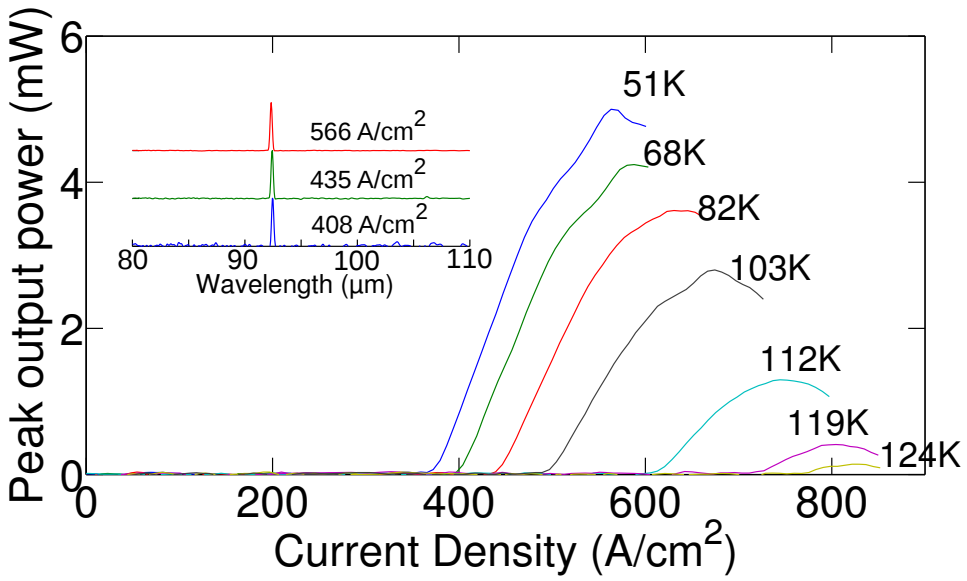

Figure 5.4: Measured light-current curve at different heat-sink temperatures of conventional second-order DFB with 100 μm width. Inset: measured spectra at different bias at $\sim$ 55 K.

Fig. 5.5 shows the measured beam pattern of a conventional second-order DFB with 100 μm width. Orientation of QCLs and angle of beam measurement are shown in Fig. 5.5. A clear double-lobed far-field radiation pattern is obtained and a null in the center between two lobes can be observed without adding a phase shift in the designed grating. The beam pattern is measured with a current density $\sim$ 560 A/cm^2, where the desired single mode spectra is recorded.

5.3.2 Second-order DFB with new photonic cavity with 70 μm width

Fig. 5.6 shows *L-I* curves versus heat-sink temperature for a QCL with second-order DFB with new photonic structure 1. This device has similar length as the one reported in Fig. 5.4, but with a narrower width of $\sim$ 70 μm. As discussed in section 5.1, the new photonic structure 1 improved the out-coupling loss of second-order

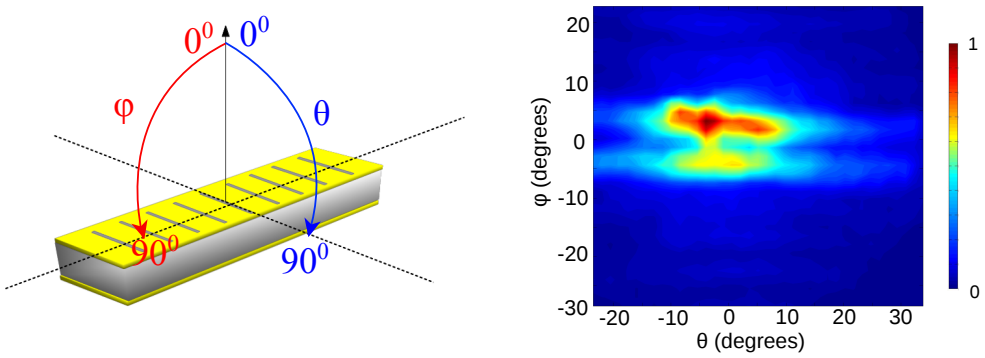

Figure 5.5: Measured beam pattern of conventional second-order DFB with 100 μm width. Schematic on the left shows the orientation of QCLs and definition of angles.

DFB cavity efficiently, so that a higher peak output power $\sim$ 7 mW at $\sim$ 51 K is recorded, even with $\sim$ 70 μm narrow cavity. Output power was detected from this THz QCL with the new second-order DFB grating without any cone collecting optics. The QCL operated up to a temperature of 81 K. The increased loss results in the decreased maximum lasing temperature. The inset shows measured spectra at different bias at $\sim$ 55 K. Robust single-mode spectra are measured under all the bias conditions within the whole dynamic ranges, which confirms the working principle of the new design with photonic structure 1.

Fig. 5.7 shows the measured beam pattern of second-order DFB with 70 μm width with new design of photonic structure 1. The angle definition is the same as that in Fig. 5.5. A single-lobed far-field radiation pattern is measured, serving as a clear comparison with the doubled-lobed beam pattern as shown in Fig. 5.5 from the conventional second-order DFB. The FWHM of the beam in Fig. 5.7 is $\sim 4^\circ \times 14^\circ$. The beam pattern is measured with current density $\sim$ 648 A/cm^2, while lasing in single mode.

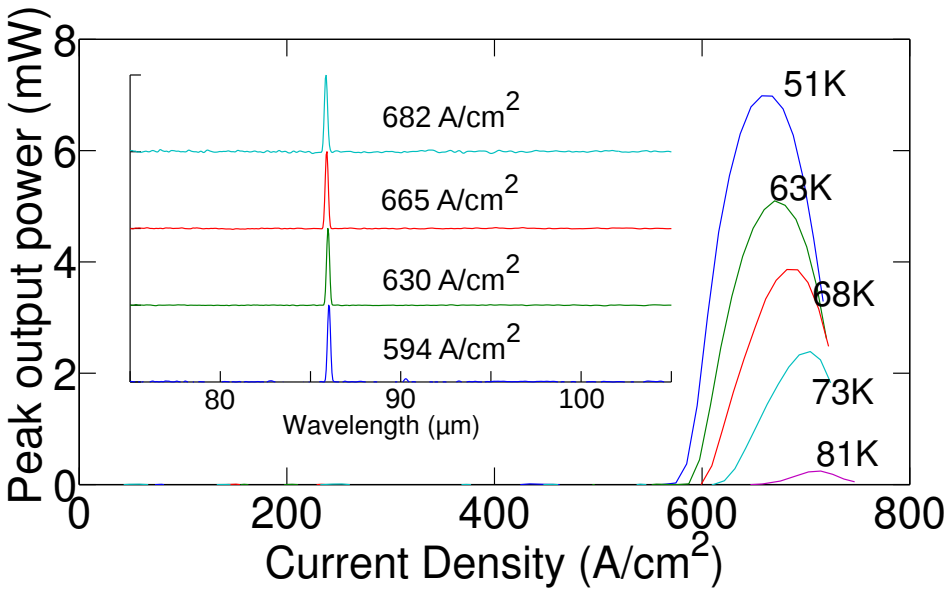

Figure 5.6: Measured light-current curve at different heat-sink temperatures of new photonic structure 1 second-order DFB with 70 μm width. Inset: measured spectra at different bias at $\sim$ 55 K.

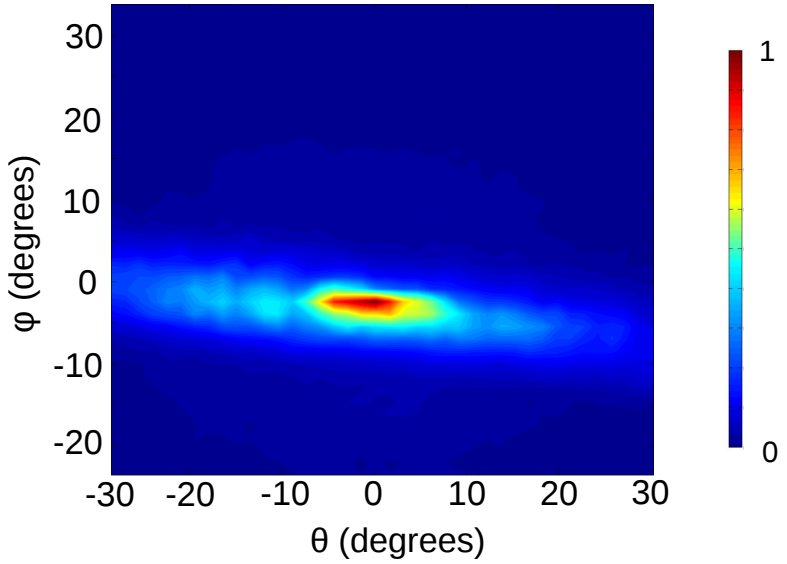

Figure 5.7: Measured beam pattern of second-order DFB with new photonic structure 1 with 70 μm width.

5.3.3 Second-order DFB with new photonic cavity with 200 μm width

Fig. 5.8 shows *L-I* characteristics versus heat-sink temperature for a QCL with second-order DFB with new photonic cavity structure 1. The designed grating period is $\Lambda = 27$ μm, the cavity dimensions are ~ 200 μm width and ~ 1.25 mm length. Peak output power of ~ 50 mW at ~ 51 K was detected from this THz QCL with second-order DFB grating with new photonic structure 1, which is one of the highest output power values reported from single-mode terahertz QCLs. The power was measured directly by the detector without using any collecting optics. The record output power from single-mode terahertz QCLs is ~ 67 mW at ~ 77 K from the graded grating period [56, 86, 87] second-order DFB with cavity width ~ 214 μm. Both of these techniques achieves high output power due to the same reason, namely the non-zero radiative field by photonic engineering of laser's waveguide.

This QCL operated up to a temperature of ~ 90 K. The inset shows spectra measured at different bias at ~ 55 K, demonstrating robust single-mode operation ~ 90.8 μm, ~ 3.3 THz, under all the bias conditions within the whole dynamic ranges.

Fig. 5.9 shows the measured beam pattern of second-order DFB with 200 μm width with new design of photonic structure 1. A single-lobed far-field radiation pattern is observed with a FWHM of $\sim 7^\circ \times 26^\circ$. The beam pattern is measured with current density ~ 520 A/cm^2, while lasing in single mode.

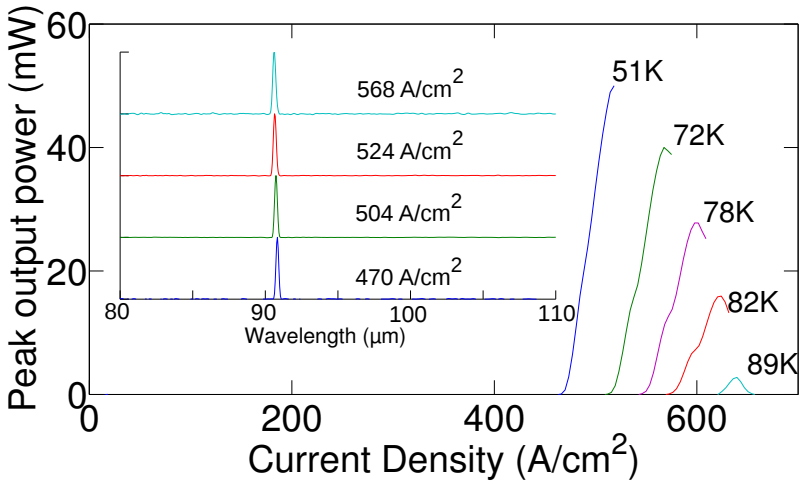

Figure 5.8: Measured light-current curve at different heat-sink temperatures of new structure 1 second-order DFB with 200 μm width. Inset: measured spectra at different bias at $\sim$ 55 K.

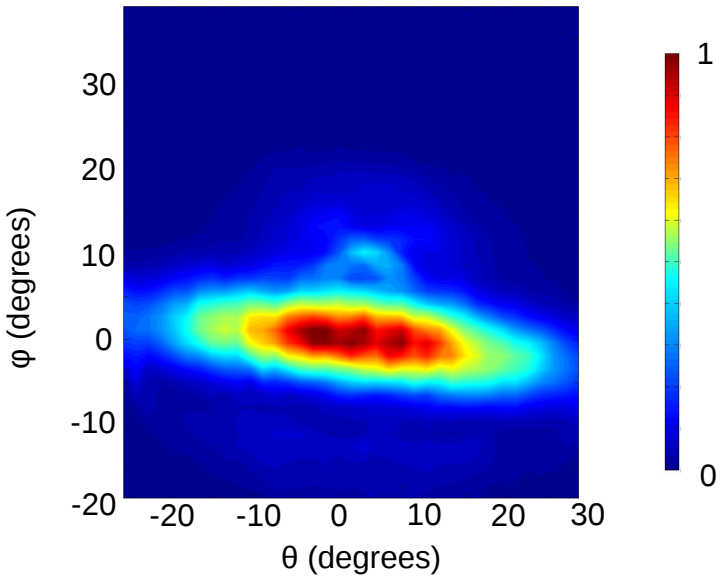

Figure 5.9: Measured beam pattern of second-order DFB with new photonic structure 1 with 200 μm width.

Chapter 6

Conclusions and future outlook

6.1 Conclusions

In conclusion, this thesis demonstrates a unique scheme for implementing distributed-feedback (DFB), called antenna-feedback, in plasmonic lasers, such that the laser can radiate in a highly directional beam. One of the biggest challenges for plasmonic lasers is that they have highly divergent radiation patterns due to the sub-wavelength dimensions. The theoretical idea of antenna-feedback is applicable to plasmonic lasers operating at any wavelength. In this thesis, the experimental demonstration is done with a specific class of plasmonic lasers which work at far-infrared wavelengths, the terahertz quantum-cascade lasers (QCLs). This thesis has obtained the narrowest beaming characteristics to-date for terahertz QCLs. And the new antenna-feedback does not require a well-defined effective index to meet the phase-matching condition.

This new approach of implementing DFB in semiconductor lasers integrates surface-plasmon-polaritons (SPPs) in the surrounding medium of the laser's cavity into the operation of DFB lasers, demonstrates a novel mode selection, out coupling and laser feedback mechanism, as well as produces an ultra-narrow beam pattern. This DFB method breaks that periodicity strictly follows the integer multiple of half-wavelength inside active medium for the first time and enhances the

radiative-field.

The coherent single-sided SPPs are generated on the metal film which has a large spatial extent in the surrounding medium of the laser's cavity, which could have important implications for applications in integrated plasmonics. Coherent SPPs with a large spatial extent could also make it easy to couple SPP waves from the plasmonic lasers to other photonic components, and could also potentially be utilized for plasmonic sensing. Fig. 6.1 shows an artistic illustration of the unique characteristics of antenna-feedback that there is a coherent SPP mode on top of laser cavity in addition to that inside the active medium. The new antenna-feedback demonstrated in this thesis could make a noticeable impact not only to the field of terahertz QCLs, but also the broader scientific communities of plasmonic lasers or spasers by providing an elegant solution to a long-standing challenge for such lasers and pave a solid way for plasmonic lasers to step into practical applications.

This thesis also demonstrates a unique and novel tuning mechanism for metal-clad plasmonic distributed-feedback (DFB) lasers. A large, reversible, continuous, and mode-hop-free tuning of ~ 57 GHz for single-mode narrow-beam terahertz plasmonic quantum-cascade lasers (QCLs) operated in a liquid-nitrogen cooled dewar is reported. The key enabling mechanism for tuning is the antenna-feedback scheme for plasmonic lasers developed in this thesis, which leads to the generation of hybrid surface-plasmon-polariton (SPP) propagating outside the cavity of the laser with a large spatial extent. Refractive-index of the surrounding medium of laser cavity affects the resonant-frequency of DFB mode sensitively and dramatically.

Specifically, at first, this thesis achieves a considerably larger tuning range compared to previously reported results for single-mode terahertz QCLs with directional far-field radiation patterns. Secondly, the tuning is demonstrated at the much more practical operating temperature of 78 K, whereas all previous tuning results for terahertz QCLs have been reported at low-temperatures close-to that of liquid-Helium 10 K. Thirdly, single-lobed beam with low divergence ($< 7^{\circ}$) is maintained through the tuning range, which is the narrowest divergence for any tunable terahertz QCL to-date. In addition, in the antenna-feedback scheme, the contribution of the surrounding medium is due to considerations of phase-matching rather than

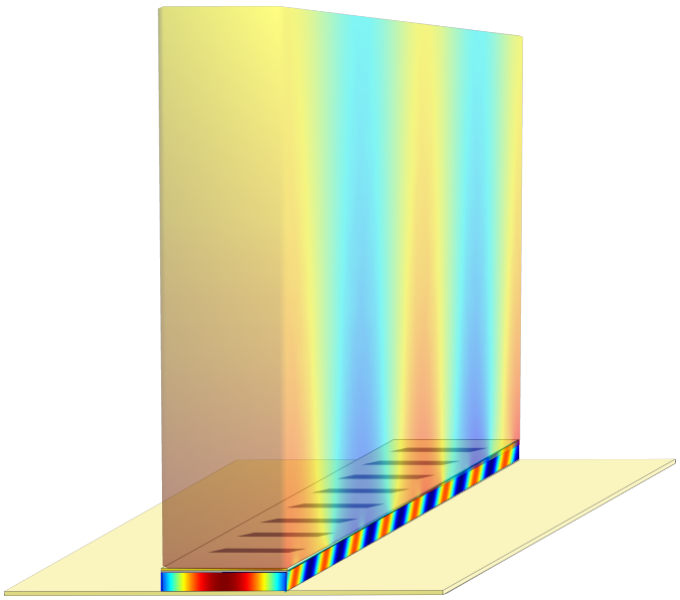

Figure 6.1: Schematic shows the unique characteristics of antenna-feedback that there is a coherent SPP mode on top of laser cavity in addition to that inside the cavity.

the fraction of the overall electromagnetic energy propagating outside the cavity in other conventional solid-state lasers. Consequently, the resonant-frequency of the antenna-feedback mode depends sensitively on the refractive-index of the surrounding medium that could be altered to tune the frequency of the plasmonic laser, which is the technique employed for terahertz QCLs presented in this thesis. To the best of our knowledge, this is a uniquely new mechanism to tune the frequency of a solid-state laser for which there is no analogous precedent in literature. In conclusion, this thesis has demonstrated a continuous ~ 57 GHz tuning from the antenna-feedback scheme for semiconductor lasers with sub-wavelength metallic cavities that emits at ~ 2.8 THz above liquid-nitrogen temperature. The enhanced tuning is achieved by post processing Silicon-dioxide deposition on a mounted and wire-bonded QCLs

with antenna feedback scheme, which operates in single-mode and narrow beam output at 78 K. Due to the large overlap of hybrid surface-plasmon mode of the resonant cavity mode on top of the metallic cavity with the surrounding medium, the frequency of desired lasing mode can be tuned largely when varying the effective refractive-index of the surrounding medium. Compared to previously published results that operated at lower temperature ($\sim$ 10K)), remarkably broader continuous tuning has been achieved at $\sim$ 78K, which provides a larger scope of applicability to THz QCLs and a broader class of plasmonic lasers.

To pursue the goal of THz QCLs with high output power and high radiative efficiency, the new photonic designs are presented in this thesis for surface-emitting second-order DFB. Significantly increased radiative field results in enhanced output power from laser cavity. In addition, more desired single-lobed far field beam pattern is achieved without any central phase shift in metallic gratings.

6.2 Future outlook

Single-mode lasing is realized by introducing distributed-feedback (DFB) in the cavity with periodic photonic structures implemented lithographically. Different types of DFB THz QCLs have been developed such as the ones with a first-order, second-order, third-order gratings respectively, or even two-dimensional photonic-crystal-type architectures and geometries with circular symmetry. However, none of the DFB THz QCLs developed thus-far have an evanescent-field with a large spatial extent on top of the cavity. By utilizing the antenna-feedback scheme described in this thesis that is specifically applicable to THz QCLs, in which, the evanescent-field on top of the metal cladding retains the long extinction length as in a ridge cavity. Importantly then, the propagation constant of the evanescent-mode outside directly impacts the resonant-frequency of the DFB QCL, which is therefore indicative of the complex relative permittivity of the analyte with which the evanescent-field could be made to interact with. Sensing and reference DFB QCLs can be placed in a pair, taking standard fabrication/lithographic variations into account, it is expected

that the lasing frequency of the two QCLs in each pair will be within few GHz of each other. Evanescent-field of the sensing QCLs interacts with the analyte placed outside the cryocooler. Consequently, the effective index of the surrounding medium for the sensing QCLs is altered since a fraction of the evanescent-field propagates in the analyte. As a result, the resonant-wavelength (or resonant-frequency) of the DFB QCL shifts. The change in emission frequency of sensing QCLs in presence of analyte is large even for small variations in either the real or imaginary part of relative permittivity of the analyte, and is in the range of 1 MHz - 1 GHz (that can be further extended depending the required sensitivity). Two key aspects of QCLs with antenna-feedback scheme are being utilized in this sensing, which are different from any other type of semiconductor DFB laser. First, the evanescent-field exists largely on top of the cavity that allows intracavity evanescent-wave sensing even with analyte placed sufficiently away from the cavity. Second, and equally importantly, the effective index of the surrounding medium in which the evanescent-wave propagates modifies the resonant-frequency of DFB QCL directly, unlike for a typical semiconductor laser in which the index of the surrounding medium affects the resonant-frequency by a higher order (weaker) effect due to the mode-confinement considerations. Therefore, terahertz QCLs with antenna-feedback can be effectively integrated into low-cost and portable semiconductor laser based evanescent-wave terahertz sensors.

Terahertz QCLs with high output power and narrow beam patterns in continuous-wave(cw) operation are highly desired for many applications. Laser cavity with wide width could increase the output power, however, heat removal problem prevents wide devices lasing in continuous-wave operation or greatly limits the cw performance. Phased arrays of elements are widely used in the radio-frequency domain, a lot of ideas and technologies in other frequency ranges could be applied and developed in terahertz frequency range as well. However, phasing-locked laser devices operating at visible or infrared wavelengths are more challenging due to the phases in individual elements could not be controlled electronically. Super-modes arrays are constructed by weakly coupling mechanism (for example, by leakage-coupling [88])

or directly through the use of couplers. Phase-locked laser arrays are highly attractive in enhancing output power while achieving good beam quality. Recently, a new mechanism based on antenna mutual coupling to achieve global phase locking in a 2D laser array was proposed, verified by numerical simulation and then experimentally demonstrated using subwavelength short-cavity surface-emitting lasers at terahertz frequencies [89]. Mode that can extends laterally in a large spatial extent based on antenna-feedback scheme developed in this thesis will be explored as a new phase-locking mechanism for effective phase-locked laser arrays.

Appendix A

Appendix

A.1 Fabrication Recipes

Fabrication for terahertz lasers with distributed-feedback is discussed in details in this section of appendix. SEM images of different steps and fabrication recipes are demonstrated. Steps of wafer thermocompression bonding, lapping down substrate, removal of substrate by selective etching and removal of etch stop layer share the same fabrication recipes as terahertz lasers with double metal Fabry-Pérot type cavities. For distributed-feedback scheme, in order to excite the fundamental mode, lossy sections or structures of metal covering sidewall are utilized. To polish all fabrication steps and obtain the optimized parameters of operation in this thesis, dami bonded GaAs wafers were processed before applying corresponding optimized parameters to bonded MBE wafers. To implement lossy absorbing boundary, a thin highly doped contact with thickness 100nm is selectively etched by using positive photoresist lithography, serving as both lateral and longitudinal absorber. The lithography parameters shown in this section are based on the UV lamp of photo lithography used in Sinclair Lab Cleanroom from June, 2012 to March, 2013.

Recipe for layer 1, which is for selectively etching highly doped contact layer. Shipley 1813 is used as the positive photo resist.

- spin coating speed and time: 0.5/0.75/4 krpm, 6/8/32 s,
- prebake: 105 degree C, 60s,
- exposure: 15s (soft contact, air gap 40),
- develop: 40s,
- postbake: 115 degree C, 75 s.

SEM images for top metal gratings of distributed-feedback, mesa etching, oxide and metal covering sidewall, fabricated and wire bonded terahertz lasers with lateral loss sections, metal covering sidewall are shown respectively as below.

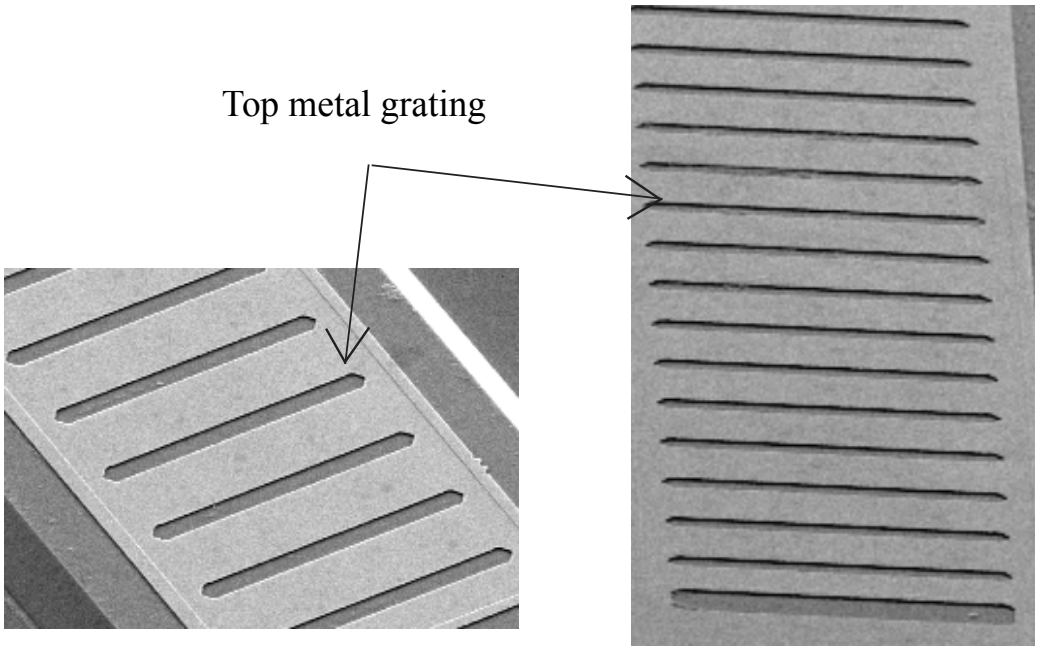

Figure A.1: SEM images for top metal gratings of distributed-feedback.

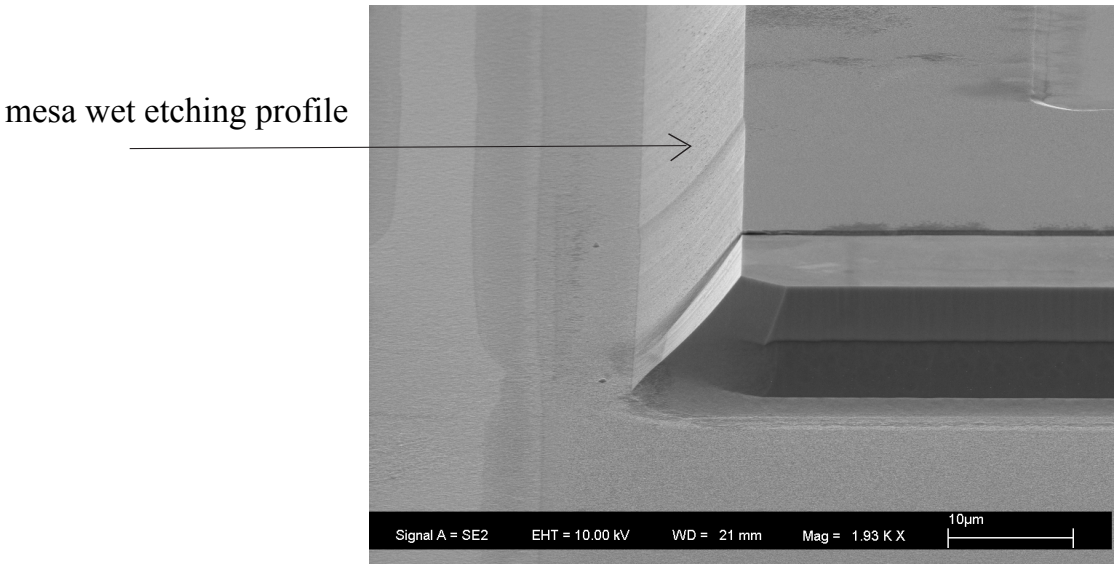

Figure A.2: SEM images for mesa etching profile.

Recipe for image-reversal lithography, AZ5214 photo resist.

- prebake: 110 degree C, 70s,
- first exposure: 9s,
- reversal bake: 120 degree C, 54s,
- flood exposure: 200s,
- develop: 70s.

S1813 positive photo lithography is used for mesa etching mask layer. Etching time of mesa in a H_2SO_4:H_2O_2:H_2O 1:8:80 solution is $\sim$ 22 minutes.

Besides the devices with lateral loss sections, covering the sidewall of laser cavity serves as the other effective method to selectively make the higher order lateral modes more lossy. The following steps are implemented as extra steps in fabrication:

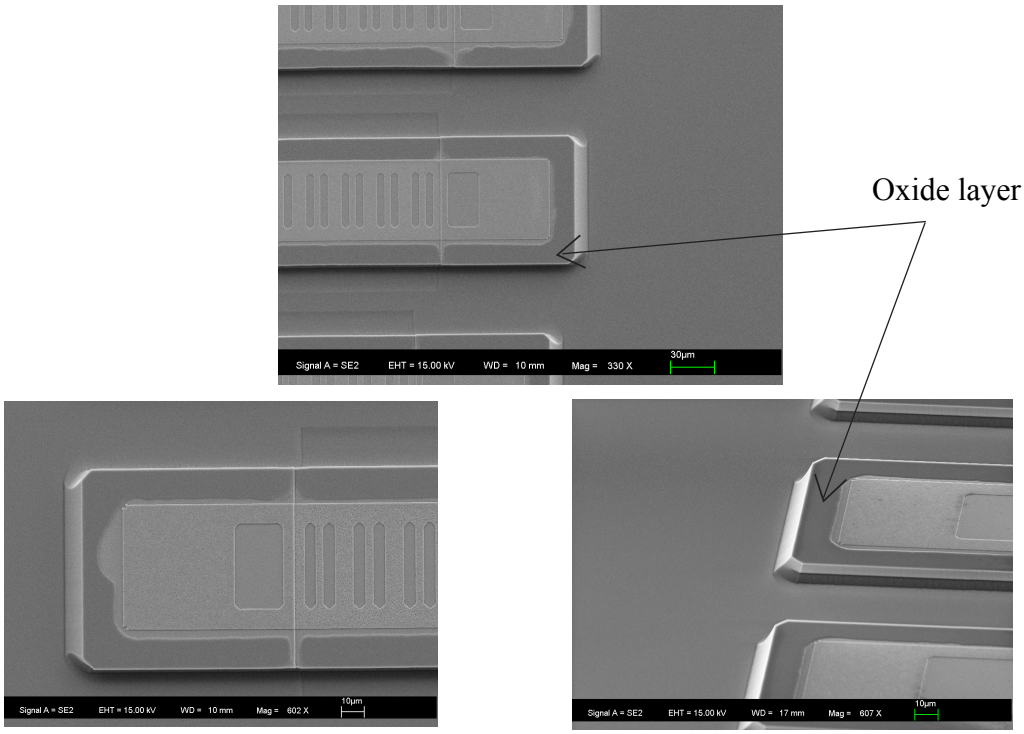

Figure A.3: SEM images for oxide layer.

To cover the sidewall of mesa with silicon dioxide(role of isolation since there will be a step of covering sidewall with metal being followed), thick positive photoresist lithography is required. Lithography parameters are shown as below:

- spin coating speed: 0.5/0.75/0.95 krpm,
- prebake: 112 degree C, 90s,
- exposure: 80s,
- develop: 40s,
- postbake: 130 degree C, 3 min.

In order to cover the sidewall and bottom side (for wire bonding) of cavity with metal, a side/bpad mask and thick AZ5214 lithography step is required.

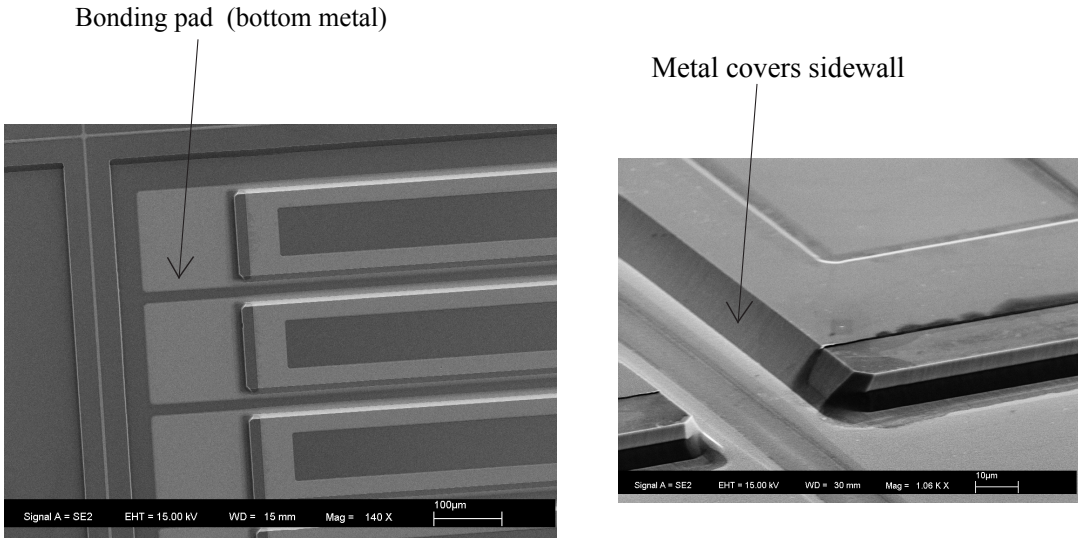

Figure A.4: SEM images for sidewall and bottom of cavities covered with metal.

- spin coating speed and time: 0.5/0.75/1.5 krpm, 6/8/30 s,
- prebake: 110 degree C, 70s,
- first exposure: 9s,
- reversal bake: 121 degree C, 54s,
- flood exposure: 400s,
- develop: 90s.

250/2500 A of Ti/Au was deposited in the E-beam deposition system in Sherman Fairchild Center with the low deposition rate. Deposition rate: for Ti 1A/sec, for Au, first 1250 A with 1 A/s, for the following thickness of 1250 A, deposition rate is 1.3 A/s.

For lift-off of side/bpad metal, typical soaking time: soak 8 min and squirt gun is used. After substrate lapping, thickness of bonded wafer is around $\sim$ 230 μm. Ti/Au is used for substrate metal deposition step, deposition thickness is 300/2000

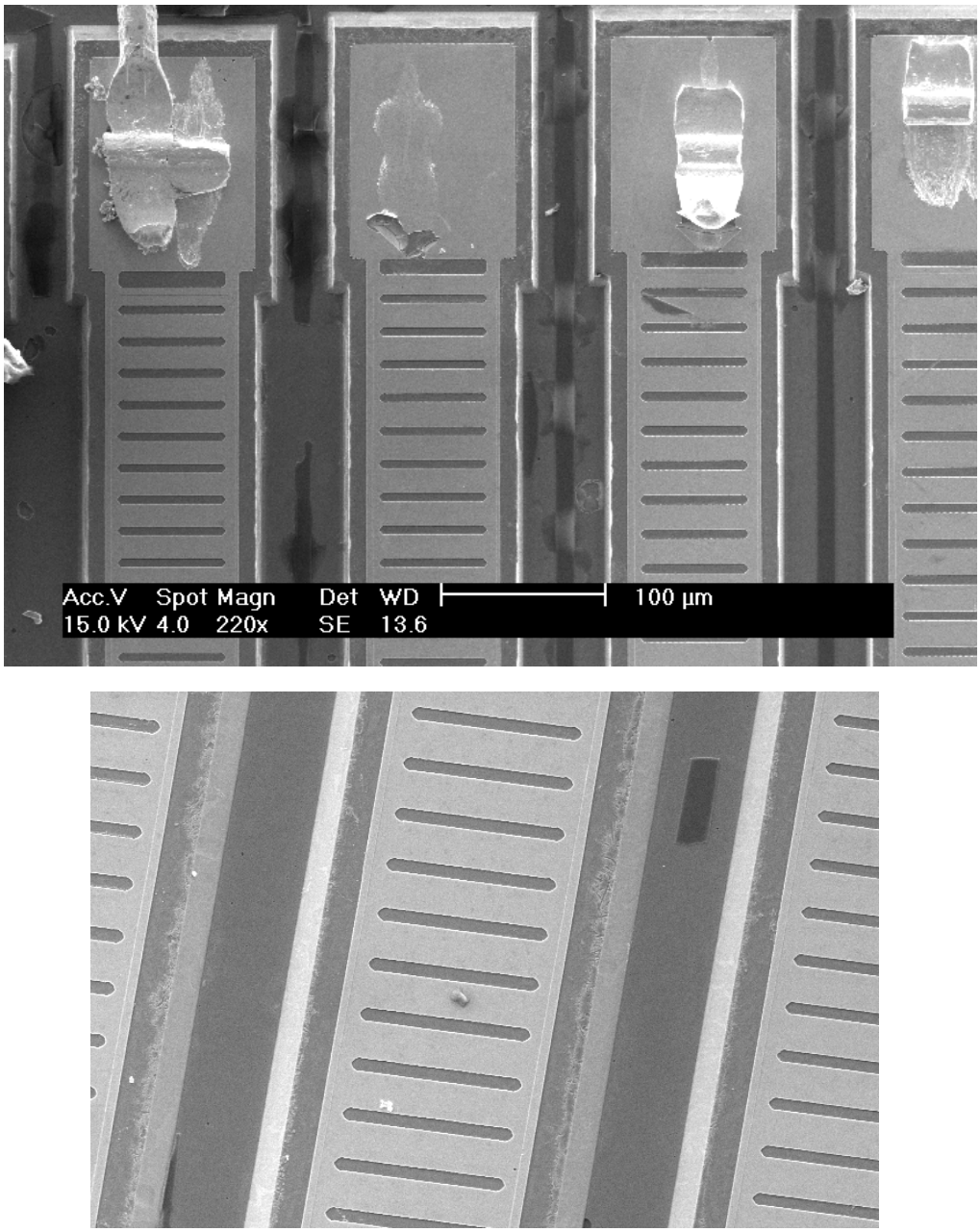

Figure A.5: SEM images of fabricated and wire bonded terahertz lasers with lateral loss sections.

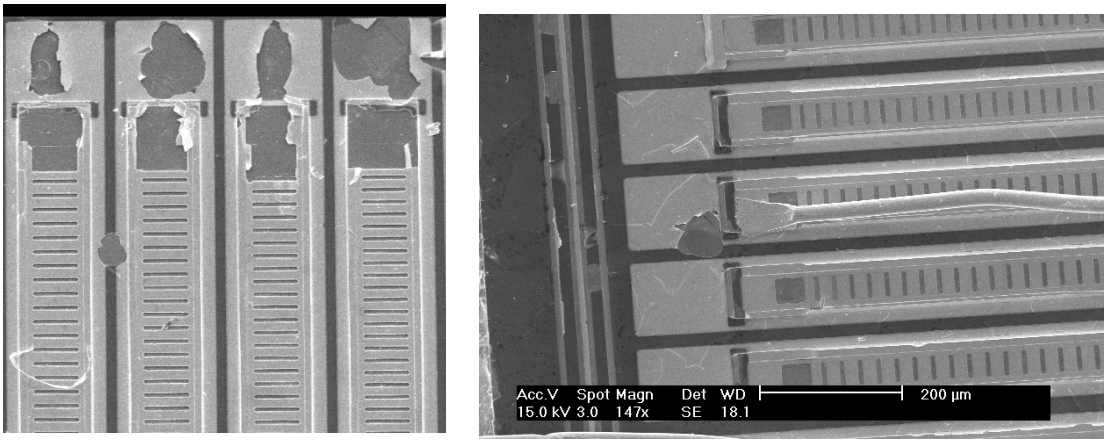

Figure A.6: SEM images of fabricated and wire bonded terahertz lasers with metal covering sidewall.

A. During the deposition process, wafer holding plate inside the E-beam deposition system is not rotating, deposition rate of Ti is 1A/sec, Ti was newly purchased by our group is used for this fabrication run. Thickness of gold deposition is 1000 A, deposition rate is 1 A/sec. For the last 1000 A thickness, deposition rate is 1.3 A/sec.

Mask design with each layer on top of each other for distributed-feedback with lateral loss sections and metal covering sidewall are shown. Cavity with ~ 200 μm width is used to describe the designed parameters for distributed-feedback with lateral loss sections. The distance between edge of mesa etching mask and outer edge of doped contact layer is ~ 15 μm, the distance between edge of metal grating mask and outer edge of doped contact layer is ~ 7 μm. For distributed-feedback with metal covering sidewall, the distance between edge of side metal mask and outer edge of mesa etch mask is ~ 10 μm, the distance between edge of side oxide layer mask and outer edge of mesa etch mask is ~ 25 μm.

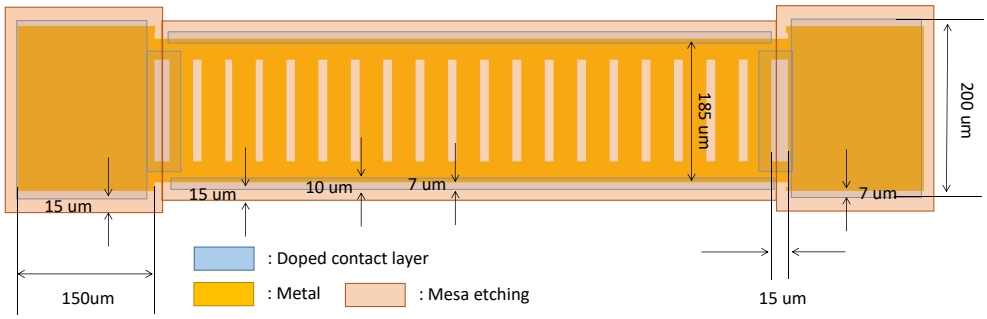

Figure A.7: Schematic of mask design with each layer on top of each other for distributed-feedback with lateral loss sections.

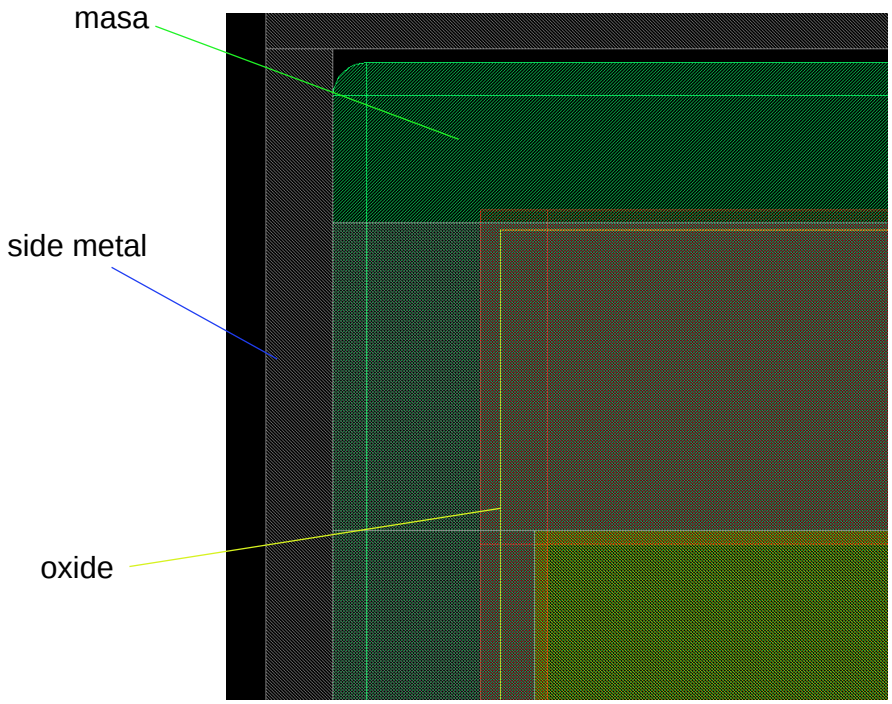

Figure A.8: Mask design with each layer on top of each other for distributed-feedback with metal covering sidewall.

A.2 Finite Element Simulations

A.2.1 2D simulations

The geometry of a typical 2D simulation in this thesis is shown. Radius for big air domain is $\sim$ 1200 μm, while the radius for small air domain is $\sim$ 700 μm. Total length of cavity is $\sim$ 1.4 mm.

The sequence of simulations are listed below.

1. choose solver (eigenfrequency solver) and physics (wave optics), specifically, setting sequence follows Model Wizard, 2D, select physics, optics, wave optics, electromagnetic waves, frequency domain, present studies, eigenfrequency
2. make geometry
3. set materials characteristics
4. electromagnetic properties is set under electromagnetic waves, frequency domain (ewfd), perfect electric conductor (PEC) surface is set for metal layer, which is considered as lossless in THz region
5. mesh
6. calculate eigenfrequency (number of eigenmodes and calculated center frequency are the parameters that can be set)
7. field plot (Ey, Ex, normE are the electric fields distribution plotted in this thesis)

Relative permittivity of each region:

- Active region: 12.9.
- Air: 1.
- Lossy air in the center: $1 - iAL \times (y - SR)$.

- Lossy air in left and right: $1 - iAL \times \sqrt{(|x| - totLen/2)^2 + y^2} - SR$, where x and y are longitudinal and vertical coordinates respectively of any point in the lossy air region.
- Doped contact layer: $-508.7 - i276.7$.
- The loss of each eigenmode is calculated by as α =(imaginary part of eigenfrequency)$\times 2\pi \times 2 \times n_{\mathrm{GaAs}}/(3 \times 10^8)$.

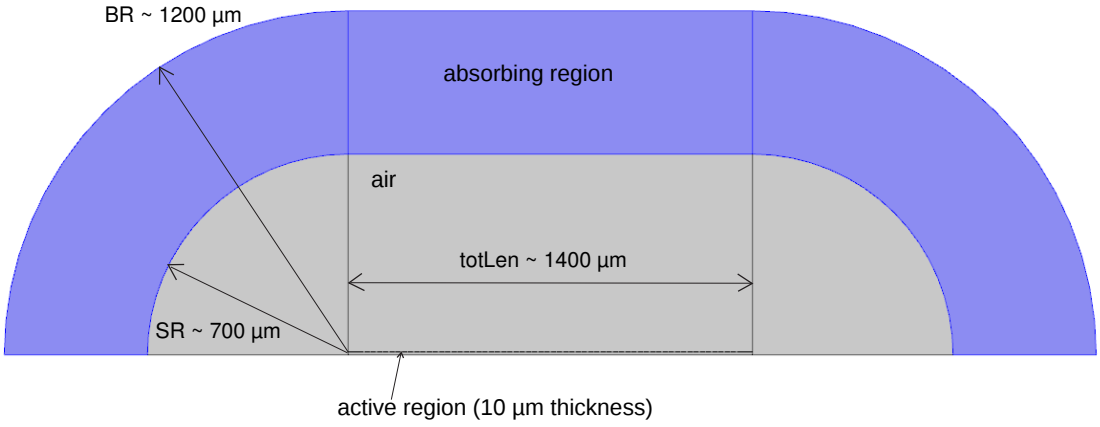

Figure A.9: Geometry for 2D simulations.

Size of mesh is a very important parameter in finite-element simulations. On one hand, mesh size should be accurate enough for the chosen finite element in consideration of geometry size. On the other hand, reasonable mesh size has to be considered with the limit of the computing memory and simulation time. The mesh size of element in 2D simulation in this thesis is generally set as following:

- In doped contact layer domain: DT/2 (DT is thickness of doped contact layer).
- In metal layer domain: MT/2, MT is the thickness of metal layer.
- In waveguide domain: WT/14, WT is the thickness of waveguide layer.

- In air domain, wavelength in air /8.

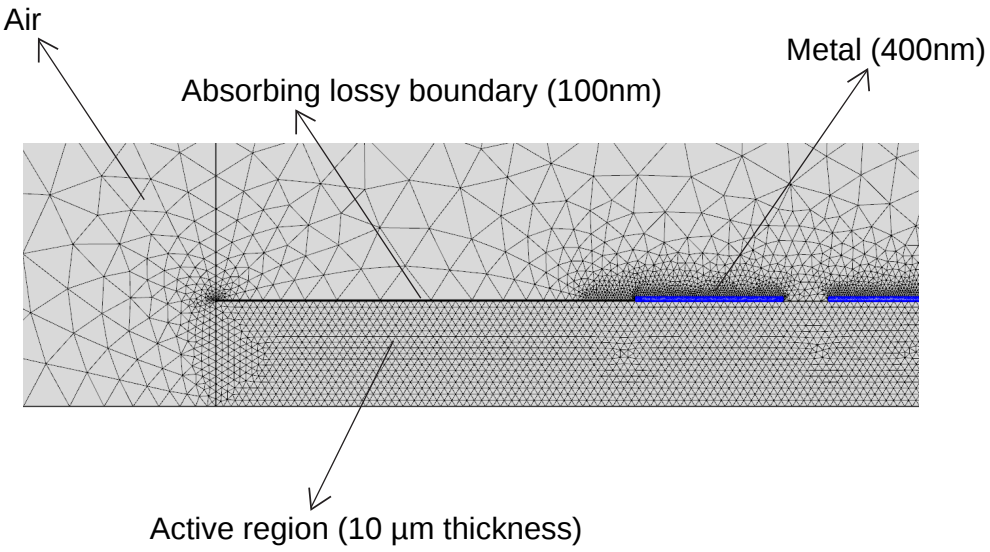

Figure A.10: Finite element mesh for 2D simulations.

A.2.2 3D simulations

3D simulations follow the similar steps as shown above for 2D simulations, some unique characteristics in 3D simulations are discussed in this section.

PML is set as an effective absorbing boundary in 3D simulations. For the 3D simulations in this thesis, PML is set under electromagnetic waves, frequency domain (ewfd). In PML setting, scaling factor is set as 0.0001, PML order is set as 1. In new Comsol version, PML setting is under definition: Definition, PML.

Far field domain is used to calculate the simulated far field beam pattern. Far field domain is set under electromagnetic waves, frequency domain (ewfd). Size of far field domain needs to be far enough from the laser cavity in order not to disturb the near field calculation of laser cavity, especially for antenna-feedback scheme in this thesis that there is a large spatial extent for the desired resonant mode. Far field domain is needed to be defined before running the simulations. In plot, with the definition of far-field domain, Efar will be the E field in the setting of choice

that can be plotted out. Plot the far field beam follows the sequence: in 2D plot group, select intensity of Efar as the value to plot, choose the desired mode whose far filed beam will be calculated under the mode list, set resolution for angles at two directions, typical setting is 100 and unit sphere.

The doped contact(DC) layer in 3D simulations is implemented by self-defined thick DC layer. Because extreme fine mesh is needed to mesh highly doped contact layer with 100nm thickness, which will dramatically increase the total required computing memory in 3D simulation to mesh such thin layer. Therefore, a thick DC layer is implemented rather than a thin DC layer in 3D simulations, taken into consideration of an affordable mesh size. There are two considerations in the setting for the relative permittivity: Firstly, the real part should be as closed as to 12.9. Secondly, the imaginary part contribute to high loss, serving as the lossy absorbing boundary. The corresponding propagation loss at the desired frequency for the chosen Drude model is ~ 500 cm^{-1}. To get an idea of the introduced loss, loss is evaluated by 2Im(k) w/c, Im (k) is the imaginary part of eigen-wavevector, w equals to 2pi*f,f is the frequency of desired mode and c is the speed of light in vacuum.

Relative permittivity of each domain:

- Active region: 12.9.
- Air: 1.
- Thick doped contact layer: $12.35 - i2.74$.

A.3 Mechanical Drawings

Several customer-designed copper mount are used in this thesis for different purposes of measurement. The following figures will show these mounts in details, the designed dimensions and parameters of each mount is marked in each of these figures.

A.3.1 Copper mounts used for edge-emitting and surface-emitting QCLs

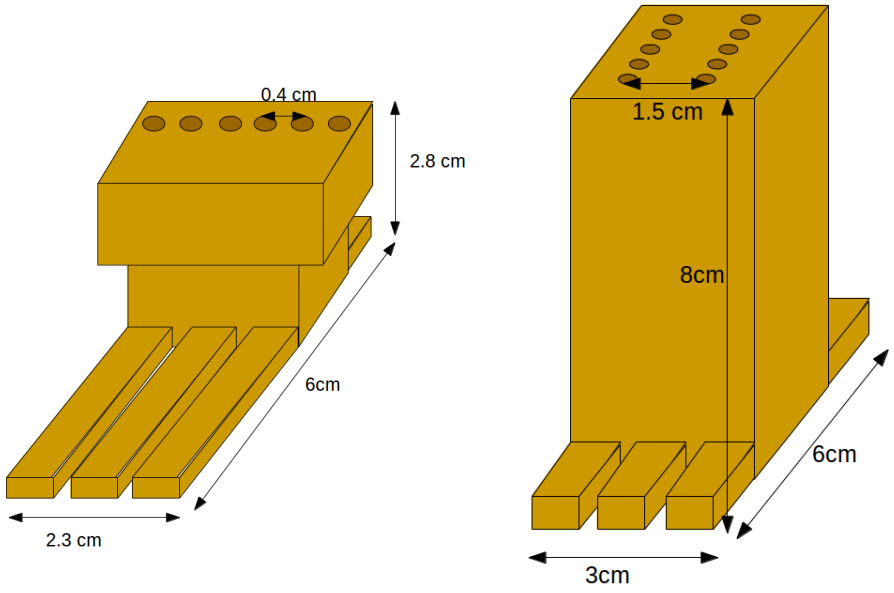

Figure A.11: 3D view of copper mount used for edge emitting devices and surface emitting devices. .

A.3.2 Copper mount for edge-emitting QCLs, to mount very close to dewar's window

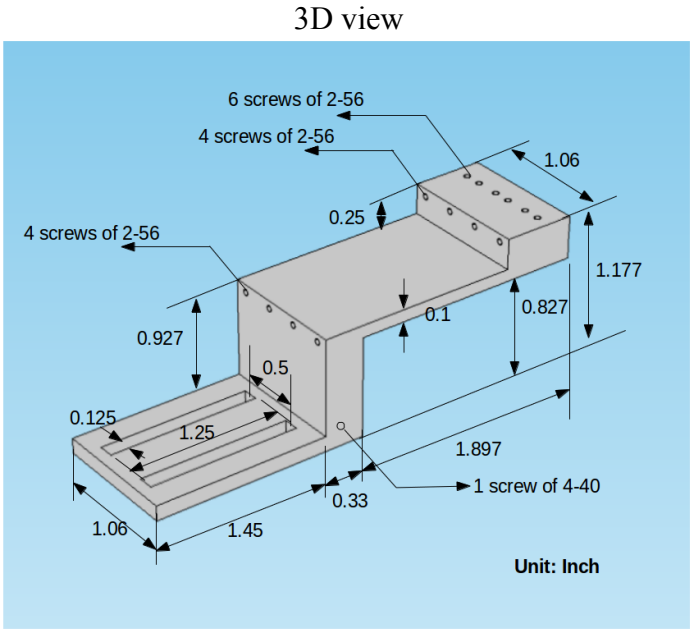

Figure A.12: 3D view of copper mount used for edge emitting devices without cone that can bring the device very close to the dewar's window.

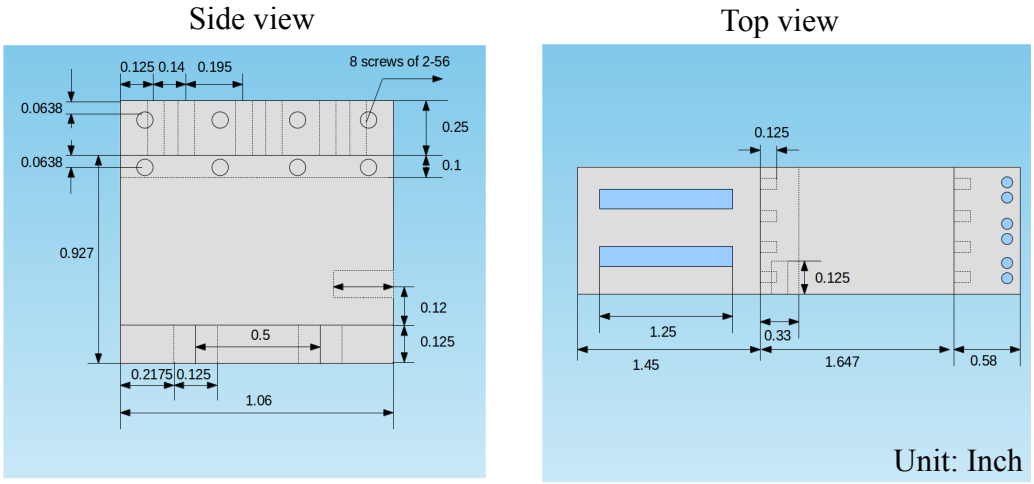

Figure A.13: Side and top view of copper mount used for edge emitting devices without cone that can bring the device very close to the dewar's window. .

Bibliography

[1] Adam, A. J. L. *et al.* Beam patterns of terahertz quantum cascade lasers with subwavelength cavity dimensions. *Appl. Phys. Lett.* **88**, 151105 (2006).

[2] COMSOL 4.4, A finite-element partial differential equation solver from COMSOL Inc.

[3] Tonouchi, M. Cutting-edge terahertz technology. *Nat. Photon.* **1**, 97–105 (2007).

[4] Hu, B. B. & Nuss, M. C. Imaging with terahertz waves. *Opt. Lett.* **20**, 1717 (1995).

[5] Chan, W. L., Diebel, J. & Mittleman, D. M. Imaging with terahertz radiation. *Rep. Prog. Phys.* **70**, 1325–1379 (2007).

[6] Lee, A., Williams, B. S., Kumar, S., Hu, Q. & Reno, J. L. Real-time imaging using a 4.3-THz quantum cascade laser and a 320 x 240 microbolometer focal-plane array. *IEEE Photon. Technol. Lett.* **18**, 1415 (2006).

[7] Darmo, J. *et al.* Imaging with a terahertz quantum cascade laser. *Opt. Express* **12**, 1879 (2004).

[8] Wu, Q., Hewitt, T. & Zhang, X.-C. Two-dimensional electro-optic imaging of thz beams. *Appl. Phys. Lett.* **69**, 1026–1028 (1996).

[9] Siegel, P. H. Terahertz technology. *IEEE Trans. Microwave Theory Tech.* **50**, 910–928 (2002).

[10] Siegel, P. H. Terahertz technology in biology and medicine. *IEEE Trans. Microwave Theory Tech.* **52**, 2438 (2004).

[11] Siegel, P. H. THz instruments for space. *IEEE Trans. Antennas Propag.* **55**, 2957 (2007).

[12] Doi, Y. *et al.* Large-format and compact stressed ge: Ga array for the astro-f (iris) mission. *Advances in Space Research* **30**, 2099–2104 (2002).

[13] West, L. C. & Eglash, S. J. First observation of an extremely large-dipole infrared transition within the conduction band of a GaAs quantum well. *Appl. Phys. Lett.* **46**, 1156–1158 (1985).

[14] Faist, J. *et al.* Quantum cascade laser. *Science* **264**, 553–556 (1994).

[15] Yao, Y., Hoffman, A. J. & Gmachl, C. F. Mid-infrared quantum cascade lasers. *Nat. Photon.* **6**, 432 (2012).

[16] Haller, E. E. Advanced far-infrared detectors. *Infrared Phys.* **35**, 127 (1994).

[17] Köhler, R. *et al.* Terahertz semiconductor-heterostructure laser. *Nature* **417**, 156–159 (2002).

[18] Kumar, S. *Development of terahertz quantum-cascade lasers.* PhD dissertation, Massachusetts Institute of Technology, Department of Electrical Engineering and Computer Science (2007).

[19] Kumar, S. Recent progress in terahertz quantum cascade lasers. *IEEE J. Sel. Topics Quantum Electron.* **17**, 38 (2011).

[20] Kohen, S., Williams, B. S. & Hu, Q. Electromagnetic modeling of terahertz quantum cascade laser waveguides and resonators. *J. Appl. Phys.* **97**, 053106 (2005).

[21] Williams, B. S. *Terahertz quantum cascade lasers.* PhD dissertation, Massachusetts Institute of Technology, Department of Electrical Engineering and Computer Science (2003).

[22] Williams, B. S., Kumar, S., Callebaut, H., Hu, Q. & Reno, J. L. Terahertz quantum-cascade laser at $\lambda \approx 100$ μm using metal waveguide for mode confinement. *Appl. Phys. Lett.* **83**, 2124 (2003).

[23] Orlova, E. E. *et al.* Antenna model for wire lasers. *Phys. Rev. Lett.* **96**, 173904 (2006).

[24] Yariv, A. & Yeh, P. *Photonics* (Oxford University Press, 2006), 6 edn.

[25] Kumar, S. *et al.* Surface-emitting distributed feedback terahertz quantum-cascade lasers in metal-metal waveguides. *Opt. Express* **15**, 113 (2007).

[26] Amanti, M. I., Scalari, G., Castellano, F., Beck, M. & Faist, J. Low divergence terahertz photonic-wire laser. *Opt. Express* **18**, 6390 (2010).

[27] Bergman, D. J. & Stockman, M. I. Surface plasmon amplification by stimulated emission of radiation: Quantum generation of coherent surface plasmons in nanosystems. *Phys. Rev. Lett.* **90**, 027402 (2003).

[28] Hill, M. T. & Gather, M. C. Advances in small lasers. *Nat. Photon.* **8**, 908 (2014).

[29] Oulton, R. F. Surface plasmon lasers: sources of nanoscopic light. *Mater. Today* **15**, 26 (2012).

[30] Berini, P. & Leon, I. D. Surface plasmon-polariton amplifiers and lasers. *Nat. Photon.* **6**, 16 (2012).

[31] Noginov, M. A. *et al.* Demonstration of a spaser-based nanolaser. *Nature* **460**, 1110 (2009).

[32] Williams, B. S. Terahertz quantum-cascade lasers. *Nat. Photon.* **1**, 517–525 (2007).

[33] Hill, M. T. *et al.* Lasing in metal-insulator-metal sub-wavelength plasmonic waveguides. *Opt. Express* **17**, 11107 (2009).

[34] Oulton, R. F. *et al.* Plasmon lasers at deep subwavelength scale. *Nature* **461**, 629 (2009).

[35] Lu, Y.-J. *et al.* Plasmonic nanolaser using epitaxially grown silver film. *Science* **337**, 450 (2012).

[36] Zhou, W. *et al.* Lasing action in strongly coupled plasmonic nanocavity arrays. *Nat. Nanotech.* **8**, 506 (2013).

[37] van Beijnum, F. *et al.* Surface plasmon lasing observed in metal hole arrays. *Phys. Rev. Lett.* **110**, 206802 (2013).

[38] Meng, X., Liu, J., Kildishev, A. V. & Shalaev, V. M. Highly directional spaser array for the red wavelength region. *Laser & Photonics Reviews* **8**, 896–903 (2014).

[39] Yang, A. *et al.* Real-time tunable lasing from plasmonic nanocavity arrays. *Nature Comm.* **6**, 6939 (2015).

[40] Schokker, A. H. & Koenderink, A. F. Lasing at the band edges of plasmonic lattices. *Phys. Rev. B* **90**, 155452 (2014).

[41] Dorofeenko, A. V. *et al.* Steady state superradiance of a 2D-spaser array. *Opt. Express* **21**, 14539–14547 (2013).

[42] Mahler, L. & Tredicucci, A. Photonic engineering of surface-emitting terahertz quantum cascade lasers. *Laser & Photon. Rev.* **5**, 647–658 (2011).

[43] Sirtori, C., Barbieri, S. & Collombelli, R. Wave engineering with THz quantum cascade lasers. *Nat. Photon.* **7**, 691 (2013).

[44] Kao, T.-Y., Hu, Q. & Reno, J. L. Phase-locked arrays of surface-emitting terahertz quantum-cascade lasers. *Appl. Phys. Lett.* **96**, 101106 (2010).

[45] Halioua, Y. *et al.* Phase-locked arrays of surface-emitting graded-photonic-heterostructure terahertz semiconductor lasers. *Opt. Express* **23**, 6915 (2015).

[46] Xu, L. *et al.* Metasurface external cavity laser. *Appl. Phys. Lett.* **107**, 221105 (2015).

[47] Amanti, M. I., Fischer, M., Scalari, G., Beck, M. & Faist, J. Low-divergence single-mode terahertz quantum cascade laser. *Nat. Photon.* **3**, 586–590 (2009).

[48] Kao, T. Y., Hu, Q. & Reno, J. L. Perfectly phase-matched third-order DFB THz quantum-cascade lasers. *Opt. Lett.* **37**, 2070 (2012).

[49] Williams, B. S., Kumar, S., Hu, Q. & Reno, J. L. Distributed-feedback terahertz quantum-cascade lasers with laterally corrugated metal waveguides. *Opt. Lett.* **30**, 2909 (2005).

[50] Fan, J. A. *et al.* Surface emitting terahertz quantum cascade laser with a double-metal waveguide. *Opt. Express* **14**, 11672 (2007).

[51] Chassagneux, Y. *et al.* Electrically pumped photonic-crystal terahertz lasers controlled by boundary conditions. *Nature* **457**, 174 (2009).

[52] Halioua, Y. *et al.* THz quantum cascade lasers operating on the radiative modes of a 2D photonic crystal. *Opt. Lett.* **39**, 3962 (2014).

[53] Lalanne, P., Hugonin, J., Liu, H. & Wang, B. A microscopic view of the electromagnetic properties of sub-λ metallic surfaces. *Surf. Sci. Rep.* **64**, 453 (2009).

[54] Babuty, A. *et al.* Semiconductor surface plasmon sources. *Phys. Rev. Lett.* **104**, 226806 (2010).

[55] Demichel, O. *et al.* Surface plasmon photonic structures in terahertz quantum cascade lasers. *Opt. Express* **14**, 5335 (2006).

[56] Xu, G. *et al.* Efficient power extraction in surface-emitting semiconductor lasers using graded photonic heterostructures. *Nature Comm.* **3**, 952 (2012).

[57] Khanal, S., Zhao, L., Reno, J. L. & Kumar, S. Temperature performance of terahertz quantum-cascade lasers with resonant phonon active-regions. *J. Opt* **16**, 094001 (2014).

[58] Liang, G. *et al.* Planar integrated metasurfaces for highly-collimated terahertz quantum cascade lasers. *Sci. Rep.* **4**, 7083 (2014).

[59] Yu, N. *et al.* Designer spoof surface plasmon structures collimate terahertz laser beams. *Nat. Materials* **9**, 730 (2010).

[60] Boyle, C. *et al.* High-power, surface-emitting quantum cascade laser operating in a symmetric grating mode. *Appl. Phys. Lett.* **108**, 121107 (2016).

[61] Balanis, C. A. *Antenna Theory: Analysis and Design* (Wiley-Interscience, 2005), 3 edn.

[62] Wu, C., Khanal, S., Reno, J. L. & Kumar, S. Terahertz plasmonic laser radiating in an ultra-narrow beam. *Optica* **3**, 734–740 (2016).

[63] Khanal, S., Reno, J. L. & Kumar, S. 2.1 thz quantum-cascade laser operating up to 144 k based on a scattering-assisted injection design. *Opt. Express* **23**, 19689–19697 (2015).

[64] Mahler, L. *et al.* High-power surface emission from terahertz distributed feedback lasers with a dual-slit unit cell. *Appl. Phys. Lett.* **96**, 191109 (2010).

[65] Lu, Y.-J. *et al.* All-color plasmonic nanolasers with ultralow thresholds: Autotuning mechanism for single-mode lasing. *Nano Lett.* **14**, 4381–4388 (2014).

[66] Yang, A. *et al.* Real-time tunable lasing from plasmonic nanocavity arrays. *Nature Comm.* **6**, 6939 (2015).

[67] Vitiello, M. S., Scalari, G., Williams, B. & Natale, P. D. Quantum cascade lasers: 20 years of challenges. *Opt. Express* **23**, 5167 (2015).

[68] Chattopadhyay, G. Technology, capabilities, and performance of low power terahertz sources. *IEEE Trans. THz Sci. Technol.* **1**, 33 (2011).

[69] Li, L. *et al.* Terahertz quantum cascade lasers with > 1 W output powers. *Electron. Lett.* **50**, 309 (2014).

[70] Scalari, G. *et al.* THz and sub-THz quantum cascade lasers. *Laser & Photon. Rev.* **3**, 45–66 (2009).

[71] Fathololoumi, S. *et al.* Terahertz quantum cascade lasers operating up to $\sim$ 200 K with optimized oscillator strength and improved injection tunneling. *Opt. Express* **20**, 3866 (2012).

[72] Vitiello, M. S. & Tredicucci, A. Tunable emission in THz quantum cascade lasers. *IEEE Trans. THz Sci. Technol.* **1**, 76 (2011).

[73] Ren, Y. *et al.* High-resolution heterodyne spectroscopy using a tunable quantum cascade laser around 3.5 THz. *Appl. Phys. Lett.* **98**, 231109 (2011).

[74] Hübers, H.-W., Eichholz, R., Pavlov, S. G. & Richter, H. High resolution terahertz spectroscopy with quantum cascade lasers. *J. Infrared Milli. Terahz. Waves* **34**, 325 (2013).

[75] Xu, J. *et al.* Tunable terahertz quantum cascade lasers with an external cavity. *Appl. Phys. Lett.* **91**, 121104 (2007).

[76] Lee, A. W. M., Williams, B. S., Kumar, S., Hu, Q. & Reno, J. L. Tunable terahertz quantum cascade lasers with external gratings. *Opt. Lett.* **35**, 910 (2010).

[77] Qin, Q., Reno, J. L. & Hu, Q. MEMS-based tunable terahertz wire-laser over 330GHz. *Opt. Lett.* **36**, 692 (2011).

[78] Han, N. *et al.* Broadband all-electronically tunable mems terahertz quantum cascade lasers. *Opt. Lett.* **39**, 3480–3483 (2014).

[79] Castellano, F. *et al.* Tuning a microcavity-coupled terahertz laser. *Appl. Phys. Lett.* **107**, 261108 (2015).

[80] Turčinková, D., Amanti, M. I., Castellano, F., Beck, M. & Faist, J. Continuous tuning of terahertz distributed feedback quantum cascade laser by gas condensation and dielectric deposition. *Appl. Phys. Lett.* **102**, 181113 (2013).

[81] Zhang, H., Dunbar, L. A., Scalari, G., Houdré, R. & Faist, J. Terahertz photonic crystal quantum cascade lasers. *Opt. Express* **15**, 16818 (2007).

[82] Dunbar, L. A. *et al.* Small optical volume terahertz emitting microdisk quantum cascade lasers. *Appl. Phys. Lett.* **90**, 141114 (2007).

[83] Turčinková, D., Amanti, M. I., Scalari, G., Beck, M. & Faist, J. Electrically tunable terahertz quantum cascade lasers based on a two-sections interdigitated distributed feedback cavity. *Appl. Phys. Lett.* **106**, 131107 (2015).

[84] Lee, K.-S., Lu, T.-M. & Zhang, X.-C. Tera tool [terahertz time-domain spectroscopy]. *Circuits and Devices Magazine, IEEE* **18**, 23–28 (2002).

[85] Schubert, M. & Rana, F. Analysis of terahertz surface emitting quantum-cascade lasers. *IEEE J. Quantum Electron.* **42**, 257 (2006).

[86] Xu, G. *et al.* Surface-emitting terahertz quantum cascade lasers with continuous-wave power in the tens of milliwatt range. *Appl. Phys. Lett.* **104**, 091112 (2014).

[87] Xu, G. *et al.* Stable single-mode operation of surface-emitting terahertz lasers with graded photonic heterostructure resonators. *Appl. Phys. Lett.* **102**, 231105 (2013).

[88] Botez, D. & Peterson, G. Modes of phase-locked diode-laser arrays of closely spaced antiguides. *Electron. Lett.* **24**, 1042–1044 (1988).

[89] Kao, T.-Y., Reno, J. L. & Hu, Q. Phase-locked laser arrays through global antenna mutual coupling. *Nat. Photon.* (2016).

Vita

Vita: Chongzhao Wu

Education:

Aug. 2010 - Present **LEHIGH UNIVERSITY**
Ph.D. candidate, Department of Electrical and Computer Engineering
Advisor: Prof. Sushil Kumar
Thesis: Terahertz plasmonic lasers with distributed-feedback

Sep. 2006 - July 2010 **FUDAN UNIVERSITY**
Bachelor of Science in Department of Electrical Engineering and Automation
Advisor: Prof. Xiaoyuan Hou, Department of Physics

Aug. 2008 - Jan. 2009 **NATIONAL TSINGHUA UNIVERSITY**
Exchange student in Department of Electrical Engineering and Institute of Photonics

Selective honors and awards:

- 2015 SPIE student chapter officer travel grant award for Photonics West 2016, SPIE
- 2015 Rossin Doctoral Fellow, P.C. Rossin College of Engineering and Applied Science, Lehigh University
- 2015 Sherman Fairchild Fellowship for Solid State Studies, Lehigh University
- 2014 Lehigh University Innovation Prize, sponsored by Baker Institute for Entrepreneurship, Lehigh University
- 2014 Sherman Fairchild Fellowship for Solid State Studies, Lehigh University
- 2011 Packard Fellowship, Lehigh University

Selective Publications:
Journal Publications:

- Chongzhao Wu, Sudeep Khanal, John L. Reno and Sushil Kumar, " Terahertz plasmonic laser radiating in an ultra-narrow beam ", *Optica 3, 734–740 ,2016*
- Chongzhao Wu, Yuan Jin, John L. Reno and Sushil Kumar, " Large tuning of narrow-beam terahertz plasmonic lasers operating at 78 K ", *submitted, arXiv:1607.06991 [physics.optics], 2016*
- Chongzhao Wu, Yuan Jin and Sushil Kumar, " Design and analysis of terahertz quantum-cascade lasers with antenna-feedback scheme", *to be submitted*

- Le Zhao, Sudeep Khanal, Chongzhao Wu and Sushil Kumar, “ Proposal for a broadband THz refractive-index sensor based on quantum-cascade laser arrays ”, *Optics Express 23(4), 4751-4765, 2015*

Conference Papers:

- Chongzhao Wu, John. L. Reno and Sushil Kumar, “Broad continuous tuning of single-mode terahertz quantum cascade lasers operating at 50 K ”, *SPIE Photonics West, 2016, Vol. 9767, San Francisco, CA*
- Chongzhao Wu, Sudeep Khanal, John. L. Reno and Sushil Kumar, “Single-mode THz quantum cascade lasers with ultra-narrow beam pattern ”, *International Quantum Cascade Lasers School and Workshop (IQCLSW), 2014, Policoro, Italy*
- Chongzhao Wu, Sudeep Khanal, Sushil Kumar, and John. L. Reno, “Antenna-coupled THz quantum cascade lasers for high-power emission,” *IEEE Photonics Conference 2013, WE1.3, Bellevue, WA*

US Patent:
Sushil Kumar, Chongzhao Wu, Antenna feedback scheme for achieving narrow beam emission from plasmonic lasers, US patent (pending) application number *14/984,652, filed on Dec. 30, 2015*

Leadership:
President of SPIE Student Chapter at Lehigh University, 2013 – present